

Distribution Agreement

In presenting this thesis or dissertation as a partial fulfillment of the requirements for an advanced degree from Emory University, I hereby grant to Emory University and its agents the non-exclusive license to archive, make accessible, and display my thesis or dissertation in whole or in part in all forms of media, now or hereafter known, including display on the world wide web. I understand that I may select some access restrictions as part of the online submission of this thesis or dissertation. I retain all ownership rights to the copyright of the thesis or dissertation. I also retain the right to use in future works (such as articles or books) all or part of this thesis or dissertation.

Signature:

Pablo E. Illing

Date

Slow granular flows: roles of polydispersity and cohesion

By

Pablo E. Illing
Doctor of Philosophy

Department of Physics

Eric R. Weeks, Ph.D.
Advisor

Victor Breedveld, Ph.D.
Committee Member

Stefan Boettcher, Ph.D.
Committee Member

Justin Burton, Ph.D.
Committee Member

Jennifer Rieser, Ph.D.
Committee Member

Accepted:

Kimberly J. Arriola, Ph.D.
Dean of the James T. Laney School of Graduate Studies

Date

Slow granular flows: roles of polydispersity and cohesion

By

Pablo E. Illing
B.A. & M.Sc., Universidad de Buenos Aires, Argentina, 2019

Advisor: Eric R. Weeks, Ph.D.

An abstract of
A dissertation submitted to the Faculty of the
James T. Laney School of Graduate Studies of Emory University
in partial fulfillment of the requirements for the degree of
Doctor of Philosophy
in Department of Physics
2024

Abstract

Slow granular flows: roles of polydispersity and cohesion

By Pablo E. Illing

This work consists of two simulation projects and a experimental project, which study the effect cohesive forces and polydispersity have on granular materials and on granular flows.

The first computational project studies the compression and fracture of crystal and glassy materials using 2D droplet arrays, and the effects of cohesive forces and polydispersity. We use a bubble model to simulate droplets, with an attractive force, which makes the bubbles adhere to each other and the walls. Droplets are first placed in an hexagonal array. For monodisperse bubbles, this forms a crystalline aggregate, polydisperse rafts resemble a glassy material. Once initialized, the droplet raft will be compressed between two walls, with only one wall moving towards the other. The array is compressed and eventually induced to rearrange. These rearrangements occur via fractures, in which depletion bonds are broken between droplets. In crystal arrays, fractures are preceded by a peak in the force exerted on the walls, which drops once the fracture occurs. For small droplet arrays, a single fracture propagates through the crystal in a single well-defined event. For larger rafts, multiple fractures can nucleate at different locations and propagate nearly simultaneously, leading to competing fractures. In polydisperse arrays, the addition of multiple droplet sizes further disrupts the fracture events, showing differences between ideal crystalline arrays, crystalline arrays with a small number of defects, and fully amorphous arrays.

The experimental project studied the 2D granular flow of highly polydisperse hard disks in a non-conventional flow geometry. We use a variety of size distributions with the largest particle being five time larger than the smallest. The experimental setup uses plungers to push the particles in a back and forth fashion. We find the flow behaves in a strikingly different manner compared to size distributions with lower polydispersity that are commonly studied. We characterize the non-affine motion and particle rearrangement, and find a qualitatively difference in the behavior of smaller and larger particles. The smaller particles tend to have higher non-affine motion, induced by the larger disks. Furthermore, we found that this local non-affine behavior increases with increasing polydispersity.

For the third project we study the clogging of gravity driven cohesive particle in a two dimensional hopper, using my simulations, and experimental data provided by our collaborators at McMaster University. Using a similar model used in the first computational project, with added gravitational forces, we simulate adhesive droplets as they flow due to gravity through a hopper. We vary the size of the opening, as well as the depletion and gravitational forces. We find that stronger depletion leads to higher clogging probability. By taking into account the depletion and gravitational forces, we can define a cohesive length scale, which effectively collapses all our simulation and experimental data onto a master curve. This indicates that for cohesive granular materials, in addition to particle size, the cohesive length scale must also be taken into account to describe the clogging.

Slow granular flows: roles of polydispersity and cohesion

By

Pablo E. Illing
B.A. & M.Sc., Universidad de Buenos Aires, Argentina, 2019

Advisor: Eric R. Weeks, Ph.D.

A dissertation submitted to the Faculty of the
James T. Laney School of Graduate Studies of Emory University
in partial fulfillment of the requirements for the degree of
Doctor of Philosophy
in Department of Physics
2024

Acknowledgments

First I'd like to thank Eric Weeks for his guidance during my six years at Emory. His extensive knowledge and expertise helped immensely to my professional development. I would also like to thank my committee members, Justin Burton, Stefan Boettcher, Jennifer M Rieser and Victor Breedveld, for their help, feedback and suggestions since they became my committee. I would like to extend more words of appreciation to Justin for his continued support and availability for questions regarding not only physics, but my general professional development as well. To David Meer and Waad Paliwal, I'd like to thank them for always being willing to help, to brainstorm, give feedback, or to take a minute and just decompress for a minute or two. I'd also like to thank Barbara Conner and Jason Boss, for always being there to help with bureaucratic or technical problems, respectively. I'd also like to thank my friends in the graduate student body, who helped me know Atlanta and have fun here. Outside Emory. I would like to extend a huge thank you to my family, my parents, Fernando Illing and Clara Guillermina Rodriguez Ortega, my brother Axel Eduardo Illing, and my aunt, Ana Maria Rodriguez Ortega, who were there during the harsh times and the fun times. I want to also extend my thanks to Mariana Lucila Aquino, for supporting me and accompanying me in this journey, even all the way back home. Lastly my friends from the Atlanta Historical Fencing Academy, who help make this place feel a bit more like home, and my friends back home, who always make me feel welcome.

Finally, I want to thank the financial support for this research, that was provided by the National Science Foundation Grants CBET-1804186, CBET-2002815 and CBET-2306371. I also would like to thank the physics department, Laney Graduate School and Emory University for their support over the years.

Contents

1	Introduction	1
1.1	Colloidal crystals and glasses	6
1.2	Amorphous flow: Shearing of soft glassy materials	9
1.3	Amorphous Flow: Hopper discharge and Clogging	13
1.4	Dissertation Outline	16
2	Compression and fracture of ordered and disordered droplet rafts	18
2.1	Introduction	19
2.2	Computational methods	21
2.2.1	Simulation forces	21
2.2.2	Model parameters	27
2.2.3	Simulation timescales	28
2.2.4	Simulation goals	29
2.3	Analytical results	30
2.3.1	Effective spring constant: two droplets	30
2.3.2	Equivalent spring model for three droplets	33
2.4	Computational results for large droplet arrays	39
2.4.1	Equivalent spring model for nominally monodisperse crystals	39
2.4.2	Bidisperse aggregates	47
2.4.3	Competing fractures	51

2.5	Conclusions	58
3	Amorphous flow of highly polydisperse disks	61
3.1	Introduction	61
3.2	Experimental methods	64
3.2.1	Experimental procedure	68
3.2.2	Particle size distributions	68
3.2.3	Image analysis	71
3.3	Results	72
3.3.1	Mean Flow	72
3.3.2	Non affine displacement and local particle rearrangement . . .	74
3.3.3	Time scale dependence	88
3.3.4	Strain clock	90
3.4	Conclusions	94
4	Clogging of cohesive particles in a two-dimensional hopper	98
4.1	Introduction	98
4.2	Methods	100
4.2.1	Computational methods	100
4.2.2	Experimental methods	102
4.3	Results	105
4.4	Conclusions	114
5	Conclusions	117
	Appendix A Effect of polydispersity on the rotation of hard disks	123
	Bibliography	126

List of Figures

- 1.1 Examples of soft condensed matter systems. Starting from the top left (a) toothpaste, a colloid composed sodium fluoride, antibacterial agents, etc., as the dispersed phase with water as the dispersion medium. (b) Mayonnaise, an emulsion made from oil, egg yolk and vinegar. (c) Shaving cream, a foam made using soaps and oils. (d) A pile of sand, glass marbles, rods, plastic spheres and an ellipsoid as an example of a granular system. 2
- 1.2 Examples of polydisperse distributions of circles. Figs.(a) and (b) show a pair of Gaussian size distributions with polydispersity $\delta = 0.5$, and $\delta = 0.25$, respectively, both with average radius $\langle R \rangle = 1$. Figs. (c) and (d) show two bidisperse distributions with size ratio 1 : 2.6, and with polydispersity $\delta = 0.32$ and $\delta = 0.5$, respectively. 5
- 1.3 Phase diagram of hard spheres as a function on the volume fraction, Φ Solid arrows indicate equilibrium states, whereas dashed arrows are non-equilibrium states. We note that for the glassy state to exist, some polydispersity is required in the system. The bottom inset images are confocal micrographs. Republished with permission of IOP Publishing, Ltd, from “The physics of the colloidal glass transition”, Gary L. Hunter and Eric R. Weeks [11]; permission conveyed through Copyright Clearance Center, Inc.. 6

1.4	Force needed to compress an array of droplets as the distance between the walls decreases. We can see that the maximum force needed to deform the droplets decreases the more glassy the array of droplet becomes. This behaviour will be further discussed in Chapter 2.	8
1.5	Examples of granular flow. Fig. 1.5(a) shows a landslide in Alaska after an earthquake, photo by <i>icefogger</i> , republished under creative commons license, original picture link(circleto.circle.blog/2022/05/11/alaska-time/). Fig.(b) shows a stream of rocks in New Zealand after a particularly heavy storm, picture by Donna Field. Figs.1.5(c) and (d) show examples of granular flow in a Skittles factory (photo courtesy of Mars Wrigley) and a water bottling facility respectively (Image capture from <i>StrongPoint Automation</i> on <i>youtube</i>). Most granular flows find in both nature and industry correspond to this regime of densely packed particles interacting through contact forces,	10
1.6	Sketch of macroscopic response of amorphous materials to external load. Failure and steady flow correspond to brittle and ductile materials respectively. At a certain maximum amount of stress the material yields and begins to deform. If the system begins to flow the stress now fluctuates around at a steady state stress value.	11
1.7	A brittle crystalline formation of droplets yielding under applied stress. Prior to reaching the stress limit the array deforms elastically. Once the stress threshold is reached the stress is released locally resulting in cascade of stress relaxation in the form of a propagating fracture. This phenomenon will be further discussed in Chapter 2.	12

1.8	<p>Examples of clogging in variety of systems. Fig.(a) shows the outflow of non-frictional spheres out of a 2D hopper. Fig.(b) shows sheep flow through a narrow gate, with an obstacle in front of it. Republished with permission of Springer Nature under a Creative Commons license, from Scientific Reports, “Clogging transition of many-particle systems flowing through bottlenecks”, Iker Zuriguel <i>et al.</i> [45]. Finally Fig.(c) shows a traffic clog in Indonesia, original photo by Fikir Yusuf.</p>	14
1.9	<p>Fig.(a): Clogging probability(P) for systems of soft spheres, as a function of hopper opening of particle diameter(w/d) for various ratio of particle softness and gravitational strength. Republished with permission of American Physical Society, from ”Clogging of soft particles in two-dimensional hoppers”, Xia Hong, Meghan Kohne, Mia Morrell, Haoran Wang, and Eric R. Weeks, Phys. Rev. E 96, 062605 (2017)[52]. Fig(b) Clogging probability $J_N(D)$ as a function of hopper opening to particle size ratio D, for hoppers loaded with N particles. Republished with permission of the EPL Editorial Office, from “Jamming and critical outlet size in the discharge of a two-dimensional silo” [47].</p>	15
2.1	<p>Snapshots for a twenty droplet simulation. In this simulation the droplet is arranged in a $p = 4$ by $q = 5$ configuration.</p>	23
2.2	<p>Illustrations of how the depletants act when in high enough concentration. In (a) we see how the resulting pressure of depletants pushed together droplets which surfaces are within one depletant diameter away from each other. In (b) we show the excluded volumes in which depletants don’t fit in. Overlapping volumes occur when two excluded volumes overlap, this results in a net gain of available volume for the depletants, which increases the net entropy of the system, lowering the Helmholtz free energy, resulting in an attractive force between the droplets.</p>	25

2.3 (a-d): Consecutive snapshots of the row reduction for three droplets: note that time increases from right to left, to match panel (e). Blue bonds are under tension, whereas red indicates compression. In panel (a), as the walls move together, the three droplets attach to the walls due to depletion and thus exert tension on the walls, resulting in the negative force peak seen in panel (e) at distance $(2 + \sqrt{3})R \approx 3.73$. As the top wall continues to move closer to the bottom wall, the droplets go through equilibrium [panel (b)], and eventually the walls begin compressing the droplets [panel (c)], leading to rise in the force on the walls. At the peak of the force, the horizontal bond between the two left particles is under tension. When this bond between the two bottom droplets breaks, the force rapidly drops [panel (d)]. 34

2.4 (a) Sketch of small displacements of three droplets. (b) Free body diagram of forces acting on the top left droplet. $F/2$ is from the wall, with the other $F/2$ contribution acting on the bottom droplet. The vertical spring is stretched by $2\Delta y$, so accordingly the force indicated as $2k_2\Delta y$ is a tension force from the bottom droplet. The $k_1\Delta r$ force is a compression force from the right side droplet. As the droplets are monodisperse $\theta = 30^\circ$. Changes in θ for small Δx and Δy can be ignored to first order. 37

2.5 A 7×7 droplet array in its initial configuration undergoing a row reduction. In (a) we can see that the array is being compressed between the walls, as evidenced by the red compression bonds. The blue tension bonds run parallel to the walls, with the depletion force preventing the crystal from spreading along the direction of the walls. In (b) a global fracture has occurred, splitting the crystal into four separate pieces and relaxing the forces; many droplets are close to their equilibrium separation distance. In (c) the crystal settles into a 6×8 hexagonal-close-packed configuration and the depletion forces pull the droplets and walls closer together. The extra droplet is in the second column. Movie S1 in the Supplemental Material of the paper this chapter is based on[21], depicts the compression process for the array shown in this figure. 40

2.6 Force on the left wall as a function of the distance between the walls for a 7×7 monodisperse droplet array. The distance starts large and decreases, so time increases from right to left. Each successive peak is taller than the last, due to the increased amount of bonds that need to be broken. The blue and red slope are used to obtain k_{eq} , as in seen in the inset. 41

2.7 Linear fit for the compression of the equivalent spring constants, as a function of the aspect ratio of the array $q/(p + 1)$ for 49 droplet array. Using Eqn. 2.32 and the linear fit gives us the spring constant for a single droplet, $k_1 = 7.08 \pm 0.6$ 43

2.8 Evolution of the normalized peak height as a function of $(p^3 + p^2)^{-1/2}$ for a different variety of starting configurations. The solid line represent the values predicted by Eqn. 2.37. The discrepancies at the right side are due to the increasing influence of viscous forces, which become more significant for large arrays with small p . The right-most data correspond to $p = 4$. The hollow diamond and hexagonal markers correspond to 18×18 and 16×16 arrays, with wall speeds half of those used for all other simulations. For the compression of bigger arrays at low p , the decreased speed, and therefore, decreased viscosity, results in smaller force peaks. 46

2.9 Evolution of the force profile as the defect fraction ϕ increases. The more bidisperse the aggregates becomes the noisier the force profile is; the individual fracture events involving many droplets split into a broad sequence of smaller fractures. The images in the right columns are snapshots from the state prior to compression of the system at distance 8. 49

2.10 $\Delta N(\phi)$ normalized by the fitting parameter ΔN_{peak} for five different droplet arrays. The dashed line corresponds to the prediction of Eqn. 2.39. Four of the data sets correspond to simulation data, while the points with the star marker are from the experimental data of Ono-dit-Biot *et al.* [20]. The experimental droplet array consists of 23 particles in three columns containing 8, 7, and 8 particles. 50

2.11	$N^{p_{ini} \rightarrow 1}$ (the amount of fracture events from the initial number of rows to one) as a function of the polydispersity δ for the discrete 4×5 bidisperse case used in Fig.2.10, and a continuous size distribution. The amount of fractures events depends on the chosen size distribution, with the discrete case increasing somewhat lineally, while the continuous case grows nonlinearly. The dashed line corresponds to the prediction of Eqn. 2.39. For the bidisperse case $\delta(\phi)$ is not symmetric between ϕ and $(1 - \phi)$, so thus Eqn. 2.39 has two branches as shown [105].	52
2.12	Successive images of of a 20 droplet aggregate undergoing a second row reduction, from the original 4 rows by 5 columns configuration. By panel (c) we can see the formation of two fractures, which are misaligned as they propagate through out the array. Thus the collapse in (d) is disordered, and the final packing with a defect in (e).	54
2.13	Successive images of a 36 droplet aggregate, undergoing its third row reduction from the original six by six configuration. By panel (c) we can see the formation of two fractures, which are misaligned as they propagate through out the array. Thus the collapse in (d) is disordered, and the final packing with a defect in (e).	54
2.14	The fraction of row reductions observed to have competing fractures as a function of $1/N^{1/2}$, using the number of droplets N . The data correspond to initially square arrays such as the array in Fig. 2.5(a). The error bars reflect the standard deviation over five runs.	56

2.15 The fraction of competing fractures as a function of aspect ratio using $N = 144$ droplet configurations. The aspect ratio is defined as q/p , with a low aspect ratio corresponding to “tall” configurations (many rows parallel to the walls, with the walls starting quite far apart), and high aspect ratios to “wide” configurations (few rows between walls that start close together). The error bars reflect the standard deviation over five runs. 57

2.16 The fraction of competing fracture as a function of the angle between the two walls, for three different droplet array sizes as indicated. The data suggest a slight angle between the walls can dramatically decrease the frequency of competing fractures. 58

3.1 Sample image illustrating the process used for image analysis and particle tracking. (a) Photograph of the experimental device with a size distribution already in place under normal lightning conditions. (b) Photograph of the same frame using green/yellow lightning to highlight the red rectangles painted on the particles. We have superimposed blue rings to illustrate the results of our particle tracking. The largest particle on the left has a diameter of 5.7 cm, with its rectangle being 3.5 cm long. 65

3.2 Top down schematic of the experimental device, set up in the "L" configuration. Plungers have been placed at each end of the flow geometry, this allows us to push the particles back and forth. The plungers both move at a set speed $v_p = 0.22\text{cm/s}$ and maximal extension of 10.7 cm. In Fig. (a) we show the dimensions of our system. Fig. (b) shows as red quarter circle, what we call the closed corner, or the bottom right corner. The purple 3/4 circle represents the "upper right corner" or "open corner". Finally the dashed square shows an approximate area of what we will refer later on as the "central" area, region or zone. The dashed square and circular circle are illustrative representations meant to give an approximate location of the these canal features. 67

3.3 A top down sketch of the experimental device, setup in the "L" configuration. Plungers have been placed in such a manner as to block the outlets and study the sloshing back and forth of a given particle configuration. . . 69

3.4 Histogram for the three continuous distribution of particles, C1, C2 and C3. These distributions are built using particles sizes "continuously", starting from R_0 and R_1 , to a larger particle size, including all radii in between. . . 71

3.5 Mean displacement field $\Delta\vec{r}_{\text{mean}}(x, y)$. The displacements are calculated using $\Delta t = 5\text{s}$. The bold line on the scale bar indicates $\Delta r_p = v_p\Delta t = 1.1\text{cm}$, the displacement corresponding to the plunger motion over Δt . On the lower right inlet, we observe a plug like flow closer to the plunger, which then turns into a more shear like flow as the particles turn the corner. Closer to the lower left corner we see an area with almost no displacements, signified by the shorter arrows with the darker color. 73

3.6	<p>Snapshots showing the different quantities measured in the flow for the bidisperse size distribution (left column panels) and the T4 size distribution (right panels). From top to bottom, (a,b) display the displacement of each particle, (c,d) show the nonaffine displacement, and (e,f) show D_{\min}^2 for each disk. The plunger at lower right enforces that contacting particles move with velocity v_p, and thus have displacements $\Delta r_p = 1.1\text{cm}$. For the bidisperse distribution, regions of higher nonaffine motion (Δr_{NA} or D_{\min}^2) are typically associated with locations of higher strain. For the tridisperse distribution, the largest particles generally have less nonaffine motion, but nearby smaller particles often have more nonaffine motion. For both distributions, the flow near the moving plunger (lower right) is plug flow: thus no shearing and no nonaffine motion.</p>	75
3.7	<p>Two examples of our neighbor definition. We use the closest 15 particles as neighbors of the reference particle. Magenta indicates the reference particle. Yellow indicates the neighbors of our largest particle, R_8, on the left. The cyan particles show the neighbors for the smallest particle, R_0, on the right.</p>	80
3.8	<p>(a) The mean magnitude of the nonaffine motion $\Delta r_{\text{NA}} /\langle R \rangle$ and (b) $D_{\min}^2/\langle R \rangle^2$, both as a function of the normalized particle size $R/\langle R \rangle$. Smaller particles have higher Δr_{NA} and D_{\min}^2 than larger particles. This is because larger particles are more likely to follow the mean flow, which forces smaller particles to maneuver around these large particles. To have enough data for a meaningful result, we average the observations of the three largest particles in C3 together.</p>	83

3.9 Δr_{NA} is shown in (a,c) and D_{min}^2 in (b,d), both as a function of distance(d_{0i}) from the edge of a reference particle with radius R to all other particles. The top panels (a,b) correspond to the bidisperse distribution, and the bottom panels (c,d) to the T4 distribution. At $d_{0i} = 0$, there's a valley for all cases, corresponding to particles in direct contact to the reference, resulting in low Δr_{NA} and D_{min}^2 , due to the tight packing. There's a another valley at $d_{0i} = 2R_0$, which in this case corresponds to a buffer of one R_0 between the particles, but are otherwise in close packing, causing the minimum. In between these valleys we find a peak at $d_{ij} \sim 0.75$ cm. These peaks are a good tool to measure the effect the reference particle has on its closest neighbors. This measurement is affected by particle size, an effect that can be seen for all distributions shown here, with larger particles having higher peaks. This can be seen by the differently colored curves. As shown in the legend, the blue curve correspond to the R_8 particles, while red and black to R_0 and R_1 , respectively. The dashed line shows the average value for all particles. 85

3.10 These graphs show how particles of size $R/\langle R \rangle$ influence the motion of their neighbors. (a) Peak $(\Delta r_{\text{NA}} - \langle \Delta r_{\text{NA}} \rangle) / \langle R \rangle$. (b) Peak $(D_{\text{min}}^2 - \langle D_{\text{min}}^2 \rangle) / \langle R \rangle^2$. The symbols correspond to distinct particle size distributions, given by the legend in (a). The peak height is measured from data similar to that shown in Fig. 3.9, where the peak is measured for $d_{0j} < 2R_0$ from the reference particle. Larger particles have stronger influences on their neighbors. Error bars are only shown when the error bar is larger than the scatter symbol. . 86

3.11	(a) $\Delta r_{\text{NA}}/\langle R \rangle$, and (b) $D_{\text{min}}^2/\langle R \rangle^2$, as a function of the polydispersity for each size distribution. For $\Delta r_{\text{NA}}/\langle R \rangle$, we see no relation to polydispersity, averaging to a value of 0.37. On the other hand $D_{\text{min}}^2/\langle R \rangle^2$ shows a positive relation with polydispersity. The dashed line is a least-squares fit to the data; see text for details.	87
3.12	Average $\Delta r_{\text{NA}}/\langle R \rangle$, Fig.(a), and $D_{\text{min}}^2/\langle R \rangle^2$, panel Fig.(b), for the central zone for various time intervals, on log-log scale, for all size distributions. The lines indicate power-law scaling with exponents as labeled. All distributions share similar exponents and their corresponding curves do not cross each other for the observed Δt	89
3.13	Color maps for $\Delta t = 5$ s, Fig.(a), $ DF(\Delta t = 5 \text{ cm}) $, Fig.(b) and $ D_{\text{min}}^2(\Delta t = 5 \text{ cm}) $ on the top row. On the bottom row we show the quantities but with $\Delta t(x,y)$, Fig.(d), such that $ DF(\Delta t(x,y)) \approx df_0$, Fig (e). The final color map, Fig.(f) corresponds to $D_{\text{min}}^2(\Delta t(x,y))$. We see at the top row that D_{min}^2 is strongly correlated to $ DF(\Delta t = 5 \text{ s}) $, while in the case for $\Delta t(x,y)$, the time interval matrix correlates strongly to $D_{\text{min}}^2(\Delta t(x,y))$. In this last case we manage to obtain a somewhat more spatially homogeneous matrix closer to the center areas.	91
3.14	(a) $\Delta r_{\text{NA}}/\langle R \rangle$ and (b) $D_{\text{min}}^2/\langle R \rangle^2$ as a function of polydispersity for all size distributions. In this figure $\Delta r_{\text{NA}}/\langle R \rangle$ and $D_{\text{min}}^2/\langle R \rangle^2$ are calculated for each particle using $\Delta t(x,y)$. In contrast, Fig. 3.11 shows similar results using a fixed $\Delta t = 5$ s. The dashed line in (b) is a least-squares fit to the data; see text for details.	95

4.1	(d) Representative image showing a clog in simulations, with a colour overlay: Red droplets indicate the clogging arch, blue droplets represent remaining droplets, yellow droplets remain attached to the aggregate due to cohesion. In this particular simulation $w/d = 3.25$, and $w/\delta = 5.00$. (b) Representative experimental image showing a clog, with $w/d = 8.8$ while $w/\delta = 2.86 \pm 0.07$. (c) Side and top view schematic diagram of the experimental chamber. Droplets are deposited and float to the bottom of the top slide while the chamber is held horizontal. (d) During the experiment, the chamber is rotated to a desired tilt angle which drives the droplets due to the buoyant force.	103
4.2	Clogging probability of (a) simulations and (b) experiments with $w/d = 3.0$ for a range of cohesive strengths as a function of strength of the effective gravitational forces g , and effective buoyant forces $\sin \theta$. Solid lines represent fits of Eq. 4.8 to the data. The value of the driving force where the probability of clogging is $P_{\text{clog}} = 1/2$ as a function the cohesive strength is shown for c) simulation and d) experiment. . . .	106
4.3	Clogging probability for a range of cohesive strengths as a function of the hopper opening width over the droplets diameter(w/d), for constant g . Solid lines represent fits of Eq. 4.11 to the data. For increasing ϕ_c wider hopper exits are needed in order to avoid clogging, meaning that the particles clog easier if they are more cohesive.	109
4.4	w^*/d as a function of δ . Close to $\delta \approx 1$ there's a change in the behaviour for w^*/d , as we expected. We have therefore chosen to fit these behaviours differently. The black dashed line represents the linear fit for low cohesion, while the red dashed line is the linear fit for high cohesion.	110

4.5 Figs. (a) and (b) show the mean avalanche size before a clog occurs plotted against the dimensionless ratio w/δ^* , for simulations and experiments, respectively. The solid line is a fit to Eq. 4.17. Figs. (c) and (d) shows $\ln(\langle s \rangle + 1)$ as a function of w/δ^* , for simulations and experiments respectively. Using Eq. 4.18 we were able to fit the data, dashed lines in Figs.(c) and (d), and obtain the parameter to plot Eq. 4.17 in Figs.(a) and (b). Dashed lines show a plateau at 190 droplets. For the simulations the empty symbols are data point with variable g , whereas the stripped data points are simulations with $N = 95$ for the circles, and $N = 285$ for the squares. 112

4.6 Probability of clogging as a function of w/δ^* . The data for both simulations and experiments collapses onto one master curve. The dashed line represents a fit to Eq. 4.20 using $A = 0.12 \pm 0.03$ and $B = 0.029 \pm 0.001$, for the simulations, and $A = 0.4 \pm 0.1$ and $B = 0.70 \pm 0.09$ for the experiments. For the simulations the empty symbols are data point with variable g , whereas the stripped data points are simulations with $N = 95$ for the circles, and $N = 285$ for the squares. 115

A.1 Figures showing the correlation between averaged $|\Delta\theta|$ against different quantities measured in the flow for the bidisperse size distribution (left column panels) and the T4 size distribution (right panels). From top to bottom, (a,b) display the correlation between $|\Delta\theta|$ and the displacement of the particles, (c,d) show $|\Delta\theta|$ vs nonaffine displacement, and (e,f) show $|\Delta\theta|$ vs D_{\min}^2 . The red data points correspond to the bins in the central zone as outlined by Fig. 3.2, while the blue data points correspond to all bins outside this area. Regarding the displacements (a,b), there does not seem to be a strong correlation between change in orientation of the particles and the magnitude of the displacement. However for both Δr_{NA} and D_{\min}^2 there seems to be a degree of positive correlation with $|\Delta\theta|$ 124

A.2 $|\Delta\theta|$, as a function of the polydispersity for each size distribution. We can see that there is no clear relation between $|\Delta\theta|$ and polydispersity, averaging to a value of 0.046. 125

List of Tables

- 3.1 Table with all the disks size distributions used in this Chapter. The first column shows the name of each distribution, in the second and third column we show the size and number ratio for all particles, respectively. The last column shows polydispersity of each distribution. For the C1 size ratio is; 2 : 3 : 4 : 5 : 6, for C2; 2 : 3 : 4 : 5 : 6 : 7 : 8, and for C3; 2 : 3 : 4 : 5 : 6 : 7 : 8 : 9 : 10. For more information about the number ratio of C1,C2 and C3, Fig. 3.4 shows a histogram with the amount of particles of each size in these distributions. 70

Chapter 1

Introduction

Soft condensed matter refers to any material in states of matter that are neither simple liquids nor crystalline solids[1]. These types of materials are defined by having properties of both liquid and solids. An example would be a pile of shaving cream, composed of air and soapy water, and if left undisturbed in a pile will hold its shape, but can be sheared and made to flow if enough force is applied. Such materials are ubiquitous, occurring naturally such a wide variety of natural oils, biological tissue, sea foam, and mud and soil. On the other hand, these materials are also incredibly useful for industry, for example: lubricants, cements, polymers and adhesives. Soft materials are also various products used in our daily life, like mayonnaise, toothpaste, whipped cream and jello. Mayonnaise, for example, is an emulsion, with the egg yolk acting as a surfactant, that stabilizes the oil droplets against coalescence with continuous phase liquid, usually vinegar or lemon juice.

While many soft matter systems are often characterized by their microscopic length scale, and the importance of thermal fluctuations, not all systems share these features, for example: granular systems and foams, whose particles are too big to be affected by thermal forces, and for which its particle's size can be placed on the macroscopic scale. Figure 1.1 shows various common examples of soft condensed

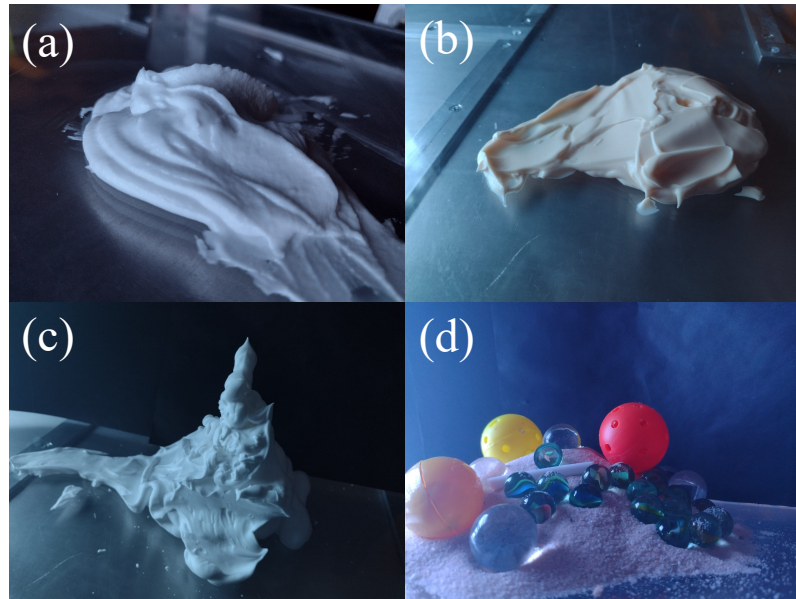


Figure 1.1: Examples of soft condensed matter systems. Starting from the top left (a) toothpaste, a colloid composed sodium fluoride, antibacterial agents, etc., as the dispersed phase with water as the dispersion medium. (b) Mayonnaise, an emulsion made from oil, egg yolk and vinegar. (c) Shaving cream, a foam made using soaps and oils. (d) A pile of sand, glass marbles, rods, plastic spheres and an ellipsoid as an example of a granular system.

matter.

Below are some systems classified under the soft condensed matter umbrella, in which different forces and mechanism come into play, and which occur at a wide range of scales:

- Colloids: A phase separated mixture, generally consisting of solid particles between 1 nm to 10 μm in size, dispersed in a liquid medium. At these scales the thermal motion is relevant. Some examples of colloids include: toothpaste, paint, blood, etc [1]. Figure 1.1(a) shows toothpaste, a colloid that has sodium fluoride, antibacterial agents, etc., as the dispersed phase, with water as the dispersion medium.
- Emulsions: Similar to colloids, an emulsion is a mixture of more than one liquid, which are normally immiscible, with one of them being dispersed as droplets. Surface forces are now relevant, while thermal forces depend on the particle

scale. Some examples include: mayonnaise, vinaigrettes, ointments, etc. Figure 1.1(b) has mayonnaise as an example of an emulsion, with the water in an egg yolk acting as the dispersion medium and the oil as the dispersed phase.

- Foams: For this case the disperse medium is a gas and the continuum medium is a liquid. Examples of foams include: shaving creams, foam at the tops of beers, etc. Figure 1.1(c) shows shaving cream, a household example for air-in-liquid foam, in this case the liquid enclosing the air is soapy water.
- Granular systems: a conglomeration of discrete solid macroscopic particles, in air or vacuum. The lower limit for the particle size is about $100 \mu\text{m}$; for these scales thermal fluctuations are not important, but friction is. A wide variety of these systems are present in both nature and industry, with the grains having a wide diversity of shapes, sizes, roughness, etc. Example of these systems include: sand, gravel, log dams, glaciers, etc. The last picture in Fig. 1.1(d) shows a pile of sand, glass marbles, rods, plastic spheres and an ellipsoid as an example of a granular system. Sand grains size generally ranges from 0.0625 mm to 2 mm , while the glass marbles where 2 cm and 5 cm in diameter. The plastic spheres were 7 cm across.

The physics of soft matter has been a field that has developed over the last few decades, and characterizing the various properties and behaviour of these kind of systems is still the focus of many researchers, with the challenges arising from the complex ways in which the constituents components of these systems can interact, often requiring a multidisciplinary approach.

Among soft condensed matter, there are also amorphous materials, and among these materials there are amorphous solids, or disordered solids. As the name implies, these kinds of materials do not posses any kind of long range order or structure, in contrast to crystalline solids, characterized by their periodic crystal structure[2, 3]. Due

to their spatial heterogeneity, robust and coherent theoretical frameworks are scarce compared to the “traditional” condensed matter, which leverages the periodicity of crystalline structures to build an elegant and coherent theoretical description[3].

Amorphous materials can be at times composed by particles with a variety of properties, such as aspect ratio, concavity, roughness, density, and particle size among many other features. We will focus particularly on the size diversity of the particles in a system, and to quantify this we will use polydispersity. For a given particle size distribution $P(r)$, with r being the particle’s radius, polydispersity is defined as:

$$\delta = \sqrt{\langle \Delta r^2 \rangle} / \langle r \rangle \quad (1.1)$$

where $\Delta r = r - \langle r \rangle$, and the moments of r (and Δr) are given by $\langle r^n \rangle = \int r^n P(r) dr$ (and $\langle \Delta r^n \rangle = \int \Delta r^n P(r) dr$). Fig.1.2 shows a variety of polydisperse circle distributions.

Examples of highly polydisperse systems are abundant in both nature and in industry, such as gravel, soil [4], sea ice [5], sand [6], and for industry, we have a wide variety of gels, foams, emulsion and colloids [7–9]. Additional examples were also mentioned above.

In summary, polydispersity plays an important role in the behaviour of various colloidal, granular, and emulsion systems, with the higher polydispersity values resulting in qualitatively different behaviour from more conventional monodisperse and low bidisperse systems, which will be shown in this dissertation. These changes in behaviour means that models and ideas that work in systems with lower polydispersity might not work to the same degree in systems with higher polydispersity. Considering that many natural and industrial systems have a high diversity of particle sizes, achieving a better understanding of the effect of polydispersity on these systems is of vital importance.

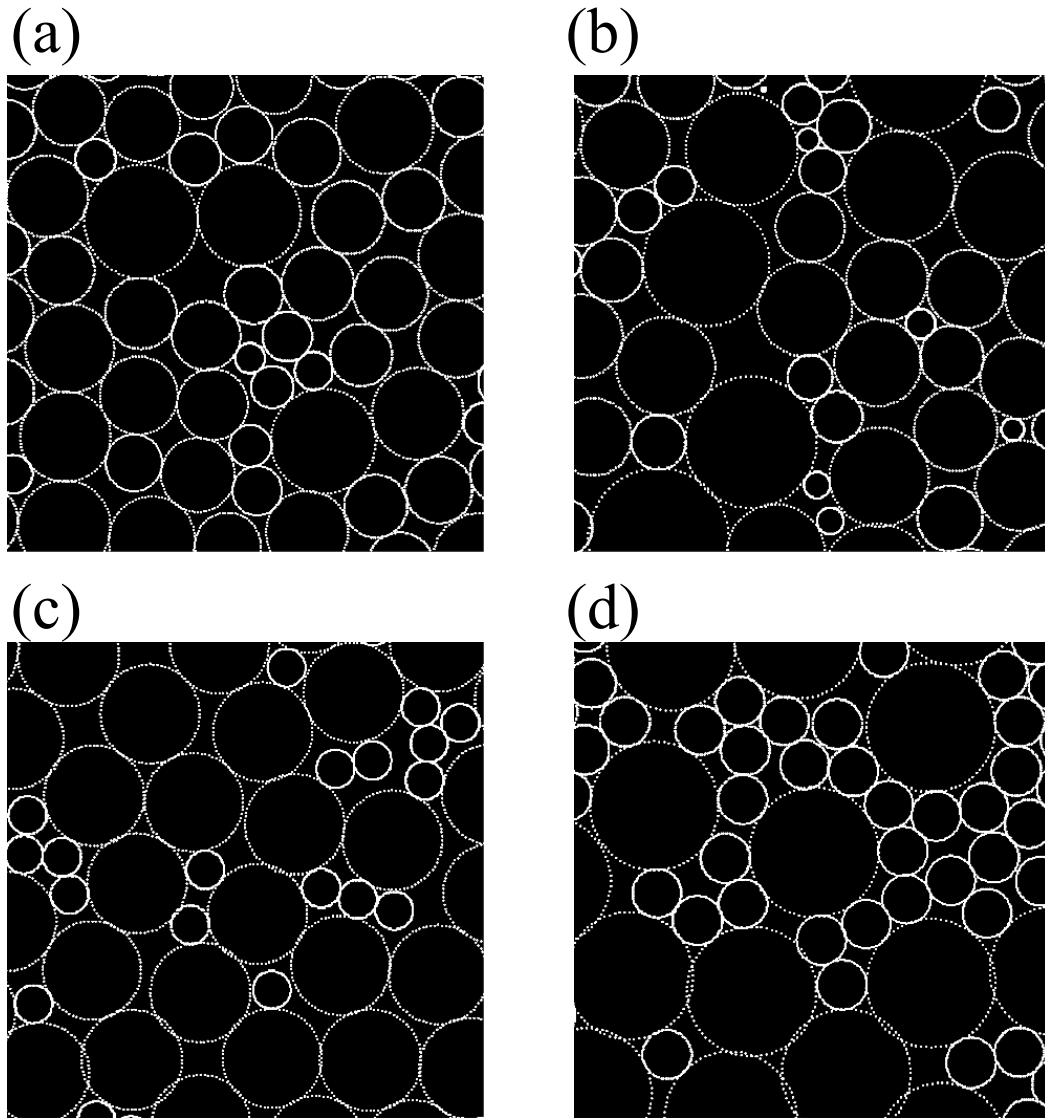


Figure 1.2: Examples of polydisperse distributions of circles. Figs.(a) and (b) show a pair of Gaussian size distributions with polydispersity $\delta = 0.5$, and $\delta = 0.25$, respectively, both with average radius $\langle R \rangle = 1$. Figs. (c) and (d) show two bidisperse distributions with size ratio 1 : 2.6, and with polydispersity $\delta = 0.32$ and $\delta = 0.5$, respectively.

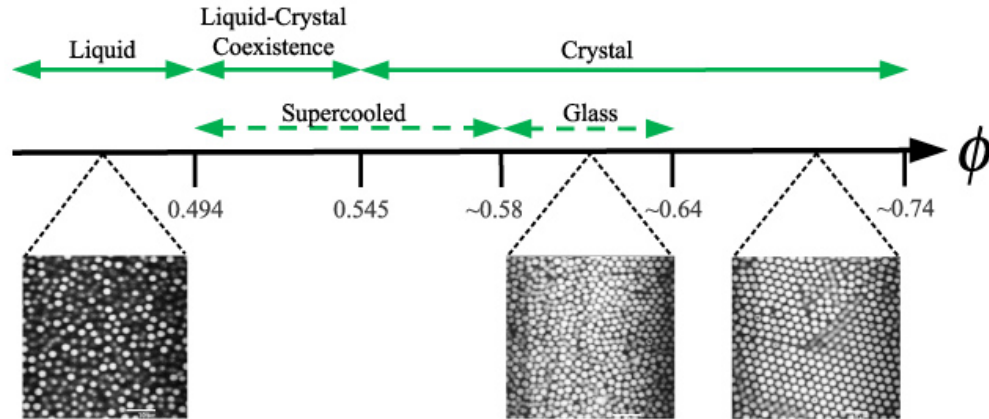


Figure 1.3: Phase diagram of hard spheres as a function on the volume fraction, Φ . . Solid arrows indicate equilibrium states, whereas dashed arrows are non-equilibrium states. We note that for the glassy state to exist, some polydispersity is required in the system. The bottom inset images are confocal micrographs. Republished with permission of IOP Publishing, Ltd, from “The physics of the colloidal glass transition”, Gary L. Hunter and Eric R. Weeks [11]; permission conveyed through Copyright Clearance Center, Inc..

1.1 Colloidal crystals and glasses

Among the examples given above for soft materials, both colloids and emulsions were listed. To reiterate, these materials consist of a continuum liquid medium, with a dispersed phase. For colloids, the dispersed phase is made of solid particles, for emulsions this phase is made of another immiscible liquid. The sizes of these particles usually range between 10nm to 10 μ m in radius, which makes these systems directly observable using optical microscopy methods (see Fig.1.3), as well as other indirect observation methods, like light scattering [10]. Due to their size colloidal particles interact with each other and their environment through a variety of forces, repulsive forces are often present in these systems (such as surface tensions, present in steric stabilized colloidal suspensions) and attractive forces (such as depletion, which occurs when particles many times smaller than the dispersed medium are present in high enough concentration).

Due to these systems being large enough to be imaged directly, they have be-

come an essential tool for modeling systems which are many times smaller[12–14]. Of these systems we are particularly interested in the use of colloids and emulsions to model both crystals and glasses. Modeling of glasses is of particular interest as the continuous transition from viscous liquid to a "solid" glass, has yet to be fully understood [15, 16]. This glass transition is different from crystallization, which has a well defined thermodynamic transition and the formation of a crystalline structure [15]. The first time colloidal suspensions were used to model crystals with a glass transition was in the 1980s[12, 13]. In contrast to "regular" glasses, which undergo a transition as a function of temperature, their colloidal counterpart undergo this transition as a function of concentration. At a high enough concentration colloidal systems will begin to self aggregate and form crystals, and with a polydispersity of at least 5%, these systems can also undergo their own glass transition. This has made them great modeling tools to study the glass transition, as well as the various properties of glasses and crystal with defects.

Emulsions are often used for a similar purpose, these systems too have been use to great success to model various glassy and crystalline systems, due to their size allowing for direct imaging. Simultaneously these particles are still susceptible to a variety of forces used to model different systems. Emulsion models can also be assembled into a variety of configurations to probe the different properties of glassy and crystal systems. One particular advantage of using emulsion droplets to model particles arrays, is the control over the radii of these droplets that can be achieved [17–20], allowing for excellent degree of control over the size distribution of the droplets composing the model glass.

As mentioned before in this subsection, in order to achieve a glass transition in these model systems a certain degree of polydispersity must be present. Extensive research has been dedicated to analyzing the effect of polydispersity on the glass transition, the changing properties of both crystals and glasses, and the extent the

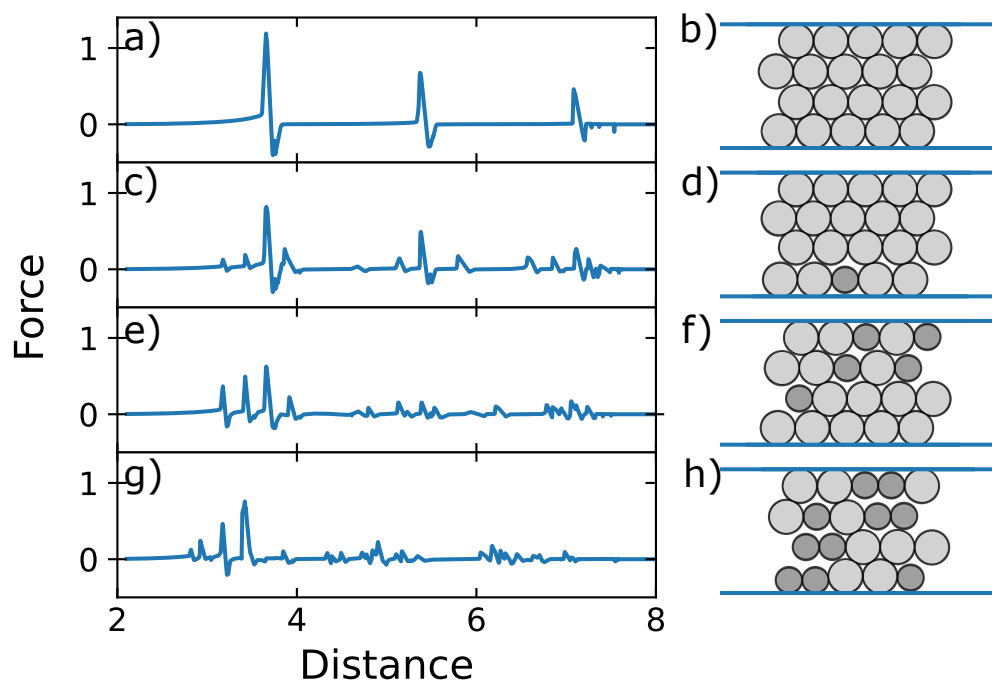


Figure 1.4: Force needed to compress an array of droplets as the distance between the walls decreases. We can see that the maximum force needed to deform the droplets decreases the more glassy the array of droplet becomes. This behaviour will be further discussed in Chapter 2.

introduction of differently size particles can produce in perfectly ordered systems. Figure 1.4 shows how the properties of a crystal/glass is affected by the amount of defects and polydispersity of its constituent particles. As the system becomes more glassy the maximum amount of force that needs to be exerted to compress the material is lowered.

Among the many questions still present regarding the behaviour of these glassy materials is their mechanical response to applied stress, particularly to an applied compressive force. In Chapter 2 we use numerical methods to simulate an array of colloidal particles, and characterize their response to compression under different conditions, both for a crystalline aggregate as well as bidisperse and polydisperse systems with a Gaussian distribution. The work presented on Chapter 2 has been published in “Physical Review E” [21].

1.2 Amorphous flow: Shearing of soft glassy materials

The flow and dynamics of amorphous materials such as foams, colloidal glasses, or granular systems display complex flow features. This behaviour is due to the spatial heterogeneity in the system. A variety of common granular flow systems are shown in Fig. 1.5. At low enough applied strain, the system will respond like an elastic solid, undergoing minute elastic deformations, however once enough force is applied to the system, the particles are made to flow in something that more closely resembles a liquid. Due to the complexity of particles interactions a global model of granular flow is still being developed, although various pictures of these dynamics have started to emerge [22–26]. In these models, flows occurs through a succession of elastic deformations and local irreversible plastic plastic deformations, which eventually lead to a macroscopic rearrangement in the material [27–29].

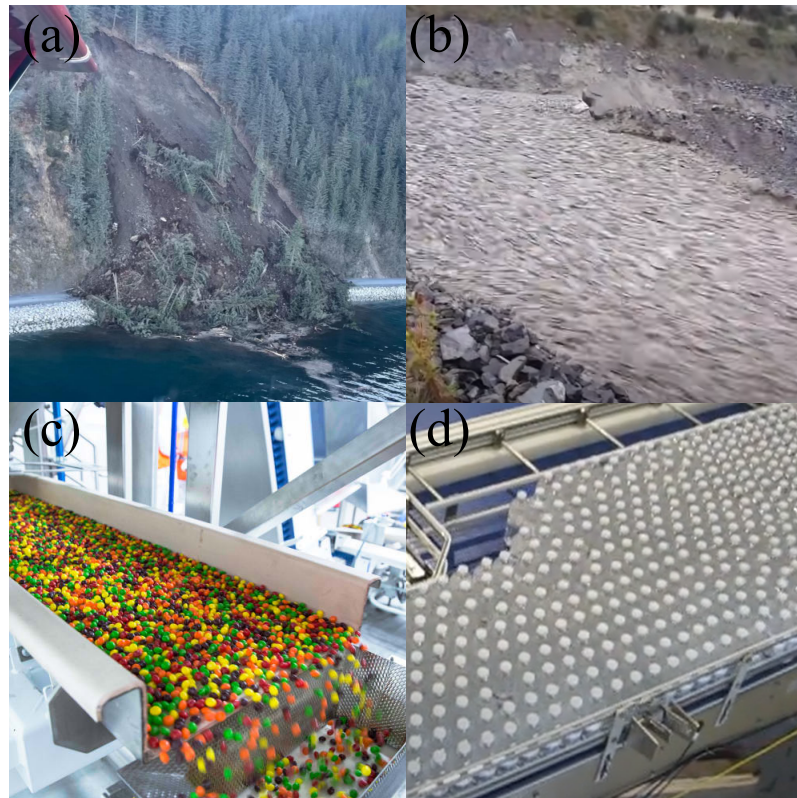


Figure 1.5: Examples of granular flow. Fig. 1.5(a) shows a landslide in Alaska after an earthquake, photo by *icefogger*, republished under creative commons license, original picture link(circle.tocircle.blog/2022/05/11/alaska-time/). Fig.(b) shows a stream of rocks in New Zealand after a particularly heavy storm, picture by Donna Field. Figs.1.5(c) and (d) show examples of granular flow in a Skittles factory (photo courtesy of Mars Wrigley) and a water bottling facility respectively (Image capture from *StrongPoint Automation* on *youtube*). Most granular flows found in both nature and industry correspond to this regime of densely packed particles interacting through contact forces,

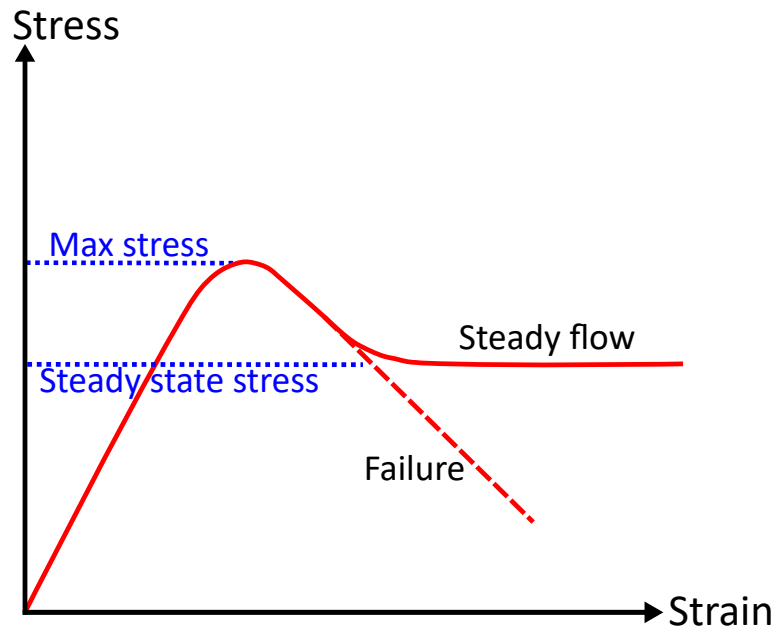


Figure 1.6: Sketch of macroscopic response of amorphous materials to external load. Failure and steady flow correspond to brittle and ductile materials respectively. At a certain maximum amount of stress the material yields and begins to deform. If the system begins to flow the stress now fluctuates around at a steady state stress value.

As stress is applied, the material will begin to deform elastically. At this point, if we stop applying stress, the material will go back to its initial configuration, responding like a Hookean solid. However, if we apply stress past a threshold the material deforms plastically and either begins to flow, if the material is ductile, or fail/break if the material is brittle. In Fig.1.6 we show a sketch of what this curve can look like for some materials. Once plastic deformations begin to occur locally, the release of stress will propagate in certain directions, which might trigger further plastic deformations close to the yielding point as stress is released through the system. Therefore local stress relaxation can trigger cascading events that have long range effects. For these systems therefore the local behaviour and rearrangement for the particles plays a major role in the macroscopic behaviour of the material. An example of a propagation stress releasing event in a brittle material is shown in Fig. 1.7. On the other hand if the material is ductile this applied stress will result in a granular flow, where a flow

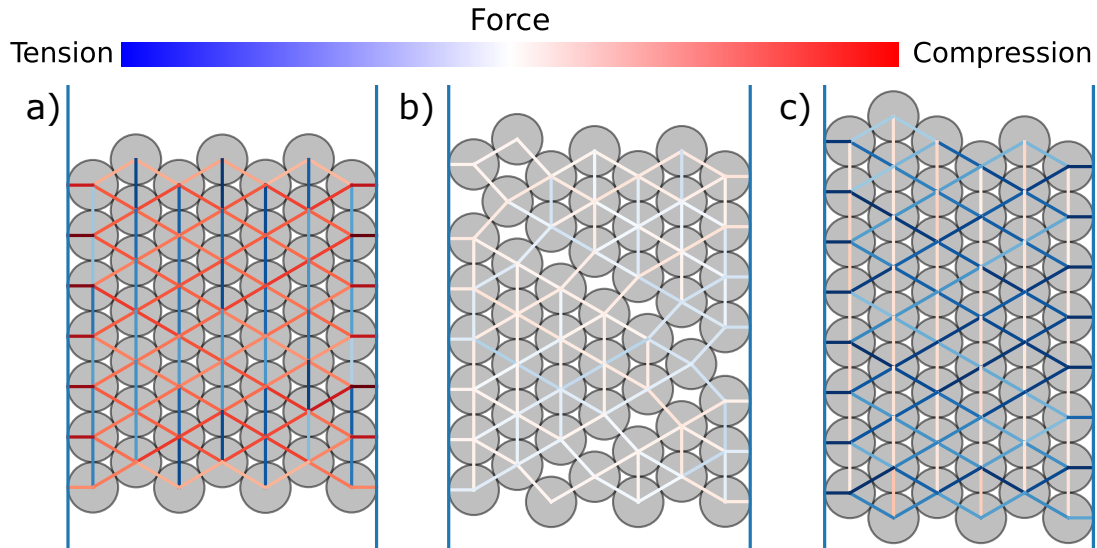


Figure 1.7: A brittle crystalline formation of droplets yielding under applied stress. Prior to reaching the stress limit the array deforms elastically. Once the stress threshold is reached the stress is released locally resulting in cascade of stress relaxation in the form of a propagating fracture. This phenomenon will be further discussed in Chapter 2.

similar to what is observed in traditional liquid is observed. In this regime particles interact with each other through friction and collisions. This liquid like behaviour is well illustrated by Figs. 1.5. The examples in Fig.1.5(a) shows a stream of rocks in New Zealand after a particularly heavy storm, and Fig.1.5(b) shows a landslide in Alaska after an earthquake. In an industrial setting, Figs.1.5(c) and (d) show examples of granular flow in a Skittles factory and a water bottling facility respectively. Most granular flows found in both nature and industry correspond to this regime of densely packed particles interacting through contact forces, and which flow once a stress threshold has been crossed.

The properties of deformation and flow in granular materials is, as stated earlier, tightly related to the complex network of inter particle interactions, therefore the properties of the particles which constitute the systems are highly relevant[30, 31]. When compared to more monodisperse systems, the behaviour of highly polydisperse amorphous systems and their response to applied stress, have been shown to be

qualitatively different for both brittle materials[20], and sheared granular systems[32]. In Chapter 3 we study the quasi 2D granular flow of polydisperse particles. We investigate the effect of polydispersity on the plastic deformation of the amorphous system, such as non-affine flow, and particle rearrangement.

1.3 Amorphous Flow: Hopper discharge and Clogging

As mentioned previously in this chapter amorphous and granular materials are ubiquitous in our daily lives, nature and industry. It therefore follows that the flow of these systems takes up an equally important role[6, 33–35]. However due to the complexity of inter particle interactions the dynamics of these systems are still not very well understood[36], for example the flow of sand differs qualitatively from a flowing fluid[36–38]. More specifically the flow of granular media through narrow openings has great importance to various industrial fields, like the agricultural, culinary and mining industries[9, 39–44]. See Figs. 1.8 for a variety of examples.

A particularly important difference from fluid flow is the clogging of a granular system when the exit orifice is below a critical width for the opening, which, depending on a variety of factors, occurs when the exit orifice is in the 3 – 6 granular particle diameter range[42, 45]. The interruption of the flow is stopped, is due to the formation of arches of particles, in two dimensions, or of domes, in 3D. To give an everyday example to this behaviour, recall how often do we shake a salt holder to break up the arches and pour the salt. Determining when a clog can occur is, as can be imagined, incredibly useful not only to predict when the flow will stop, but the size of the exit can also induce intermittent interruptions in the flow, and affect the mean flow rate itself[42, 45, 46].

The mean flow rate is a function of the difference between the opening size to the

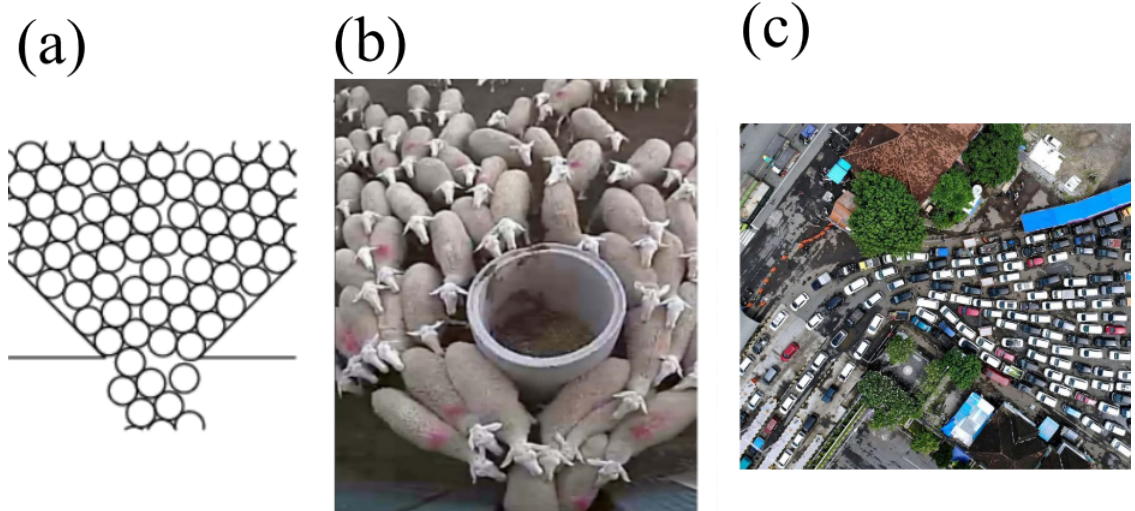


Figure 1.8: Examples of clogging in variety of systems. Fig.(a) shows the outflow of non-frictional spheres out of a 2D hopper. Fig.(b) shows sheep flow through a narrow gate, with an obstacle in front of it. Republished with permission of Springer Nature under a Creative Commons license, from Scientific Reports, “Clogging transition of many-particle systems flowing through bottlenecks”, Iker Zuriguel *et al.* [45]. Finally Fig.(c) shows a traffic clog in Indonesia, original photo by Fikir Yusuf.

critical size at which clogging occurs[39, 42]. We note that experiments suggest that rather than there being a critical opening size, the probability of the hopper clogging becomes exponentially small[47, 48]. There is a wide variety of factors that affect the clogging process, some intrinsic to the hopper or particles themselves, such particle shape and size[49–51], friction between the particles and the hopper[45], particle softness[49, 52], among others[45]. On the other hand, the clogging probability and flow properties are also affected by driving forces, like gravity, and by forces which might lead to the break up of the arch or dome structures, like shaking[45, 49]. We are particularly interested in the effect cohesive forces have on the clogging probability and discharge of a 2D hopper system. Cohesive forces between particles are fairly common in granular systems, for example small powders are subjected to cohesive forces due to electrostatic charges and Van der Waals forces[53]. In larger particles particles tend to clump together due the effect of liquid capillary bridges[54]. These cohesive effects can greatly affect hopper flow and clogging[55, 56].

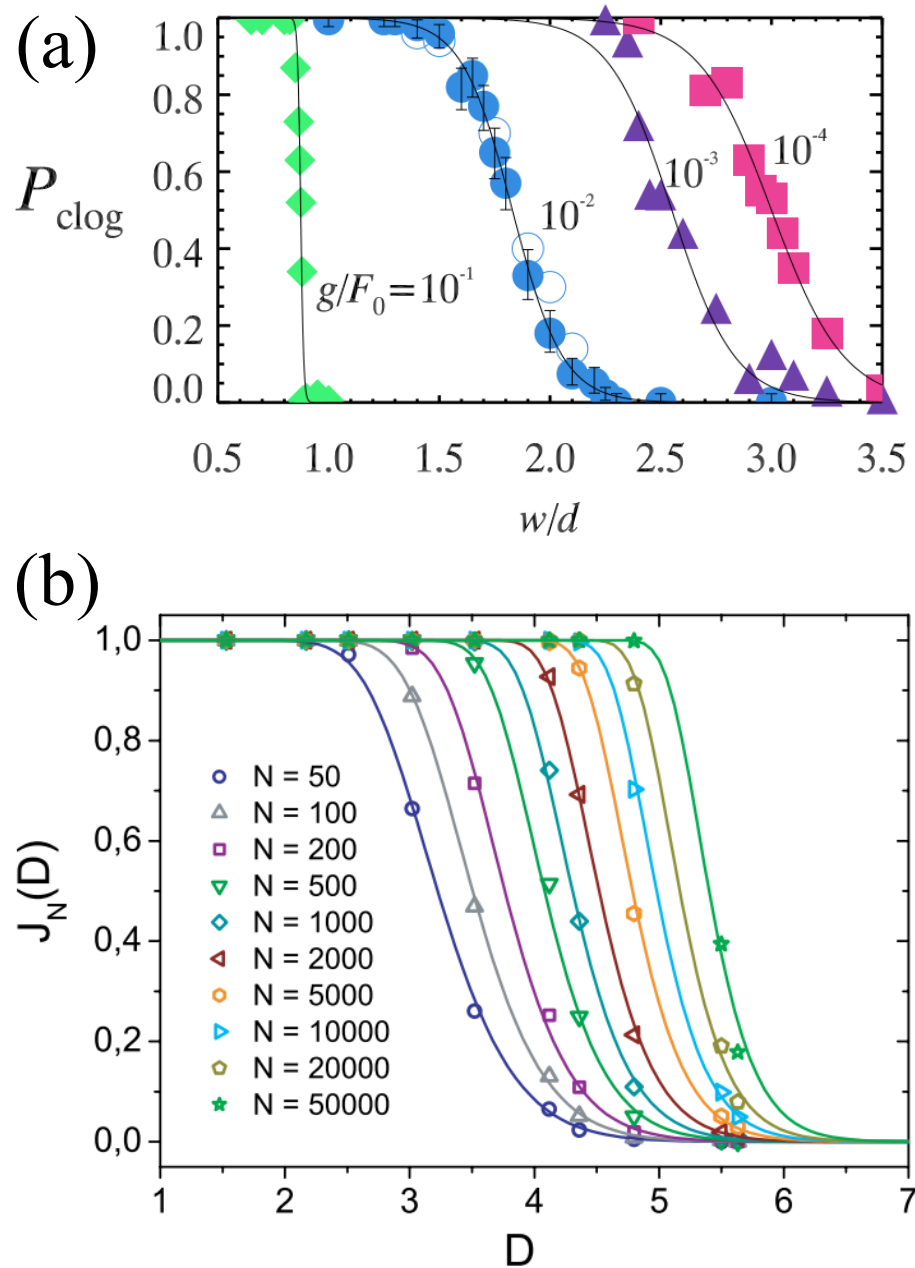


Figure 1.9: Fig.(a): Clogging probability(P) for systems of soft spheres, as a function of hopper opening of particle diameter(w/d) for various ratio of particle softness and gravitational strength. Republished with permission of American Physical Society, from "Clogging of soft particles in two-dimensional hoppers", Xia Hong, Meghan Kohne, Mia Morrell, Haoran Wang, and Eric R. Weeks, Phys. Rev. E **96**, 062605 (2017)[52]. Fig(b) Clogging probability $J_N(D)$ as a function of hopper opening to particle size ratio D , for hoppers loaded with N particles. Republished with permission of the EPL Editorial Office, from "Jamming and critical outlet size in the discharge of a two-dimensional silo"[47].

In Chapter 4 we study the interplay between these cohesive forces, which increase the clogging probability and gravity, the driving force that pushes the particles through the hopper. We investigate this relation by varying cohesive forces, gravitational forces and the size of the hopper exit, using simulations, as well as experimental data provided by our collaborators.

1.4 Dissertation Outline

The rest of this dissertation will be organized in four Chapters. In these chapters we explore how amorphous materials are affected by interparticle cohesive forces (Ch.2 and Ch.4), and how polydispersity affects the amorphous materials when an external load is applied (Ch.2 and Ch.3).

In Chapter 2 we use simulations to study the mechanical response of droplets rafts under compression, for mostly monodisperse crystal structures, as well as more polydisperse glassy materials. We characterize the response of these materials, by measuring the amount of plastic deformation events, and by measuring the force needed to trigger such events for different material properties like polydispersity, size, and aspect ratio. In Chapter 3 we carry out experiments to study the quasi 2D granular flow for highly polydisperse distributions of disks. We use a variety of differently sized disks to build multiple disk distributions with different size ratio and polydispersity. We then investigate the effect polydispersity has on the flow properties and plastic deformations of the system, using the different disk distributions. In Chapter 4 we study the amorphous flow of a quasi 2-d hopper, and how cohesive forces affect the outflow of particles. We characterize this outflow by studying the clogging probability as well as measuring the amount of particles remaining in a clog, while varying the gravitational and cohesive forces, as well as the hopper width.

Finally in Chapter 5 we review the conclusions of our projects, possible future

projects relating to the research presented, the impact this work will have.

Chapter 2

Compression and fracture of ordered and disordered droplet rafts

The work presented in this chapter has been published in “PHYSICAL REVIEW E” [21].

We simulate a two-dimensional array of droplets being compressed between two walls. The droplets are adhesive due to an attractive depletion force. As one wall moves toward the other, the droplet array is compressed and eventually induced to rearrange. The rearrangement occurs via a fracture, where depletion bonds are quickly broken between a subset of droplets. For monodisperse, hexagonally ordered droplet arrays, this fracture is preceded by a maximum force exerted on the walls, which drops rapidly after the fracture occurs. In small droplet arrays a fracture is a single well-defined event, but for larger droplet arrays, competing fractures can be observed. These are fractures nucleated nearly simultaneously in different locations. Finally, we also study the compression of bidisperse droplet arrays. The addition of a second droplet size further disrupts fracture events, showing differences between

ideal crystalline arrays, crystalline arrays with a small number of defects, and fully amorphous arrays. These results are in good agreement with previously published experiments.

2.1 Introduction

As previously mentioned in Chapter 1 of this dissertation, foams, emulsions, and colloids are often used as models for systems such as crystals and glasses [16, 57]. Foams are gas bubbles in a liquid, with the gas-liquid interfaces stabilized by surfactant molecules. Emulsions are similar in that they are droplets of one liquid in a second immiscible liquid, with surfactants stabilizing the liquid-liquid interfaces. Colloids are composed of solid particles in a liquid. The first published work using bubbles to model crystals was done by Bragg and Nye [58] and Bragg and Lomer [59]. These soft matter systems can be used to study fundamental questions about order to disorder transitions [20, 60–67], jamming [63, 67–71], and crystal nucleation and melting [12, 72–74]. More recently foams have also been used to study biological systems [75–78].

A key feature of these systems is their response to external stress. The mechanical response of these dispersions can be tuned by varying the composition [69, 79–82]. It is also well known that materials become harder to deform as the volume fraction of the particulate phase is increased (that is, the colloidal particles, droplets, or bubbles, depending on the material) [83, 84]. Once a volume fraction threshold is reached, the system responds like a soft solid [80, 83, 85, 86]. However, if enough force is applied, the system will plastically deform and flow. The relation between macroscopic flow and local plastic events has been the focus of much work [80, 82, 87–89].

One concern using soft materials as models for crystals is that in contrast to atoms which are all identical, the components of a soft material are typically somewhat poly-

disperse. Nonetheless, one can use low polydispersity (nominally “monodisperse”) soft materials to model crystals [19, 58]. Such model systems allow one to investigate the effect of local plastic deformations and disorder [20, 90], which are connected to the bulk properties of the crystal, such as yield stress [19, 20, 61, 63].

The mechanical properties of a glass, like crystals, is heavily dependent on its microscopic structure, and this has been studied in a variety of soft materials serving as model glasses [57, 60, 62, 64, 67, 74, 90–95]. Prior studies examined how the disordered structure of a glass affects a sample’s mechanical properties [61, 96–98]. It is of interest to contrast crystals and glasses; for example numerical studies have shown that adding even a small amount of defects into a crystal drastically changes the mechanical properties of the resulting system [57, 60, 62, 64, 67, 90, 93–95].

Experimental work by Ono-dit-Biot *et al.* examined the ability of quasi-two-dimensional crystalline and noncrystalline samples to fracture under compression [19, 20]. The experiments consisted of a monolayer of oil droplets suspended in an aqueous solution. The droplets packed into a raft held together by depletion forces. The raft was then horizontally compressed between two parallel walls, causing the droplets to rearrange. Nominally monodisperse rafts formed hexagonal close packed configurations. During the compression process, the hexagonal packing would undergo coordinated fracture events. Each such fracture allowed the crystal to reduce the number of rows by one, fitting into the narrower space imposed by the confining walls, while maintaining hexagonal order after the fracture event concluded. However, when smaller droplets, which act as defects, were substituted into the droplet array, the coordinated fracture events were replaced by a series of smaller intermittent fractures. With a sufficiently large number of defects, the samples behaved much more like a glass than like a disordered crystal.

The goal of this chapter is to computationally replicate and extend the experimental results of Ono-dit-Biot *et al.* [19, 20]. In particular, we expand on the prior

results by simulating a larger number of droplets with a greater variety of starting configurations, allowing us to understand system size effects that were untested in the experiments. Furthermore, we investigate the influence of experimental imperfections: namely, the role of imperfectly parallel compressing walls, and understanding the role of polydispersity of particle sizes. We also present analytic calculations which highlight the importance of attractive interactions between droplets to the observed results.

Our simulations include the three key forces present in the experimental work. The first of these is a repulsive force between the droplets (or the droplets and the walls), that is due to surface tension. Second, an attractive force due to depletion from micelles present in the experiments and modelled here with the Asakura-Oosawa model [99]. Third, a dissipative viscous force acting on moving droplets, although this is minimal given the small velocities considered. Our simulations reproduce the experimental observations, namely the fracture events and their dependence on the particle size distribution. We also investigate a new phenomenon where the crystal fractures in multiple locations nearly simultaneously, disrupting the packing post-fracture, which occurs more frequently in larger droplet arrays. Our work suggests that this phenomenon was likely suppressed in the experiments due to a slight tilt of the relative orientations of the two walls, taking them out of parallel by $\sim 0.2^\circ - 1.0^\circ$.

2.2 Computational methods

2.2.1 Simulation forces

Our goal is to have a simulation which captures the key features of the prior work of Ono-dit-biot *et al.* [19, 20]. We use the Durian “bubble model” [87] to simulate the droplets’ motions as the array is compressed. In particular, we use the modified version presented by Tewari *et al.* in Ref. [100] which allows droplets to have differ-

ent numbers of nearest neighbors; our code is specifically adapted from that used in Hong *et al.* [52, 101]. The athermal bubble model simulates the interactions between droplets in a viscous medium. The model replaces the details of each droplet’s deformation with a simple pairwise repulsive interaction. The model assumes negligible inertial effects (appropriate for low-mass bubbles or slow-moving emulsion droplets), and viscous interactions. For our work we add the effect of attractive depletion interactions between adjacent particles as well as between particles and the walls.

The first step in our simulation is to generate the droplets. For nominally monodisperse simulations, we assign droplet radii according to a normal distribution with mean $\langle R \rangle = 1$ and width $\delta = 1.25 \times 10^{-3}$. This value is small enough to represent a single droplet size, while still allowing for some randomness that is inherent in the experiment. For a bidisperse distribution, we generate droplets with radii $R_{\text{large}} = 1$ and $R_{\text{small}} = 0.765$, the same radius ratio as in the experimental work [20]. In all cases, the droplets are initially arranged in a hexagonal closed packed lattice, with p rows and q columns. Rows are defined as a set of q droplets aligned parallel to the walls. An example is shown in Fig. 2.1 with $p = 4$ rows by $q = 5$ columns.

Each droplet is modeled as a sphere, and the simulation starts by calculating all forces acting on each droplet. The first is an elastic repulsive force between droplets. If droplets i and j overlap, the repulsive force is:

$$\vec{F}_{ij}^{\text{contact}} = f_0 \left[\frac{1}{|\vec{r}_i - \vec{r}_j|} - \frac{1}{|R_i + R_j|} \right] \vec{r}_{ij}, \quad (2.1)$$

where R_i is the droplet radius, their positions are \vec{r}_i , and the difference vector is $\vec{r}_{ij} = \vec{r}_i - \vec{r}_j$. An overlap occurs when a neighbor j is close enough to the droplet i such that $|\vec{r}_{ij}| < R_i + R_j$. Here, f_0 acts as a spring constant, the origin of which is the surface tension induced Laplace pressure. In particular, Eqn. 2.1 avoids the need to simulate the actual deformation of the droplets by replacing the deformation with

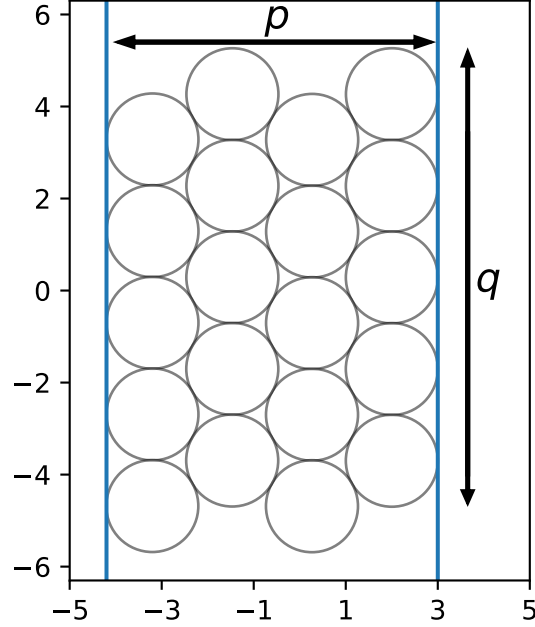


Figure 2.1: Snapshots for a twenty droplet simulation. In this simulation the droplet is arranged in a $p = 4$ by $q = 5$ configuration.

this effective force which is valid at low deformations, the regime of interest. This linear (Hookean) response was observed in the experiments [19].

The second interaction force between neighboring droplets is a viscous force, if the two droplets are moving at different velocities:

$$\vec{F}_{ij}^{\text{viscous}} = b(\vec{v}_i - \vec{v}_j) \quad (2.2)$$

with b being the viscous coefficient, and \vec{v}_i the velocity of a given particle. This force acts on each droplet in a direction that tries to bring their velocities into agreement: for example, if droplet i is motionless then the viscous force from droplet j acting on i is in the direction of v_j . Additionally droplets are affected by the viscous drag of the surrounding medium, and is calculated as:

$$\vec{F}_i^{\text{drag}} = -b\vec{v}_i \quad (2.3)$$

where $b = 1$ as in Eqn 2.2. This force acts in opposition to the displacement of i bubble.

A final important force in the experiment is the depletion force: an attractive force acting between droplets that are sufficiently close. In the experiment, this is due to small surfactant micelles. In the simulation this is modeled as an effective force between neighboring droplets, which in this case are droplets with distance $r_{ij} < R_i + R_j + 2a_s$. Here a_s is the radius of the depletant which thus sets the range of the attractive interaction. The depletion forces are calculated using the Asakura-Oosawa model [99]. In Figs. 2.2 we show a sketch of how depletion force acts, Fig. 2.2.(a), as well as the excluded and overlapping volumes, Fig. 2.2(b).

The first step needed to calculate the depletion interactions is to calculate the overlapping volume between a pair of spheres with a radius $R'_i \equiv R_i + a_s$ [102]:

$$V_{\text{overlap}}(r_{ij}, R'_i, R'_j) = \frac{\pi}{12r_{ij}} (R'_i + R'_j - r_{ij})^2 \times \left(r_{ij}^2 + 2r_{ij} (R'_i + R'_j) - 3(R_i'^2 + R_j'^2) + 6R'_i R'_j \right). \quad (2.4)$$

Using the overlap volume we can obtain the associated Helmholtz free energy, which we then differentiate to get the depletion force:

$$\vec{F}_{ij}^{\text{dep}} = \frac{\phi_c}{8a_s^3} \frac{\partial V_{\text{overlap}}(r_{ij}, R'_i, R'_j)}{\partial r_{ij}} \hat{r}_{ij}, \quad (2.5)$$

where the direction of the force is attractive between the two particles. In this formula, ϕ_c is a constant related to the temperature and volume fraction of the depletant. In the simulation we set $a_s = \frac{\langle R \rangle}{20} = 1/20$. The formula for $\partial V_{\text{overlap}}/\partial r_{ij}$ is:

$$\frac{\partial V_{\text{overlap}}(r_{ij}, R'_i, R'_j)}{\partial r_{ij}} = \frac{\pi}{4} \left[r_{ij}^2 - 2(R_i'^2 + R_j'^2) + \left(\frac{R_i'^2 - R_j'^2}{r_{ij}} \right)^2 \right]. \quad (2.6)$$

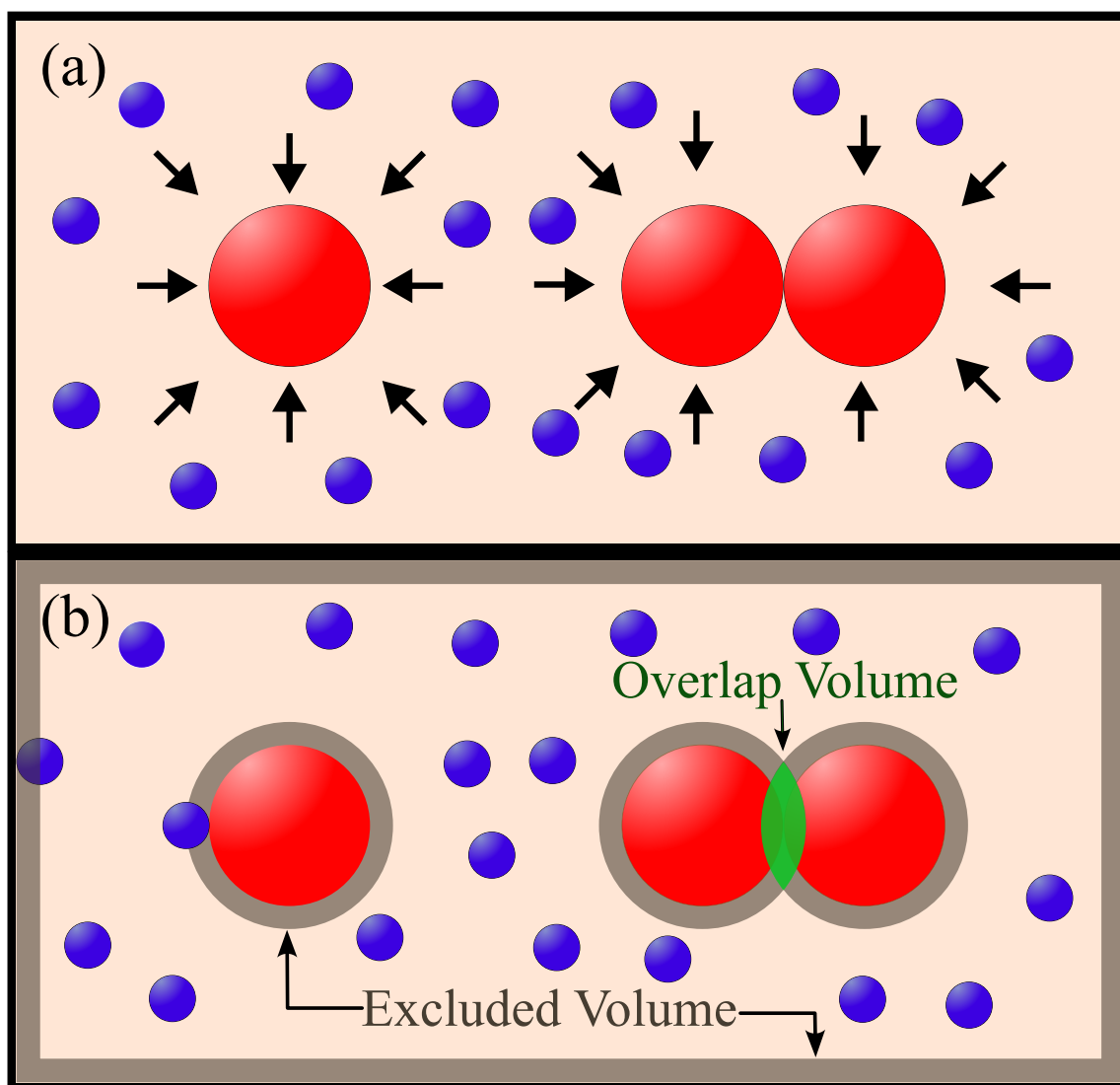


Figure 2.2: Illustrations of how the depletants act when in high enough concentration. In (a) we see how the resulting pressure of depletants pushed together droplets which surfaces are within one depletant diameter away from each other. In (b) we show the excluded volumes in which depletants don't fit in. Overlapping volumes occur when two excluded volumes overlap, this results in a net gain of available volume for the depletants, which increases the net entropy of the system, lowering the Helmholtz free energy, resulting in an attractive force between the droplets.

In addition to calculating the droplet-droplet interactions, we also need to calculate the droplet-wall interactions for droplets sufficiently close to the wall. The repulsive force from the wall is given by

$$\vec{F}_i^{\text{wall,repel}} = f_0 \langle R \rangle (r_{\text{wall},i}^{-1} - R_i^{-1}) \hat{n}_{\text{wall}}, \quad (2.7)$$

where $r_{\text{wall},i}$ is the distance from the droplet center to the wall. Note this force diverges as $r_{\text{wall}} \rightarrow 0$, preventing any droplets from passing through the wall. In particular this form differs from Eqn. 2.1 by using the unit normal vector \hat{n}_{wall} rather than \vec{r}_{wall} , which is what leads to the divergence. The magnitude of the attractive depletion force between a droplet and the wall is given by:

$$F_i^{\text{wall,dep}} = \frac{\pi \phi_c}{8a_s^3} (R_i + 2a_s - r_{\text{wall},i})(R_i + r_{\text{wall}}) \quad (2.8)$$

for every droplet with $r_{\text{wall},i} < R_i + 2a_s$. We will summarize these two terms into:

$$F_i^{\text{wall}} = F_i^{\text{wall,repel}} + F_i^{\text{wall,dep}},$$

noting that the two components point in opposite directions (and thus F_i^{wall} can be zero if these two components are in balance).

The Durian Bubble Model is originally for massless bubbles [87], and in our situation we treat droplets in a low Reynolds number limit for which inertial effects are negligible. Accordingly, the net force is always zero; the velocity of each particle is always such that the velocity-dependent viscous forces balance the other forces. Thus, we combine Eqns. 2.1, 2.2, and 2.5 and solve for the velocity:

$$\vec{v}_i = \frac{1}{N_i + 1} \langle \vec{v}_j \rangle + \frac{1}{b(N_i + 1)} \left[\sum_j \left(F_{ij}^{\text{contact}} - F_{ij}^{\text{dep}} \right) \hat{r}_{ij} + F_i^{\text{wall}} \hat{n}_{\text{wall}} \right], \quad (2.9)$$

where N_i are the total number of neighbors for particle i . We use fourth order Runge-Kutta to solve this differential equation for the velocities at each time step.

2.2.2 Model parameters

The model sketched above has many parameters. In this section we discuss how these parameters are set based on comparison with the prior experimental work (Refs. [19, 20]) and on computational convenience. We start by fixing our simulation parameters as $b = 1$, $\langle R \rangle = 1$, $v_{\text{wall}} = 10^{-4}$, $\phi_c = 10^{-4}$, $f_0 = 10$, and $a_s = 0.05$. Using several nondimensional ratios we can make various comparisons to the experiment.

First, the range of the depletion force is given by the ratio of the size of the micelles and the size of the droplets. In the experiments the mean droplet radius $\langle R \rangle^{\text{exp}} \approx 20 \mu\text{m}$, and depletion micelles which have size $a_s^{\text{exp}} \approx 5 \text{ nm}$, the experimental range is $\alpha_1^{\text{exp}} \approx 2.5 \times 10^{-4}$. In the simulations the range of the depletion interaction is set to:

$$\alpha_1^{\text{sim}} = \frac{a_s}{\langle R \rangle} = 0.05. \quad (2.10)$$

Here α_1^{sim} is larger than α_1^{exp} , although still much less than 1. This choice avoids numerical instabilities which would occur if the depletion force was too short range.

Second, we need to understand the relative importance of the depletion and viscous forces. In the experiment, this ratio of forces is

$$\alpha_2^{\text{exp}} = \frac{v_{\text{wall}}\eta}{W} \approx 10^{-5},$$

where the viscosity $\eta \approx 1 \times 10^{-3} \text{ Pa}\cdot\text{s}$, the depletion energy per unit area between two droplets $W \approx 1 \times 10^{-6} \text{ J/m}^2$, and the speed of the wall $v_{\text{wall}} \approx 3 \times 10^{-7} \text{ m/s}$ [19].

In the simulation, the same ratio is

$$\alpha_2^{\text{sim}} = \frac{bv_{\text{wall}}a_s}{\phi_c} = 0.05. \quad (2.11)$$

In both the simulation and in the original experiments, the depletion force is stronger. That being said, in the simulations, the effect of viscosity is more significant than in the experiment. This choice is to keep the simulation computational time reasonable; reducing the viscosity coefficient b would require a smaller integration time step.

Finally we compare the forces of repulsion and depletion in the experiment:

$$\alpha_3^{\text{exp}} = \frac{k}{W} \sim 10^4,$$

where $k \approx 10^{-3}\text{N/m}$ is the spring constant associated with the oil droplets' surface tension [84, 103]. In our simulations we have:

$$\alpha_3^{\text{sim}} = \frac{f_0 a_s}{\phi_c} = 0.5 \times 10^4.$$

These are the same order of magnitude; the factor of 0.5 difference means that the simulated droplets are slightly softer than the experimental droplets. Adjusting the ratio in the simulation would again increase the computational costs, so we judge our parameter choices to be a reasonable compromise between computational costs and adequately capturing the experimental limits (short range attractive forces, small viscous forces compared to depletion, large repulsive forces compared to depletion).

2.2.3 Simulation timescales

We need to choose the simulation time step carefully to allow for the correct integration of all interactions. As shown in Eqns. 2.1, 2.2, and 2.5, the magnitude of the different forces are set by the constants f_0 , ϕ_c , and b for repulsive, depletion, and viscous forces respectively. From these constants, together with the speed of the walls, v_{wall} , average droplet radii, $\langle R \rangle$ and the depletant radius, a_s , we can define three different time scales: $\tau_1 = \frac{\langle R \rangle b}{f_0} = 10^{-1}$, $\tau_2 = b a_s^2 / \phi_c = 25$, and $\tau_3 = \langle R \rangle / v_{\text{wall}} = 10^4$. τ_1 is the time scale for two overlapping droplets to push apart in the absence of the

depletion force, and is the fastest time scale. τ_2 is the time scale for two overlapping droplets to pull together due to the depletion force, which is slower than τ_1 because as noted above, the depletion force is weaker than the repulsive force. Finally, τ_3 is the time scale for the walls to move a distance $\langle R \rangle$. Given these results, we set the simulation time step to be $\Delta t = \tau_1 = 0.1$. We have checked that simulations run with smaller time steps give the same results as those run with $\Delta t = 0.1$. The implication of $\tau_1 \ll \tau_3$ is that during rearrangements, the walls will move a negligible distance.

2.2.4 Simulation goals

Given that the simulation parameters are chosen to match the experiment to a reasonable extent, it is worth stating what we wish to replicate. The experiment measures forces exerted on the moving walls, and relate these forces to the effective spring constant of two interacting droplets due to the depletion force [19]. Our wall forces likewise must relate to the effective spring constant in our simulation, so we consider this in Secs. 2.3 and 2.4. This is not a replication *per se* so much as allowing us to illuminate the importance of both compressive and tensile forces acting between droplets. That being said, one important experimental observation to replicate is the relationship between the wall forces, array size, and effective spring constant acting between a pair of droplets, which will be examined in Sec. 2.4-A.

One experimental observation to replicate is how the forces on the walls are changed when the droplet array has a mixture of particle sizes. When the experimental droplet array consisted of a nearly 50/50 mixture of large and small droplets, the array rearranged in a nearly continuous sequence of small fracture events; however, this observation was limited to a 23-droplet array [20]. We wish to replicate the observations and extend them to larger array sizes.

Finally, moving beyond replication, we will examine how the fractures depend on the system size, droplet polydispersity, and wall tilt angles: factors that are easier to

vary smoothly in the simulation as compared to experiment.

2.3 Analytical results

We wish to understand the force required to compress the droplet array. We start by considering the effective spring constant between two droplets. We then consider compressing three droplets. Due to the attractive depletion force, compressing three droplets requires one effective spring to be stretched while the other two are compressed. In this section we take $R_i = R_j = R = 1$.

2.3.1 Effective spring constant: two droplets

For two droplets in contact the balance of repulsive and attractive forces in equilibrium lead to a harmonic interaction with an effective spring constant. Balancing Eqns. 2.1 and 2.5, the equilibrium distance between two particles can be approximated as:

$$d_{\text{eq}} = 2R - 2a_s \left(\frac{L^2}{2R^2} - 1 \right)^{-1}. \quad (2.12)$$

using:

$$L^2 = \frac{8f_0a^3}{\pi\phi_c} \quad (2.13)$$

We can use two of the nondimensional ratios analyzed in Sec. 2.2.2, the range of the depletion forces α_1 and the ratio of repulsion to depletion forces α_3 , to write

$$\frac{L^2}{R^2} = \frac{8}{\pi}\alpha_1^2\alpha_3 = \frac{100}{\pi} = 31.8. \quad (2.14)$$

By substitution of Eqn. 2.14 into Eqn. 2.12, we see that the term multiplying a_s has a small value for our simulations so we will define:

$$\epsilon = \left(\frac{L^2}{2R^2} - 1 \right)^{-1} \approx 0.0671. \quad (2.15)$$

We can then finally write the equilibrium position as:

$$d_{\text{eq}} = 2(R - a_s \epsilon) \approx 2(1 - 0.00336) \approx 1.993. \quad (2.16)$$

As expected the equilibrium position would be at $2R$ if depletion wasn't present. With depletion, the equilibrium position is adjusted by a small fraction of the depletant radius a_s . With the parameters used in the simulations the particles overlap but just slightly. (In the experiment, this implies that the droplets would be slightly deformed due to the depletion force. Given that $\alpha_3^{\text{exp}} \sim 10^4$, the experimental deformation is likely unobservable.)

At this point we can calculate the effective spring constant response for monodisperse droplet-droplet interactions due the balance of depletion and repulsion. Using both Eqn. 2.1 and 2.5, and doing a small displacement from equilibrium Δr_{ij} , results in the force increasing by:

$$\Delta F = \left(\frac{f_0}{2R} - \frac{R\pi\phi_c}{8a_s^3} \right) \Delta r_{ij} = k_1 \Delta r_{ij}, \quad (2.17)$$

which leads to

$$k_1 \approx 4.69 \quad (2.18)$$

as the effective spring constant for droplet-droplet interactions. The depletion force slightly reduces the spring constant from that due purely to repulsion, which is $f_0/(2R) = 5$.

We can similarly calculate the energy associated with breaking a depletion bond.

In this case we must calculate the work needed to separate two droplets from their equilibrium separation, d_{eq} , up to the point where depletion turns off, $d_{\text{off}} = R_i + R_j + 2a_s$.

$$E_{\text{depletion}} = -\frac{\phi_c}{8a_s^3} \int_{d_{\text{eq}}}^{d_{\text{off}}} \frac{\partial V_{\text{overlap}}}{\partial r_{ij}} dr_{ij} = \frac{\phi_c}{8a_s^3} V_{\text{overlap}} \Big|_{d_{\text{off}}}^{d_{\text{eq}}}$$

The minus sign is due to the fact that the motion to separate the droplets opposes the depletion force. Since there is no overlapping volume at $d_{\text{off}} = R_i + R_j + 2a_s$, we have only the equilibrium volume:

$$E_{\text{depletion}} = \frac{\phi_c}{8a_s^3} V_{\text{overlap}}(d_{\text{eq}}). \quad (2.19)$$

However since the equilibrium distance is less than the radius of the droplets, we must also take into account the repulsive force's work, which assists in separating the droplets:

$$W_{\text{rep}} = f_0 \int_{d_{\text{eq}}}^{R_i+R_j} \left(1 - \frac{r_{ij}}{R_i + R_j}\right) dr_{ij}, \quad (2.20)$$

and so the corrected term for the energy needed to break a bond between two droplets is the difference between Eqns. 2.19 and 2.20:

$$E_1 = \frac{\phi_c}{8a_s^3} V_{\text{overlap}}(d_{\text{eq}}) - \frac{f_0(R_i + R_j - d_{\text{eq}})^2}{2(R_i + R_j)}. \quad (2.21)$$

Using Eqns. 2.12 and 2.14, we can simplify this further to:

$$E_1 = \frac{\phi_c}{8a_s^3} V_{\text{overlap}}(d_{\text{eq}}) - \frac{2f_0 a_s^2 \epsilon^2}{R}. \quad (2.22)$$

We can now replace all the values by the corresponding constants, and for d_{eq} and L^2 from Eqns. 2.12 and 2.14, respectively, which gives us the energy stored per bond in

the monodisperse case:

$$E_1 = 0.00173. \quad (2.23)$$

We can repeat a similar calculation for the effective spring constants and bond energy present at the walls, and obtain:

$$k_{\text{eff}}^{\text{wall}} = 9.57 = 2.04k_1, \quad (2.24)$$

and

$$E_1^{\text{wall}} = 0.00340 = 1.965E_1. \quad (2.25)$$

2.3.2 Equivalent spring model for three droplets

We next consider the compression of three monodisperse droplets in an equilateral triangle arrangement, shown schematically in Fig. 2.3(a). In this case we start with two rows of droplets and the compression causes a rearrangement to one row. As the top wall moves towards the bottom wall, the droplet cluster attaches to the two walls due to depletion forces. Initially the bonds to the walls are all under tension due to the depletion force, pulling on the two walls. As the distance between the walls continues to decrease, the droplets go through equilibrium (panel b) with the spacing between each pair of droplets being d_{eq} (Eqn. 2.12). As the compression proceeds, the force continues to rise as the distance between the walls decreases (panel c). During this process, the diagonal bonds compress while the horizontal bond between the two droplets on the bottom wall is under tension. Eventually this horizontal bond breaks, which allows the diagonal compressed bonds to relax (panel d); from this point onward the droplets will continue to move with only the viscosity resisting their motion until they are reduced to a single row of droplets (not shown). In Fig. 2.3(e) we plot the force on the walls as a function of the distance. Time is advancing from right to left. The linear rise of the force from position (a) to (c) indicates that the

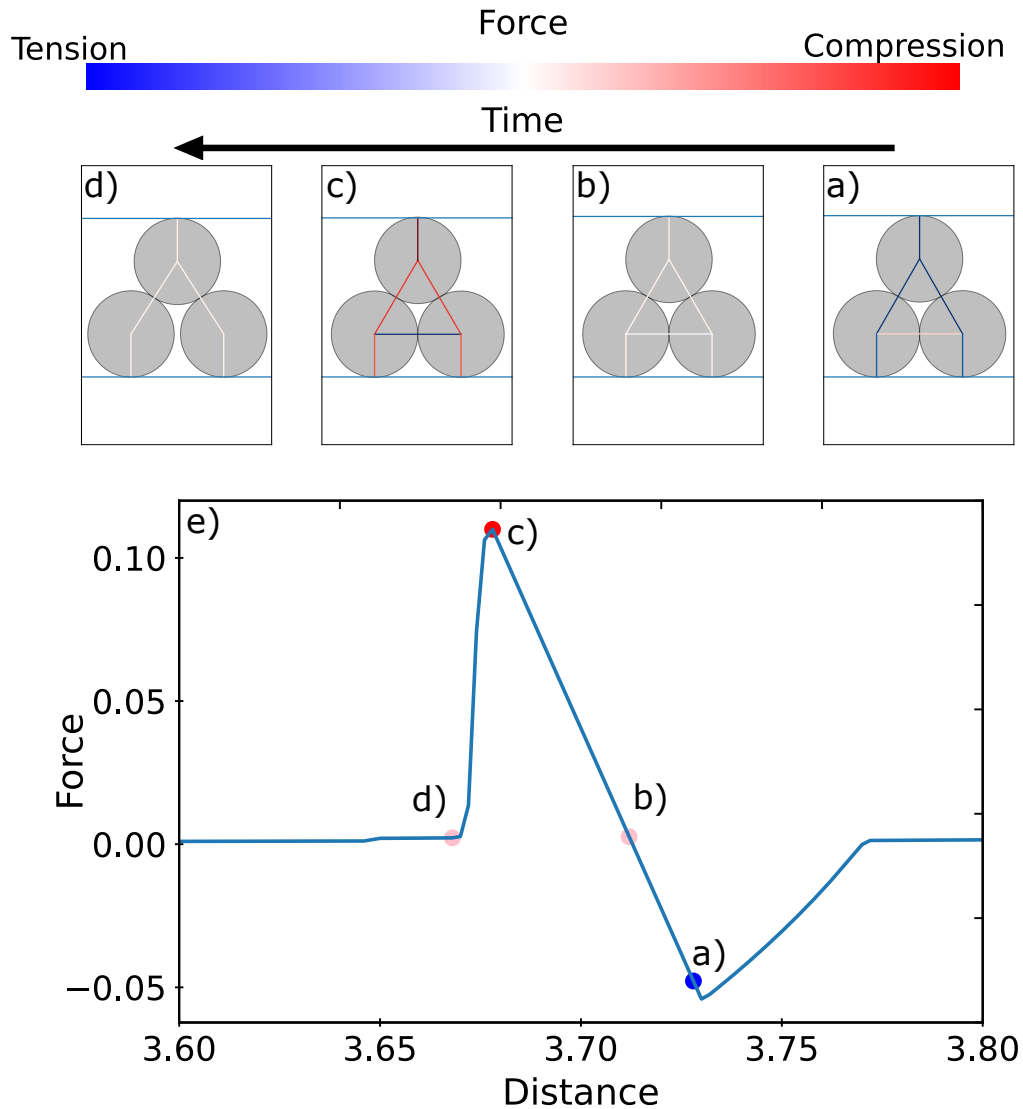


Figure 2.3: (a-d): Consecutive snapshots of the row reduction for three droplets: note that time increases from right to left, to match panel (e). Blue bonds are under tension, whereas red indicates compression. In panel (a), as the walls move together, the three droplets attach to the walls due to depletion and thus exert tension on the walls, resulting in the negative force peak seen in panel (e) at distance $(2 + \sqrt{3})R \approx 3.73$. As the top wall continues to move closer to the bottom wall, the droplets go through equilibrium [panel (b)], and eventually the walls begin compressing the droplets [panel (c)], leading to rise in the force on the walls. At the peak of the force, the horizontal bond between the two left particles is under tension. When this bond between the two bottom droplets breaks, the force rapidly drops [panel (d)].

the array is compressed elastically, until the vertical bond breaks at (c) and the row reduction occurs.

To explain the elastic rise in force [position (a) to (c) in Fig. 2.3(e)], we note that each droplet bond has spring constant k_1 , which can be used to calculate the equivalent spring constant for the triangular array. For these three droplets, the compression force between the two left droplets and the left wall is half that of the compression force of the single droplet on the right and the adjacent wall. To find a relationship between the force F exerted by the walls on the droplet pack and the horizontal displacement of the walls from the equilibrium position (when $F = 0$), we start by considering the situation sketched in Fig. 2.4(a): the left two droplets only move in the y direction, with the top droplet moving up by Δy and the bottom moving down by Δy ; and the right droplet moves left by Δx under the action of the force F . (To be clear, this is in the reference frame where the left droplets do not move horizontally. In practice, all three droplets move horizontally under the influence of the walls, with the net horizontal displacement between the right droplet and the left droplets as Δx .)

A free body diagram for the top droplet is shown in Fig. 2.4(b). For the moment we will consider the vertical bond between the two left droplets to have spring constant k_2 in order to illustrate the role of tension, but since the spring constant is the same (for small displacements) whether under tension or compression, we will eventually set $k_2 = k_1$. The distance between the top droplet and right droplet is initially d_{eq} . When the droplets begin to move, the change in this distance is

$$\Delta r \approx \Delta x \cos \theta - \Delta y \sin \theta. \quad (2.26)$$

This expression is valid in the limit where $\Delta x, \Delta y \ll r_{eq}$, and changes to the angle θ due to droplet movement can be ignored as they are a second order correction. This

formula for Δr has been chosen with signs so that $\Delta r > 0$ when the droplets are being compressed, consistent with the direction of the force indicated in Fig. 2.4(b). Balancing the two forces in the vertical direction gives

$$\Delta y = \frac{k_1 \sin \theta \cos \theta}{k_1 \sin^2 \theta + 2k_2} \Delta x, \quad (2.27)$$

which relates the horizontal and vertical displacements.

If we take the extreme case where $k_2 \rightarrow \infty$, Eqn. 2.27 gives us $\Delta y \rightarrow 0$, as no matter how much we push, the two vertical droplets are stuck together at a fixed separation. On the other hand if there is no adhesion force, then $k_2 = 0$ and $\Delta y = \cot \theta \Delta x$, which corresponds to the droplets displacing as needed to accommodate the right droplet moving leftwards (and thus keeping $\Delta r = 0$). Finally for the case we consider in the simulations, $k_1 = k_2$ and $\theta = 30^\circ$, giving:

$$\Delta y = \frac{\sqrt{3}}{9} \Delta x \equiv C \Delta x. \quad (2.28)$$

This is indeed the relation between the displacements that we observe in the three droplet simulation.

Substitution of Eqn. 2.28 into Eqn. 2.26 for Δr , and balancing the horizontal forces in Fig. 2.4(b), leads to

$$F = 2k_1 \cos \theta (\cos \theta - C \sin \theta) \Delta x. \quad (2.29)$$

This expression relates the wall force F to the compression Δx of the three droplets; the term in front of Δx is an effective spring constant equal to $(4/3)k_1$. Note that the term with C , which allows for the vertical motion of the two left side droplets, reduces the effective spring constant slightly (as the ratio of the second term to the first is $C \tan \theta = 1/9$). Again to understand the role of the tension force between

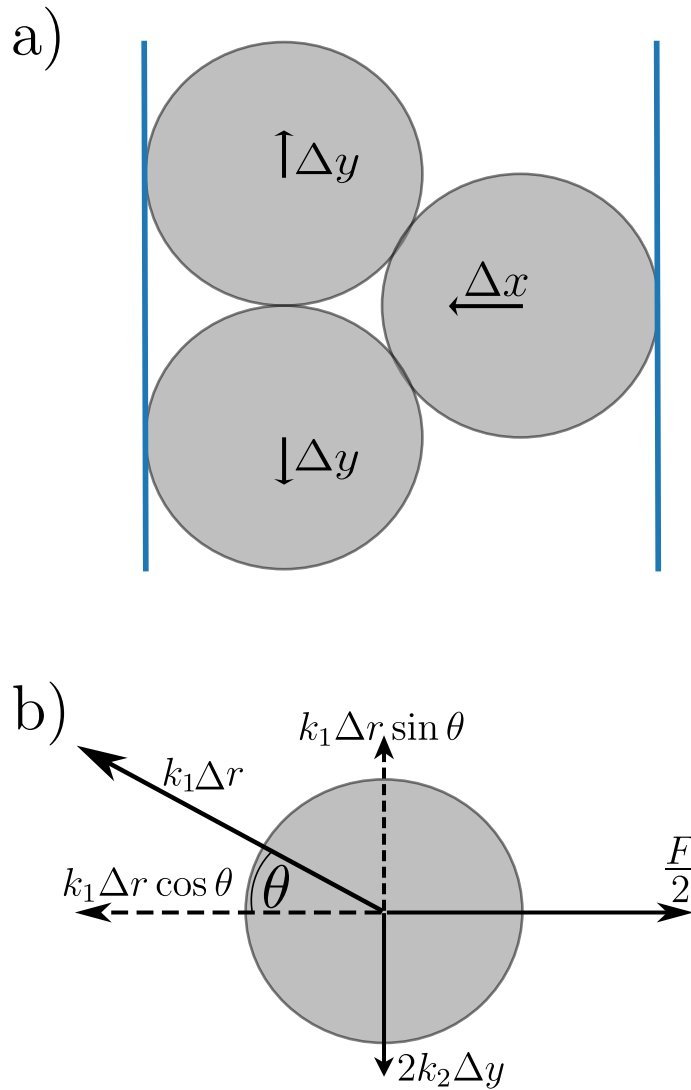


Figure 2.4: (a) Sketch of small displacements of three droplets. (b) Free body diagram of forces acting on the top left droplet. $F/2$ is from the wall, with the other $F/2$ contribution acting on the bottom droplet. The vertical spring is stretched by $2\Delta y$, so accordingly the force indicated as $2k_2\Delta y$ is a tension force from the bottom droplet. The $k_1\Delta r$ force is a compression force from the right side droplet. As the droplets are monodisperse $\theta = 30^\circ$. Changes in θ for small Δx and Δy can be ignored to first order.

the two vertically oriented droplets, we consider the limits for C . If $k_2 \rightarrow \infty$ then $C = 0$ and the effective spring constant is equal to $(3/2)k_1$. Intriguingly, this is the result one gets for two springs in parallel, in series with one spring, which apart from the diagonal connections is what we see in Fig. 2.4(a). In contrast, if $k_2 = 0$, then $C = \cot \theta$ and the term in parentheses would be zero, thus resulting in $F = 0$. Thus the tension bond plays an important role in generating the wall force.

In addition to the spring-like interaction of the three compressed droplets, there are also spring-like interactions with the walls. At the left side wall, because there are two droplets, the effective wall interaction behaves with spring constant of $2k_{\text{wall}}$; on the right side we have simply k_{wall} . These three springs act in series, so thus the overall effective spring constant the system has is

$$\frac{1}{k_{\text{eq}}} = \frac{1}{2k_{\text{wall}}} + \frac{1}{k_{\text{wall}}} + \frac{1}{2k_1(\cos^2 \theta - C \sin \theta \cos \theta)} \quad (2.30)$$

which simplifies to $0.673k_1 = 3.16$ using Eqns. 2.18 and 2.24. This is the value we measure from the slope of the elastic regime in Fig. 2.3(e), matching to the three significant figures we have been using. The close agreement is perhaps a bit surprising, given that the analytic calculation has been assuming small displacements whereas the simulation uses the full form of the depletion interaction. The agreement also confirms that our wall speed is slow enough that viscous forces are not adding significantly to our measured wall force.

We can also relate the energy required to break one depletion bond (Eqn. 2.22) to the force peak F_p . Ignoring energy stored in compressive interactions, the elastic energy $k_{\text{eq}}\Delta x^2/2$ gets converted into breaking Δn bonds, so we have

$$E_1 \Delta n = \frac{1}{2} k_{\text{eq}} \Delta x^2 = \frac{F_{\text{max}}^2}{2k_{\text{eq}}}. \quad (2.31)$$

From the data in Fig. 2.3, we have $\Delta n = 1$, $k_{\text{eq}} = 3.16$, and $F_{\text{max}} = 0.110$ leading to

$E_1 = 0.00191$ which is 10% larger than the prediction of Eqn. 2.22. The discrepancy is precisely because of the extra energy stored in the compressed droplets. The extra energy gets converted into droplet motion once the bonds under tension are broken.

2.4 Computational results for large droplet arrays

2.4.1 Equivalent spring model for nominally monodisperse crystals

We will next consider the general case of a nominally monodisperse rectangular array of droplets with p rows and q columns. We will consider the specific example of a 7×7 array but also, where relevant, discuss results from simulations with other numbers of droplets. Figure 2.5 shows this 7×7 droplet array undergoing a row reduction from $p = 7$ to $p = 6$ rows. A video of the compression process for this particular simulation is available in the Supplemental Materials Movie S1 of the paper this Chapter is based on[21]. All simulations are initialized by placing the droplets in a perfectly ordered array; one such initial state is shown in Fig. 2.5(a), which corresponds to the system before a fracture. The red lines indicate compression forces and the blue lines indicate tension forces. The tension is caused by the depletion forces between droplets along the vertical direction (parallel to the walls), therefore separating the droplets apart, pulling against the depletion force which holds the crystal together. In Fig. 2.5(b) the global fracture has broken the crystals into four distinct pieces. The forces decrease in magnitude, indicated by the light pink and light blue lines, showing the compression and tension in the crystal has been relieved during the fracture. Each piece moves as an essentially solid assembly; the relative position of the droplets within this assembly does not matter, and droplets at the boundaries move similarly to those in the middle. Finally in Fig. 2.5(c) a new crystal with $p = 6$ rows forms, with tension pulling the droplets back into a hexagonal configuration.

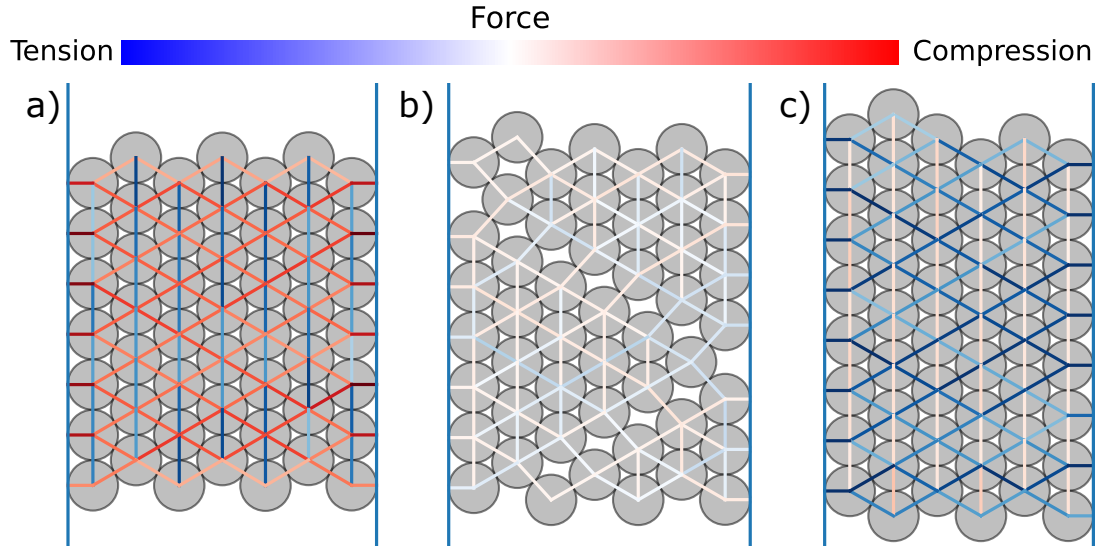


Figure 2.5: A 7×7 droplet array in its initial configuration undergoing a row reduction. In (a) we can see that the array is being compressed between the walls, as evidenced by the red compression bonds. The blue tension bonds run parallel to the walls, with the depletion force preventing the crystal from spreading along the direction of the walls. In (b) a global fracture has occurred, splitting the crystal into four separate pieces and relaxing the forces; many droplets are close to their equilibrium separation distance. In (c) the crystal settles into a 6×8 hexagonal-close-packed configuration and the depletion forces pull the droplets and walls closer together. The extra droplet is in the second column. Movie S1 in the Supplemental Material of the paper this chapter is based on [21], depicts the compression process for the array shown in this figure.

In this case the walls experience a tension force from the attractive depletion bonds which are not yet at their equilibrium position.

Clearly during the compression process the force exerted by the droplet packing on the walls varies in both magnitude and direction. In Fig. 2.6 we plot the force exerted on the left wall as the crystal is compressed and undergoes row reduction. Note that time increases from right to left, as the horizontal axis is the distance between the walls which decreases with time. We wish to understand the features of this graph, and will start with the easiest: during the compression force minima ($F < 0$) occur. These correspond to the droplets nestling into a new hexagonal arrangement, being pulled in together by depletion forces, and pulling on the wall as the droplets settle into this more compact arrangement. An example of this corresponds to Fig. 2.5(c)

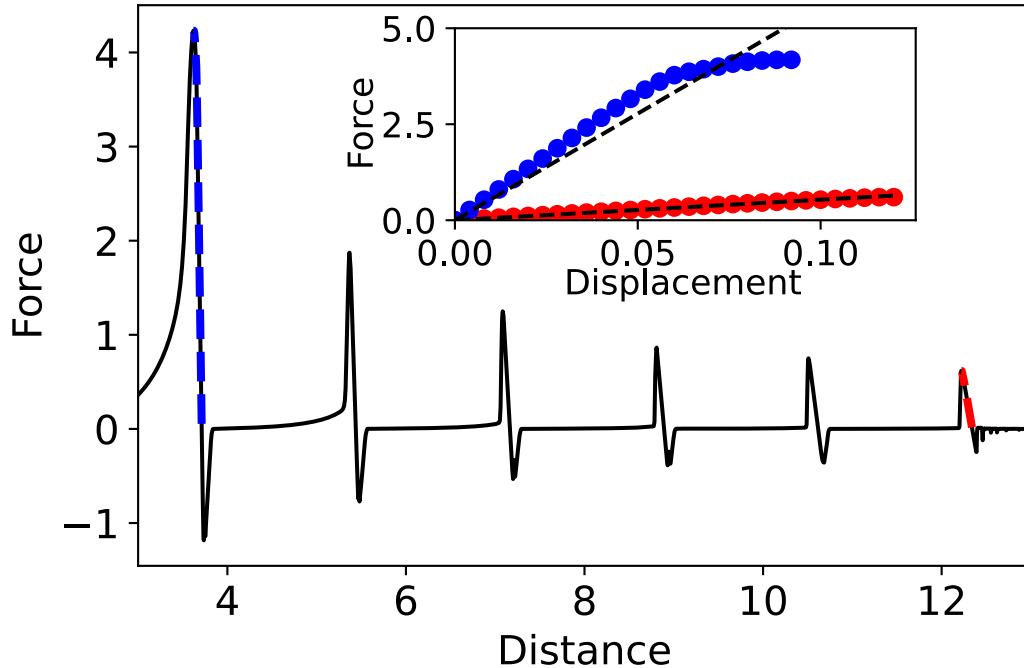


Figure 2.6: Force on the left wall as a function of the distance between the walls for a 7×7 monodisperse droplet array. The distance starts large and decreases, so time increases from right to left. Each successive peak is taller than the last, due to the increased amount of bonds that need to be broken. The blue and red slope are used to obtain k_{eq} , as in seen in the inset.

where all the bonds perpendicular to the wall are under tension: the more compact configuration exerts this tension on the walls due to the attractive depletion force.

We next turn to the question discussed previously for two and three droplets: what is the effective spring constant of this droplet array? The inset in Fig. 2.6 shows the increase of the force from zero as a function of the compression from the equilibrium position for the first row reduction (red) and the last (blue). The dashed lines in the inset show the linear fit used to obtain the k_{eq} for that row transition. We can see that once the walls begin compressing the crystal the force rises monotonically, with the crystal responding elastically until finally a catastrophic fracture event occurs. This is due to the tension forces being sufficient to break the depletion bonds between the droplets along the fracture. At large compression (blue data points) the force is less than expected, as when the array is down to two layers, being compressed into one

layer, the bonds at the ends of the array break first and relieve some of the wall force while the bonds in the middle are still intact. That is, the fracture does not occur everywhere simultaneously.

The effective spring constant is larger when the droplet array has fewer rows and more columns. This can be understood by a generalization of the spring model to bigger arrays. We have a rectangular array of p rows (parallel to the walls) and q columns; the equivalent spring constant is therefore that of a matrix of p springs in series and q springs in parallel. The interactions with the two walls, with spring constant $k_{\text{wall}} \approx 2k_1$, has the effect of adding an additional row. This leads to the following equation that relates the equivalent spring constant k_{eq} to the spring constant of a single droplet k_1 :

$$k_{\text{eq}} = \frac{q}{p+1}k_1 \quad (2.32)$$

In general Eqn. 2.32 is a simplification as it ignores the effect of the springs under tension, as described for three droplets in Sec. 2.3.2. Nonetheless this is a useful approximation. For the red slope in Fig. 2.6 we get $k_1 = 5.27$, and for the blue slope we get $k_1 = 7.65$. The higher k_1 for the blue data is because at this point the droplet array is quite wide and to compress the array requires nontrivial motions at the edges of the array as will be discussed below. These large edge motions lead to viscous forces which increase k_{eq} and thus the measured k_1 . These measured values for k_1 are about 12-15% larger than the true value of k_1 , illustrating the enhanced elasticity due to the tension bonds.

For each row reduction we perform a linear regression on the force as a function of compression distance and obtain the corresponding value of the equivalent spring $\Delta F = k_{\text{eq}}\Delta x$. The graph of k_{eq} is shown in Fig. 2.7 and is linear as a function of $q/(p+1)$ as predicted by Eq. 2.32. As the crystal is compressed $q/(p+1)$ grows and therefore k_{eq} grows as we have a larger number of springs arranged in parallel

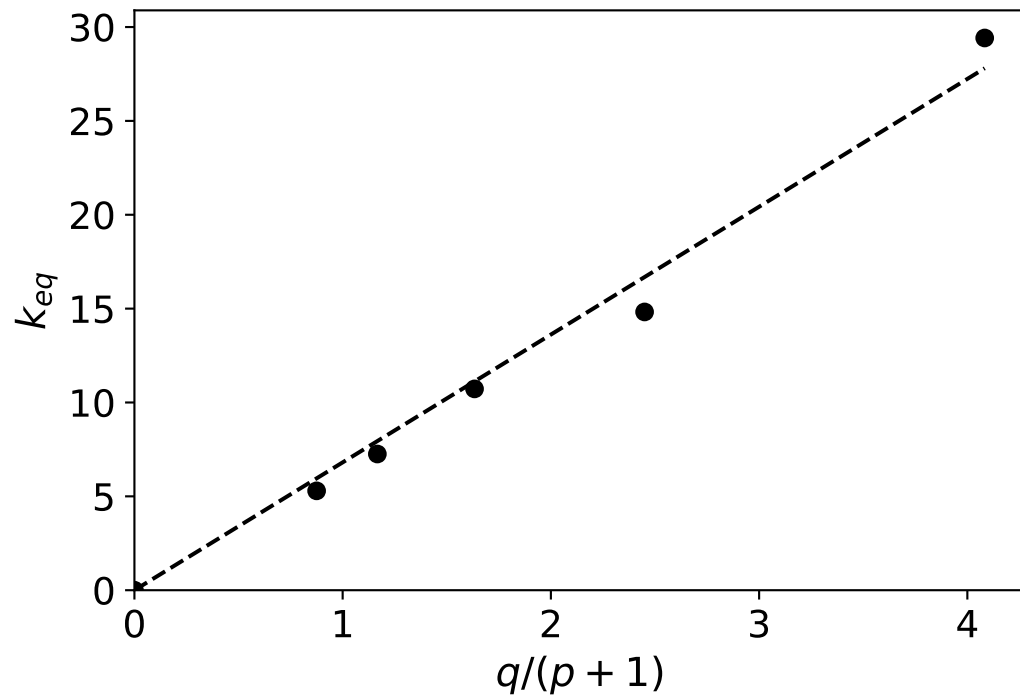


Figure 2.7: Linear fit for the compression of the equivalent spring constants, as a function of the aspect ratio of the array $q/(p+1)$ for 49 droplet array. Using Eqn. 2.32 and the linear fit gives us the spring constant for a single droplet, $k_1 = 7.08 \pm 0.6$.

and fewer in series. The linear fit of this graph gives $k_1 = 7.08 \pm 0.5$, which is higher than our theoretical $k_1 = 4.69$ (Eq. 2.18). This procedure was repeated for different runs with the same crystal configuration (thus different realizations of our slight polydispersity), as well as for arrays containing 20 to 400 particles, obtaining a mean value of $k_1 \approx 6.1$. As with the individual measurement of k_{eq} discussed above, the likely cause of the higher k_1 is due to the viscous forces acting on the larger droplet array, as well as the breakdown of the approximations used to calculate k_1 .

To understand how the viscous forces affect our system, consider a row reduction transitioning from p to $p - 1$ rows, for example as shown in Fig. 2.5 with $p = 7$ initially. The number of columns q is a function of the total number of droplets N and p , and thus increases from $q = N/p$ to $q' = N/(p - 1)$. We will continue by analysing the vertical displacement, parallel to the rows, of one of the droplets at the edge of the configuration – that is, at the top or bottom of a row. Before the row reduction the rows of the array have length $2Rq$, and $2Rq'$ afterwards. Taking the center of the array to be our origin, the displacement of an edge droplet during this row reduction is:

$$d_{\text{edge}} = \frac{N}{p-1} \frac{2R}{2} - \frac{N}{p} \frac{2R}{2} \quad (2.33)$$

where we have divided by two as the array expands symmetrically around the origin. The time needed for this transition to occur is the time needed for the walls to move the distance of one row, $t = \sqrt{3}R/v_{\text{wall}}$. Dividing Eqn. 2.33 by t we obtain:

$$v_{\text{edge}} = \frac{v_{\text{wall}}}{\sqrt{3}} \left(\frac{N}{p(p-1)} \right). \quad (2.34)$$

Based on Eqn. 2.34 we can see that the speed of an edge droplet depends on the size of the array, as well as which transition it is. Replacing Eqn. 2.34 into Eqn. 2.11 for α_2^{sim} we have:

$$\alpha_2^{\text{edge}} = \frac{1}{\sqrt{3}} \left(\frac{N}{p(p-1)} \right) \alpha_2^{\text{sim}}. \quad (2.35)$$

For the first transition in Fig. 2.5, we have $N = 49$, $p = 7$ and thus $\alpha_2^{\text{edge}} = \alpha_2^{\text{sim}}49/(42\sqrt{3}) \approx 2\alpha_2^{\text{sim}}$. For the last row reduction starting with $p = 2$, this becomes $\alpha_2^{\text{edge}} = \alpha_2^{\text{sim}}49/(2\sqrt{3}) \approx 14\alpha_2^{\text{sim}} \approx 0.7$. This shows that during the last row reduction, for the edge droplets the viscous forces are now comparable to the depletion forces, even for an array of modest size with $N = 49$.

We verified this computationally using $N = 49$ and using half and double our usual value of v_{wall} . As expected, the simulations running at double the wall speed had more significant viscous effects for the last row reductions, while the simulations running at half the wall speed had less noticeable viscous effects.

The next feature of Fig. 2.6 to explain is the peaks in the force. As the number of rows is reduced and the number of columns increases, Fig. 2.6 shows the force required for the fracturing increases significantly. This is because more depletion bonds need to be broken.

As we did previously for the three droplet case, we can obtain the depletion energy per bond from the force peaks for each transition, continuing from Eqn. 2.31 which we can rewrite as:

$$F_{\text{max}} = \sqrt{2E_1k_{\text{eq}}\Delta n} \quad (2.36)$$

where Δn is the number of bonds broken during the row reduction. To rewrite this equation we will use Eqn. 2.32 to replace k_{eq} with k_1 and $N = p \times q$ to eliminate q . We will additionally assume that the number of broken bonds per transition is $\Delta n = 2q$, which is true when the array fractures into equilateral triangles, as was the case in the original experiments. This leads to:

$$F_{\text{max}} = 2N\sqrt{\frac{k_1E_1}{p^3 + p^2}} \quad (2.37)$$

To test this we plot in Fig. 2.8 the force peaks F_{max} divided by the total number of droplets N in each simulation as a function of the $(p^3 + p^2)^{-1/2}$ for a wide range

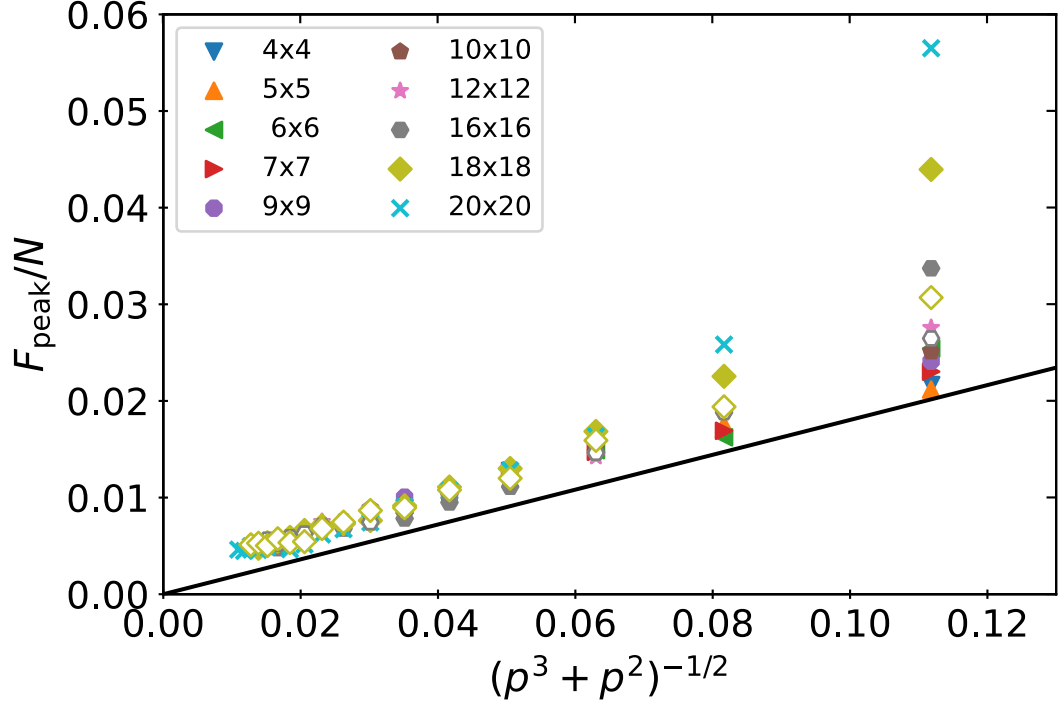


Figure 2.8: Evolution of the normalized peak height as a function of $(p^3 + p^2)^{-1/2}$ for a different variety of starting configurations. The solid line represent the values predicted by Eqn. 2.37. The discrepancies at the right side are due to the increasing influence of viscous forces, which become more significant for large arrays with small p . The right-most data correspond to $p = 4$. The hollow diamond and hexagonal markers correspond to 18×18 and 16×16 arrays, with wall speeds half of those used for all other simulations. For the compression of bigger arrays at low p , the decreased speed, and therefore, decreased viscosity, results in smaller force peaks.

of N and p . The solid line shows the prediction of Eqn. 2.37 using k_1 and E_1 from Eqs. 2.18 and 2.31.

Figure 2.8 shows that most force peaks exceed the expected value corresponding to Eq. 2.37. There are several reasons for this difference. First, Eq. 2.37 uses k_1 which neglects the influence of the tension bonds. Second, viscosity dissipates some of the energy the walls put into the system, which is more significant for bigger arrays and when the arrays have fewer rows p [thus higher $(p^3 + p^2)^{-1/2}$]. With fewer rows, the bubbles at the ends of the array must move faster to reach the new configuration, while the wall keeps moving at the same speed; see Eqn. 2.35. Equation 2.35 also shows that larger arrays (larger N) have larger viscous forces, in agreement with what

is seen in Fig. 2.8. The effect of viscosity is further evidenced by the smaller peaks corresponding to simulations of 16×16 and 18×18 , ran at $v_{\text{wall}} = 5 \cdot 10^{-5}$, half of the wall speed for all other simulations. Third, there are situations where $\Delta n > 2q$ (caused by more complex fracture events) which will be discussed in Sec. 2.4.3, which thus increases F_{max} .

To summarize, we have successfully replicated the experimental observation that each successive row reduction requires greater compression, as there are more depletion bonds that need to be broken [20]. Like the experiments, we successfully relate the spring constant of a single droplet to the array aspect ratio dependence of the wall forces [19]. Our results also illuminate the influence of viscosity (in Fig. 2.8), which is more observable in the simulations due to the larger nondimensional number α_2^{sim} (Eqn. 2.11).

The equivalent spring model is therefore a useful tool for understanding the characteristics of a nominally monodisperse droplet array as it is compressed. In the next section we will take a closer look at the behavior of arrays which are no longer considered monodisperse.

2.4.2 Bidisperse aggregates

As seen in the previous section, a raft made up of low polydisperse droplets is a model crystalline packing. In this section we introduce defects and increase the polydispersity of the simulated samples to study these new aggregates during compression, which more closely resemble glassy materials.

We start by analyzing the behaviour of bidisperse aggregates. In these arrays the particles can have a radius of either $R = 1$ or $R = 0.765$ (to match the experiments of Ref. [20]). We define the defect fraction ϕ as:

$$\phi = N_{\text{small}}/N_{\text{total}} \tag{2.38}$$

where N_{small} is the number of smaller droplets in the aggregate, and N_{total} is the total number of droplets. The defect fraction ϕ varies from zero to one. In the case where $\phi = 0$ or $\phi = 1$, we return to the monodisperse case seen in the previous section, corresponding to a crystal made exclusively of large or small droplets.

Figure 2.9 shows how the force profile changes as we substitute differently sized particles in a 20 droplet array, becoming progressively more disordered as the fraction of defects rises from $\phi = 0$ to $\phi = 0.5$. (The compression process is shown in Movies S2 and S3 in the Supplemental Material of our published work[21]). Figure 2.9(a) shows the force profile for the monodisperse droplet aggregate shown in Fig. 2.9(b), which as discussed in the previous section shows clear force peaks connected to well-defined row reductions. Introducing a single small droplet results in a force profile and droplet array shown in Figs. 2.9(c,d). This single defect causes the appearance of smaller peaks, signalling additional smaller fracture events and thus a more disordered row reduction. Figures 2.9(e-h) show the force profile and initial droplet configuration for $\phi = 0.25$ and $\phi = 0.50$. Introducing more defects introduces more small force peaks. At a defect fraction of $\phi = 0.5$ there are no distinct “row reductions”, but rather a nearly continuous series of small fractures.

In the prior experimental work, Ono-dit-Biot *et al.* developed a predictive model for the number of peaks in the force profile for a compressed aggregate [20]:

$$\frac{\Delta N(\phi)}{\Delta N_{\text{peak}}} = 2\sqrt{(1-\phi)\phi}, \quad (2.39)$$

where $\Delta N(\phi) = N(\phi) - N(0)$ is the excess number of peaks $N(\phi)$ observed for a given defect concentration over the number of peaks $N(0)$ for the original aggregate ($N(0)$ is the number of starting rows minus one), and ΔN_{peak} is a fitting parameter to the highest amount of peaks for a given droplet configuration.

The prediction given by Eqn. 2.39 describes the simulation data well, as shown

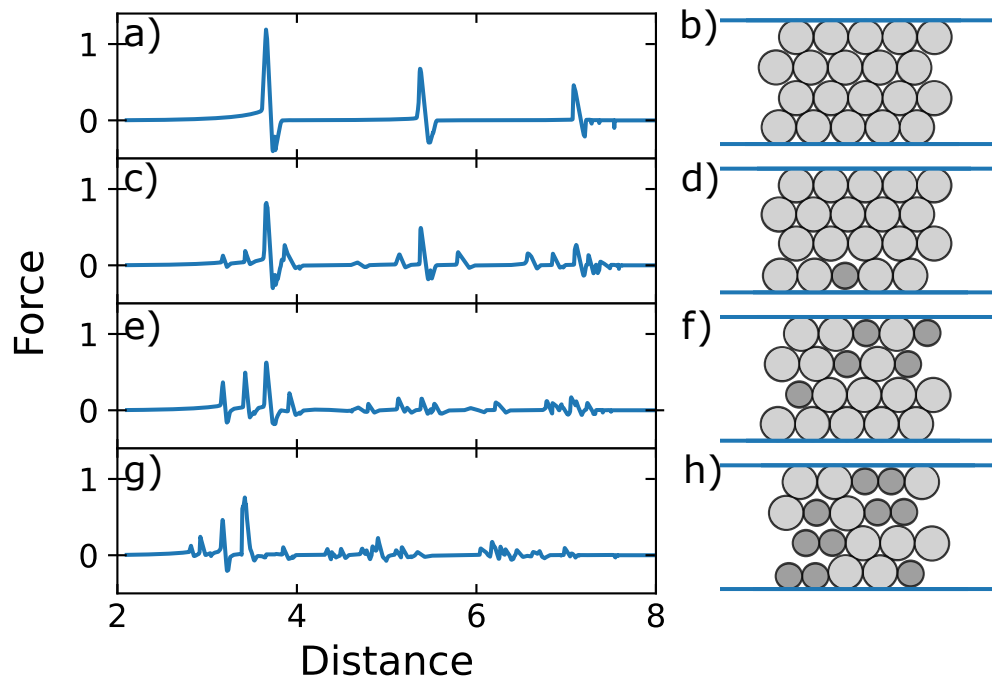


Figure 2.9: Evolution of the force profile as the defect fraction ϕ increases. The more bidisperse the aggregates becomes the noisier the force profile is; the individual fracture events involving many droplets split into a broad sequence of smaller fractures. The images in the right columns are snapshots from the state prior to compression of the system at distance 8.

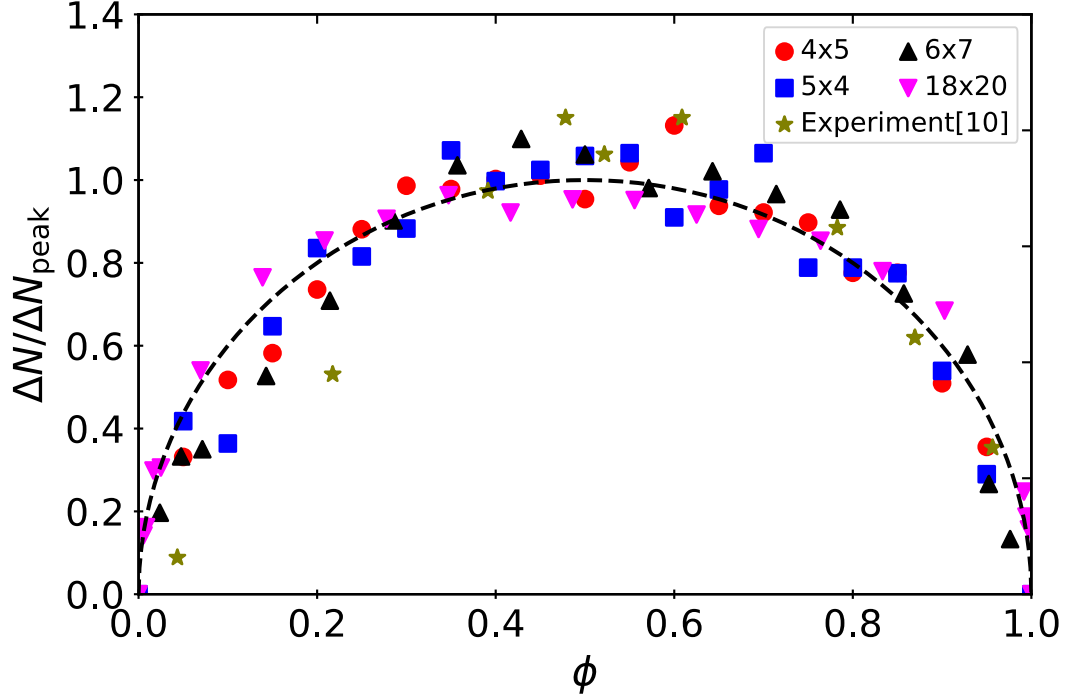


Figure 2.10: $\Delta N(\phi)$ normalized by the fitting parameter ΔN_{peak} for five different droplet arrays. The dashed line corresponds to the prediction of Eqn. 2.39. Four of the data sets correspond to simulation data, while the points with the star marker are from the experimental data of Ono-dit-Biot *et al.* [20]. The experimental droplet array consists of 23 particles in three columns containing 8, 7, and 8 particles.

for four examples in Fig. 2.10 where the data have been scaled in each case by the ΔN_{peak} that best fits each data set. Furthermore, this data collapse agrees with the experimental results of Ref. [20] (star symbols in Fig. 2.10), and extends their 3×8 array results up to an 18×20 droplet array. Above this size, the peaks from individual fracture events begin to blur together around $\phi \approx 0.5$, making it challenging to correctly measure $N(\phi)$.

Additionally we can take the derivative Eqn. 2.39 with respect to ϕ :

$$\frac{\Delta N(\phi)'}{\Delta N_{\text{peak}}} = \frac{1}{\sqrt{\phi}} \frac{1-2\phi}{\sqrt{1-\phi}}, \quad (2.40)$$

which indicates the increase in peaks in an array as a function of the defect fraction.

We also note that when $\phi \rightarrow 0$ and $\phi \rightarrow 1$, $\frac{\Delta N(\phi)'}{\Delta N_{\text{peak}}} \rightarrow \infty$, which means that for larger arrays, even a small amount of bidispersity produces a greater amount of peaks compared to smaller arrays.

We can also consider how the bidisperse sample compares with a nominally single-component sample composed of polydisperse particles. To do this, we use particles with sizes distributed according to a Gaussian, characterized by polydispersity δ defined as the standard deviation of the distribution divided by the mean. Additionally we can calculate the polydispersity of the bidisperse arrays using the following equation[104]:

$$\delta = (R_{\text{small}} - R_{\text{big}}) \frac{\sqrt{(1-\phi)\phi}}{(1-\phi)R_{\text{big}} + \phi R_{\text{small}}} \quad (2.41)$$

Figure 2.11 shows the amount of fracture events occurring during the whole compression as a function of polydispersity. The blue squares correspond to the Gaussian distribution, and the red circles correspond to the bidisperse distributions considered above, now plotted as a function of δ calculated from each distribution's standard deviation and mean size. For the discrete bidisperse data set, we have used the 4×5 droplet case previously shown in Fig. 2.10. The continuous polydispersity case has many more fracture events than the bidisperse distributions with equivalent δ . Examining the individual movies, the increase in fracture events is because the case of continuous polydispersity acts to introduce weak points into the array in many locations simultaneously. That is, the continuous polydispersity case is somewhat analogous to a bidisperse array with $\phi \approx 0.5$ and a size ratio that grows with increasing Gaussian width δ .

2.4.3 Competing fractures

The larger disorder in the fracture process when adding defects is expected. We additionally observe a new behavior in droplet aggregates even with low polydispersity

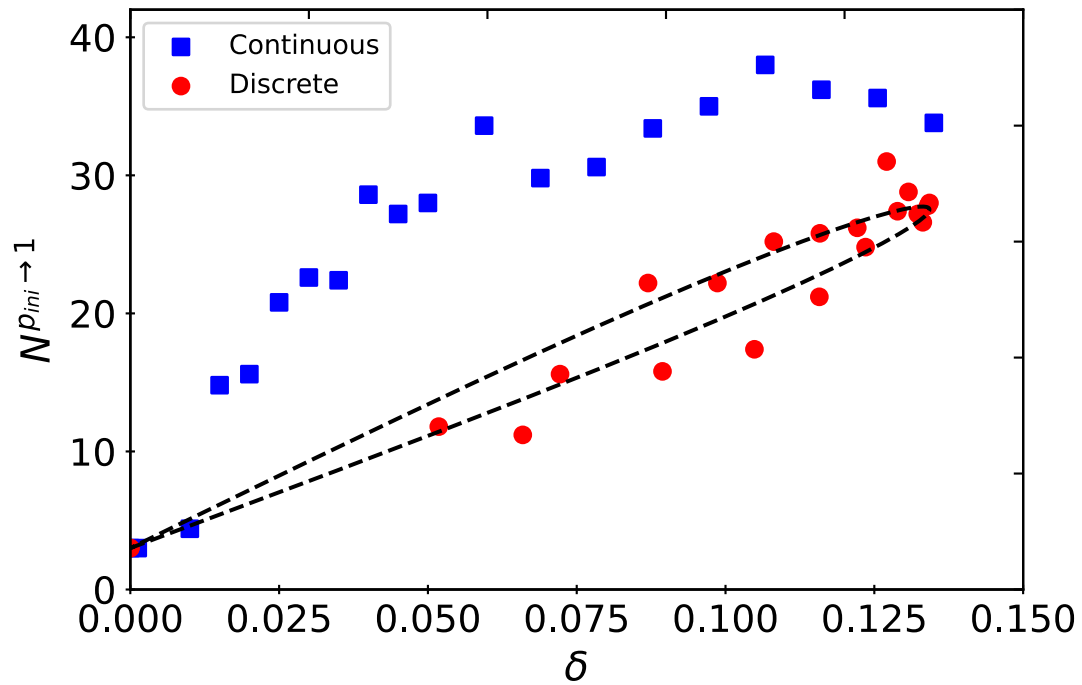


Figure 2.11: $N^{p_{ini} \rightarrow 1}$ (the amount of fracture events from the initial number of rows to one) as a function of the polydispersity δ for the discrete 4×5 bidisperse case used in Fig. 2.10, and a continuous size distribution. The amount of fractures events depends on the chosen size distribution, with the discrete case increasing somewhat linearly, while the continuous case grows nonlinearly. The dashed line corresponds to the prediction of Eqn. 2.39. For the bidisperse case $\delta(\phi)$ is not symmetric between ϕ and $(1 - \phi)$, so thus Eqn. 2.39 has two branches as shown [105].

not seen in Ref. [20]: competing fractures. In Sec. 2.4.1 we focused on the compressed crystal undergoing single coordinated fractures resulting in a change from one hexagonal array to a smaller array with one fewer row. However, sometimes two or more fractures nucleate at multiple sites in the array. As the droplet raft is further compressed, these fractures propagate leading to misalignment: the compressed array, upon completion of the fractures, is no longer hexagonal. Instead, we see holes or other defects in the structure. An example of competing fractures can be seen in Fig. 2.12. For this particular example in the first snapshot [Fig. 2.12(a)] the droplets are compressed throughout the whole array, with some variability due to the minimal underlying droplet polydispersity. This pressure is alleviated by breaking depletion bonds, as seen in Fig. 2.12(b): but this occurs mainly on the upper portion of the array, while the lower half remains compressed. Eventually the lower end starts another fracture event, but the second fracture does not align with the first fracture, as seen in Fig. 2.12(c). This results in a disorderly row reduction as seen in the last snapshot Fig. 2.12(d).

A similar example is present in Fig. 2.13 for a 36 droplet case. Upon compression, a fracture originates first at the “top” of the array, with a secondary fracture nucleating later at the “bottom.” Both fractures fail to align, causing again a disorderly collapse in the crystal. Another example of competing fractures in large arrays is presented in Supplemental Material Movie S4 of the published work this chapter is based on, showing the compression of a 121 particle array [21].

While Fig. 2.12 is a small droplet array, we would expect that in larger arrays there are more potential sites for fracture events to start. Furthermore, even if a fracture starts in one location, it propagates to other locations at a finite speed: it is possible that the fractures can’t spread fast enough to cover the whole crystal before another fracture event is nucleated elsewhere. To test this suggestion, we measure the fraction of row reductions that occur via competing fractures for different numbers of

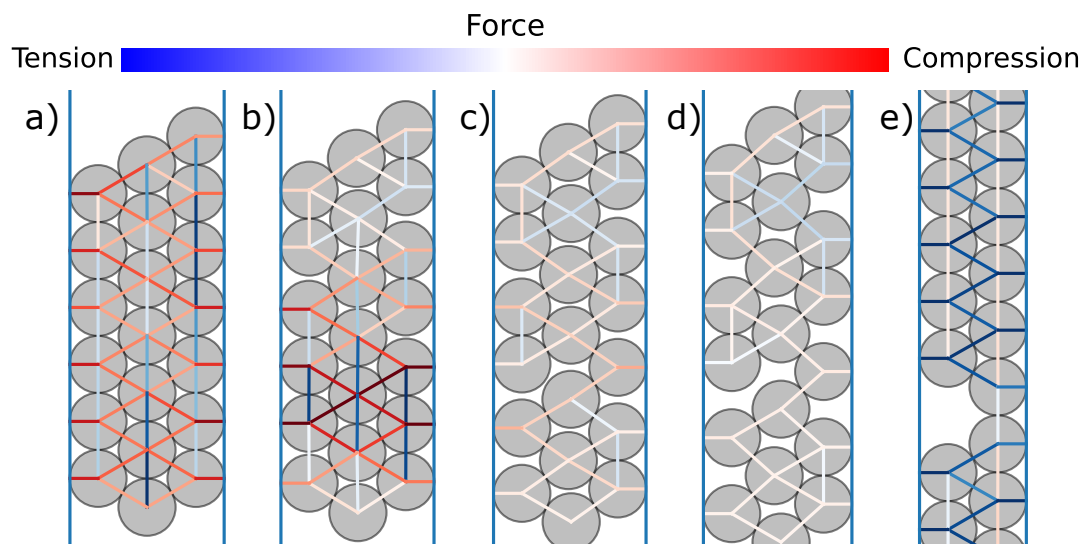


Figure 2.12: Successive images of a 20 droplet aggregate undergoing a second row reduction, from the original 4 rows by 5 columns configuration. By panel (c) we can see the formation of two fractures, which are misaligned as they propagate through out the array. Thus the collapse in (d) is disordered, and the final packing with a defect in (e).

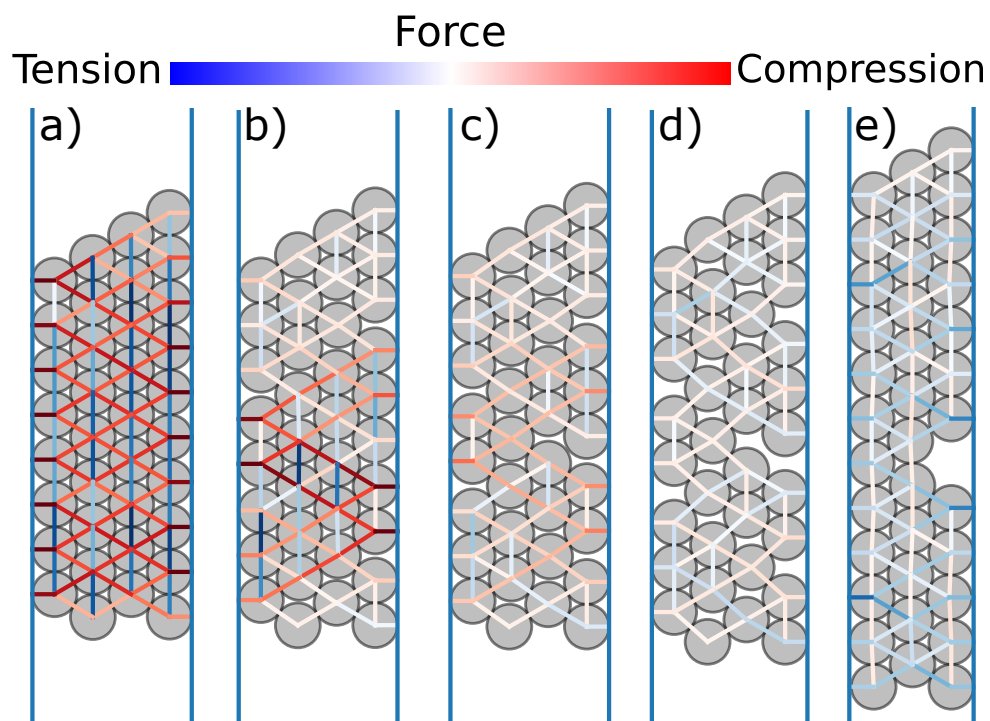


Figure 2.13: Successive images of a 36 droplet aggregate, undergoing its third row reduction from the original six by six configuration. By panel (c) we can see the formation of two fractures, which are misaligned as they propagate through out the array. Thus the collapse in (d) is disordered, and the final packing with a defect in (e).

droplets N and plot this in Fig. 2.14. This fraction is defined by averaging over several simulations with the same N but varying the random seed for the polydispersity. In particular, for each simulation run we count the number of row reductions that have multiple competing fractures. The one exception is that we ignore the very last row reduction ($2 \rightarrow 1$) which is always clean; thus if we start with p rows, there are $p - 2$ total row reductions which could potentially have competing fractures. Then we calculate the average fraction of row reductions with competing fractures over all runs with the same starting configuration. The data points are plotted as a function of $1/N^{1/2}$ and exhibit a fairly linear trend: larger arrays have more competing fractures, with an extrapolation to all fracture events being competing fractures in the $N \rightarrow \infty$ limit. The limit where no competing fractures occurs corresponds to a 3×3 array ($N = 9$) for which there is no longer a possibility for competing fractures; the array is too small to fit two fracture events. Overall, Fig. 2.14 confirms the basic idea, that larger arrays have more potential ways for competing fractures to occur.

We investigate how the presence of competing fractures is influenced by the initial droplet array aspect ratio, defined as $AR = q/p$. The results are shown in Fig. 2.15 based on calculations with $N = 144$ droplets. A lower aspect ratio corresponds to a “taller” initial configuration with many rows, and as expected the initial row reductions have only a small amount of competing fractures. As the array becomes wider, competing fractures become more prevalent, similar to the wide array shown in Fig. 2.12. This confirms that for a wider configuration the compression from the wall at the far ends of the crystal can produce separate fracture events. The data should be interpreted with caution: the “taller” configurations with aspect ratio less than 1 will be compressed and pass through the “wider” configurations, and thus some number of the competing fractures observed for the taller configurations occur when the array is at a later compression stage and is thus wider. This likewise is a factor in the data of Fig. 2.14, that the larger N arrays sample higher aspect ratio configurations during

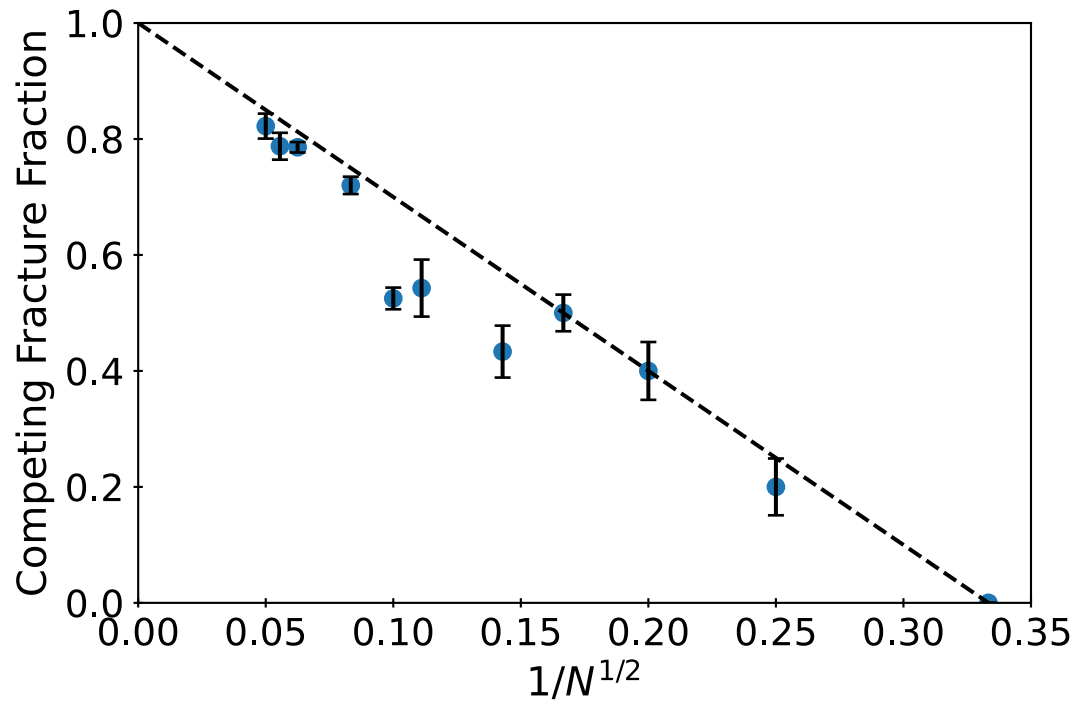


Figure 2.14: The fraction of row reductions observed to have competing fractures as a function of $1/N^{1/2}$, using the number of droplets N . The data correspond to initially square arrays such as the array in Fig. 2.5(a). The error bars reflect the standard deviation over five runs.

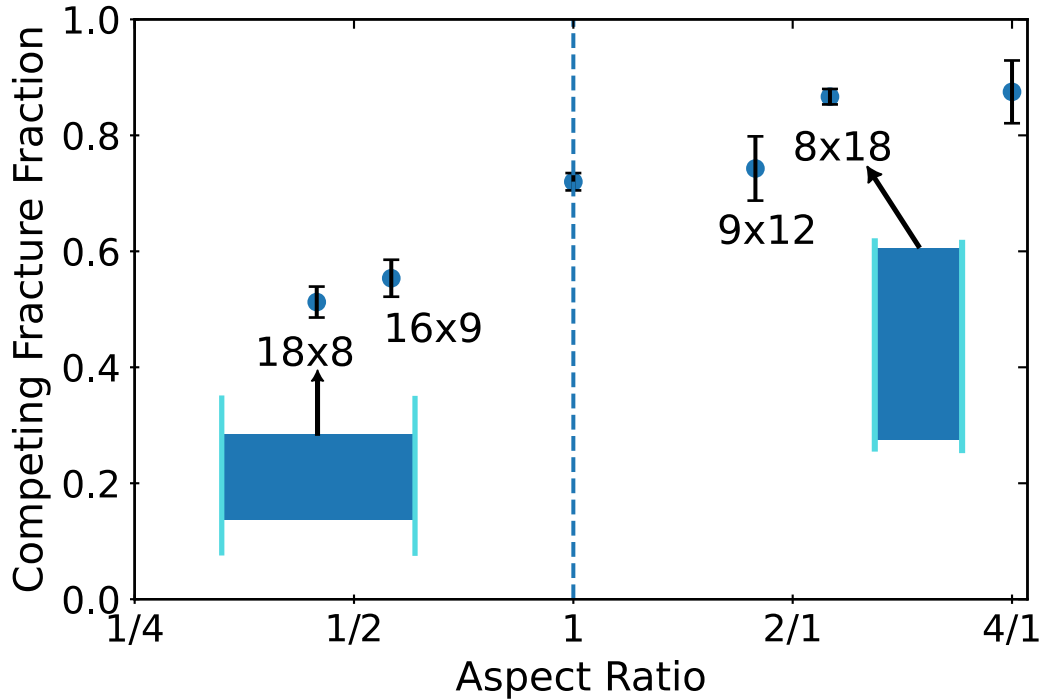


Figure 2.15: The fraction of competing fractures as a function of aspect ratio using $N = 144$ droplet configurations. The aspect ratio is defined as q/p , with a low aspect ratio corresponding to “tall” configurations (many rows parallel to the walls, with the walls starting quite far apart), and high aspect ratios to “wide” configurations (few rows between walls that start close together). The error bars reflect the standard deviation over five runs.

their compression which have the higher propensity for competing fractures.

Competing fractures were not seen in the experiments of Refs. [19, 20]. We speculate that this may be due to the experimental challenge of aligning the two glass pipettes that serve as the compressing walls. To test this hypothesis, we study the dependence of competing fractures on the relative angle of the moving wall to the stationary wall, with 0° representing perfectly parallel alignment. The data are shown in Fig. 2.16 for arrays with 20 to 180 droplets as indicated. As the angle of the wall increases, the frequency of competing fractures decreases, reaching a minimum close to an angle of 0.2° . This is due to the wall compressing on one side of the array first, which results in fractures nucleating on that side first, and spreading throughout the crystal as the wall continues moving. However, at still higher angles, close to the 0.2°

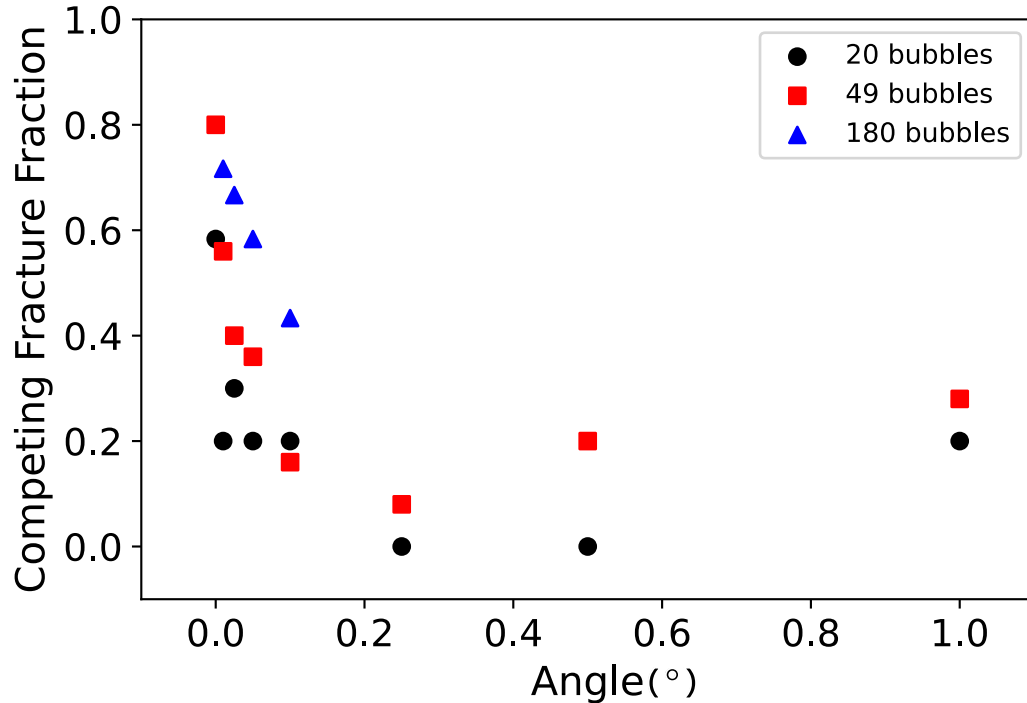


Figure 2.16: The fraction of competing fracture as a function of the angle between the two walls, for three different droplet array sizes as indicated. The data suggest a slight angle between the walls can dramatically decrease the frequency of competing fractures.

angle for the arrays shown in Fig. 2.16, the compression is sufficiently uneven that the number of rows between the walls becomes less well-defined, leading to an increase in competing fractures. A tilt angle of 0.2° is plausible for the experiments, and may have biased the experimental observations towards single fractures.

2.5 Conclusions

We have simulated a variety of two-dimensional arrays of droplets with attractive interactions as they undergo compression. Inspired by the prior experimental work of Refs. [19, 20], we reproduce and extend their key results. First, we show how the effective elastic properties of the droplet arrays are related to the intrinsic spring constant acting between a pair of contacting droplets. In particular, some of these springs are compressed and others are under tension; the tension bonds act to increase

the overall spring constant exhibited by the droplet array. Second, we confirm how the force required to initiate a fracture event scales with the aggregate size, extending the results to more droplets than the experiments studied. Third, we find that intentionally adding defects into the otherwise hexagonally ordered array dramatically increases the number of fracture events, while at the same time decreasing the force required to initiate those fractures. The dependence of the fracture events on defects is in quantitative agreement with the model developed in Ref. [20], and with the simulations we were able to extend the size of the cluster studied by an order of magnitude more droplets. Of interest is that the number of excess fractures scales as $\sqrt{\phi}$ for a small fraction ϕ of defects. The derivative of this diverges as $\phi \rightarrow 0$, indicating that for a perfect crystal, adding in any density of defects dramatically increases the ease of breaking the crystal. The maximum disorder occurs when the sample is composed of an equal mixture of two sizes of droplets, in reassuring agreement with the decades of simulations which have used mixtures of equal numbers of two particle sizes to model glasses, for example in the classic papers of Kob and Andersen [106, 107].

Our simulations also found a phenomenon not observed in experiments, which is the presence of competing fractures. This occur when two independent fracture events start in different locations, and when they propagate through the sample, they do not match in the middle. Competing fractures result in the post-fracture array being more disordered. These are more prevalent for larger droplet arrays, giving some sense of why they might not have been observed in the experiments. We demonstrated that if the two walls compressing the crystalline aggregate are slightly tilted with respect to each other, this helps bias the formation of cracks toward the more compressed side. A tilt angle of $\sim 0.2^\circ$ is optimal in the simulations for suppressing competing fractures, and this is entirely plausible to have been present in the experimental work [19]. This also suggests that in real crystals undergoing compression, slight mis-alignment of compressing surfaces could affect how samples fracture. Note that in our simulations,

symmetry is broken by the slight polydispersity of droplet sizes – introduced to match the experimental polydispersity. Such polydispersity would not be present in ideal crystals. Nonetheless, thermal fluctuations might facilitate multiple sites for fractures to be initiated.

Chapter 3

Amorphous flow of highly polydisperse disks

The work presented in this chapter has been submitted for publication to “PHYSICAL REVIEW E”, and a preprint of this paper has been uploaded to arXiv [108]. We study the particle-scale motion of highly polydisperse hard disks flowing in a two-dimensional bent channel. We use various size distributions of particles, in which the largest particles are up to five times larger than the smallest. The disks are pushed through an L-shaped channel to drive the particle rearrangements. Although the mean flow is essentially independent of the polydispersity, the motion of individual particles becomes more nonaffine on average for higher polydispersity samples. We characterize the nonaffine motion, finding a qualitative difference in the behavior of small and larger particles: the smaller disks have more nonaffine motion, induced by the larger particles.

3.1 Introduction

The behaviour and properties of amorphous materials and their flow has been a subject of extensive study for decades [86, 87, 90, 109–112]. These amorphous materials

are extremely common, both in nature and industry, in the form of emulsions, granular media, food products and foams, among many others [89, 113]. Much prior research has been dedicated to the study of the flow and rheological properties of these materials, however most of this work has been done on systems with particles of similar sizes and properties [83, 109, 111, 112, 114–123]. In contrast with these model systems, many natural systems and materials have components with a range of sizes. For example, the size ratio between the largest and smallest particles can be a factor of 10 or more [4, 5, 124–126]. The presence of disparate-sized particles is known to affect the flow behavior of various systems, including sand and gravel deposition [6, 33–35], hopper flow [127–129], and geophysical phenomena such as avalanches, land slides, and glacier flow [5, 115, 130–133]. Mixtures of various size components can also determine consistency and texture in food products [113, 134].

The above mentioned examples all have highly polydisperse particle size distributions, that is the broadness in particle size in a given distribution. These systems show complex structural and dynamical properties due to their spatial heterogeneity.

The study of these kinds of systems has led to interesting physical behavior when compared to their monodisperse counterparts. As an example, polydisperse hard spheres can phase separate into multiple crystalline phases [135]. In active matter, polydispersity leads to the emergence of new phases [136]. Experimental and computational studies on the compression and stretching of particle rafts have shown that polydispersity greatly affects their structural properties, such as their compressional yielding threshold [20, 21]. In granular materials, force chains become drastically more heterogeneous in more polydisperse systems, affecting the material’s jamming point and rheological properties [137–140]. In particulate suspensions, the polydispersity of the particles strongly impacts the viscosity of the suspension: for example, adding small particles can lower the viscosity [141].

Previous studies of sheared soft materials typically wish to avoid crystalline order,

so often a bidisperse mixture of particles is used, or a single type of particle with mild polydispersity [109–111, 111, 112, 114–121]. Polydispersity δ is defined as the standard deviation of the particle radii divided by the mean radius. A frequently studied system is bidisperse, with equal numbers of small and large particles with size ratio 1 : 1.4, yielding $\delta = 0.17$ [57, 116, 117, 142, 143].

Two prior studies examined highly polydisperse emulsions ($\delta \geq 0.5$), with the size ratio between the largest and smallest particles as large as 10 : 1 [32, 144]. These studies found that large and small particles play different roles in the flow of the sample, with large particles moving more smoothly, while small particles move more erratically. This has implications for how particles are mixed and also consequences for the rheological response: highly polydisperse systems have well-mixed small particles and are easier to flow [32]. These two studies only considered emulsion droplets at high volume fractions (above jamming); because the droplets are soft they can still flow, but leaving unanswered the question as to whether these prior observations generalize to hard particles at packing fractions below jamming.

In this chapter we will show the effect particle size distribution has in the flow, non-affine displacement, and local particle rearrangement in sheared granular materials. The granular particles used for this work, consist of hard cast acrylic disks. We use 11 different particle size distributions with varying polydispersity, ranging from $\delta = [0.2, 0.48]$. We push mixtures of these disks through an L-shaped channel to cause the particles to rearrange, and study individual particle motions during this flow. We find that large particles are more likely to follow the mean flow, and more likely to perturb the motion of nearby smaller particles so that the latter do not follow the mean flow. Our observations confirm the prior understanding [32, 144], extending those observations to hard particles. We additionally find that the influence of the perturbation from the larger particles extends only a short distance from the surface of the large particles, about 2-3 small particle diameters.

This chapter consists of 5 sections; Section 2 will review the experimental set up and image analysis procedure. Section 3 will characterize the properties of the flow in the case of the lowest polydisperse size distribution. Section 4 will analyze the local particle rearrangements and non affine displacements for all particle size distributions. Finally, Section 5 will look at these properties again but taking into account the spatial heterogeneity, using a spatially dependent time step which achieves a somewhat homogeneous strain field. This spatially dependent time step is then used to calculate the displacement properties of the particles studied in the previous sections.

3.2 Experimental methods

The particles in the experiment were made using cast acrylic sheets (thickness of 2.9 mm). The disks used in the experiments were produced by cutting the acrylic sheets using a laser cutter. Frosted rectangles were etched on the center of disks during the cutting procedure, to facilitate tracking. Each rectangle is proportional to the diameter of its corresponding particle, to simplify not only positional tracking and particle size identification, but rotational orientation as well, which can be researched in future projects. As a final step, the frosted rectangles were painted red using a felt-tip marker, to make particle tracking easier. A sample of finalized particles is shown in Fig 3.1(a). Here we can see a wide variety of particles with radii ranging from 0.635 cm to 2.22 cm. It is worth noting that the thickness of the sheet and the smallest radius have been chosen so that the particles don't tip over when pushed. The largest particle on the left has a diameter of 5.7 cm, with its rectangle being 3.5 cm long.

The experimental device used for this project consists of a large square aluminum base, with each side measuring 53.3 cm, on which we can screw-in several divisions. This work will focus on the 'L' configuration with the dimensions given in Fig. 3.2.

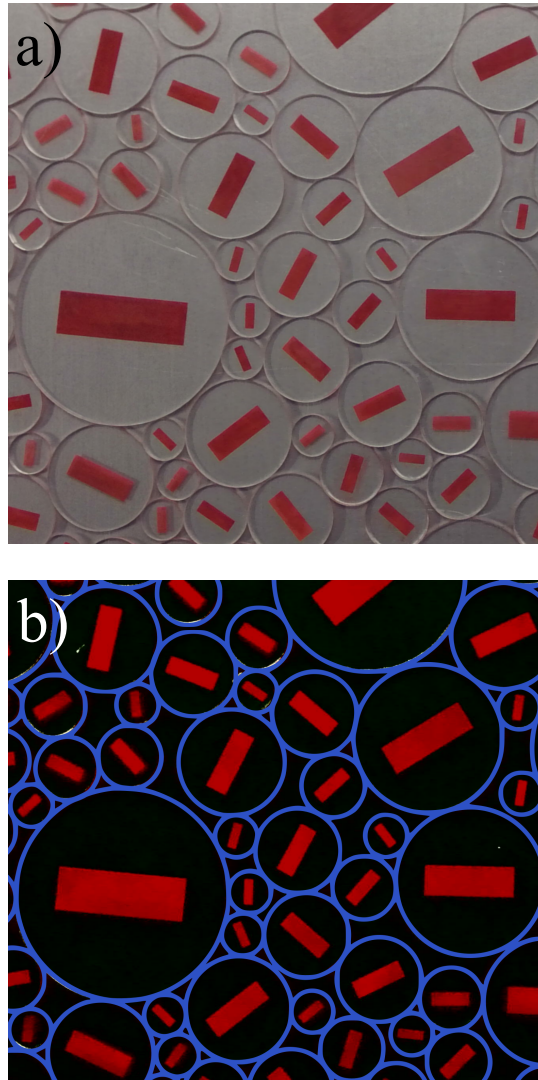


Figure 3.1: Sample image illustrating the process used for image analysis and particle tracking. (a) Photograph of the experimental device with a size distribution already in place under normal lightning conditions. (b) Photograph of the same frame using green/yellow lightning to highlight the red rectangles painted on the particles. We have superimposed blue rings to illustrate the results of our particle tracking. The largest particle on the left has a diameter of 5.7 cm, with its rectangle being 3.5 cm long.

This configuration consists of a track of total length 75.4 cm, bent at a right angle at the 37.7 cm mark, and with a 20.5 cm width opening. To push the particles through our experimental setup at a steady velocity we use mechanical plungers, with a set speed of $v_p = 0.22$ cm/s, and maximal extension of 10.7 cm.

In order to ensure a two dimensional flow of the disks confined to the surface of the device and prevent the particles from flowing over one another, a transparent acrylic sheet is screwed on top of the experimental apparatus. This sheet can be easily removed to facilitate the placements of particles into the device.

To record the particles, we used a MOKOSE UC70 camera with 2100×2100 pixel resolution, operated at 6 frames per second. The camera is placed directly above the experimental device. We light the experiment using an array of colored LED lights, diffused through a screen, to achieve as homogeneous a light source as possible. The LED lights were set to a yellow/green color, to make the red rectangles on the particles contrast better against the reflective aluminum background, and later on during video processing we can obtain a bright highlight of the rectangle by subtracting the green channel from the red channel.

We also measure the relevant friction coefficients in the experiment. The friction coefficients between the particles and the aluminum base are measured by tilting the surface until the disks move, and measuring the subsequent velocity of the sliding disks. We obtain $\mu_{\text{static}} \approx 0.5$ and $\mu_{\text{dynamic}} \approx 0.3$. The value of μ_{dynamic} combined with the low plunger speed we use allows us to calculate the stopping time at $\Delta t_{\text{stop}} \sim 7 \times 10^{-4}$ s. Essentially, when the plunger stops moving, particles stop instantaneously; inertia is negligible. The negligible effect of inertia in this experiment is comparable to the “quasi-static” conditions setup in the Chapter 2. The friction coefficients between the acrylic particles themselves are also measured: $\mu_{\text{static}} \approx 0.4$ and $\mu_{\text{dynamic}} \approx 0.3$.

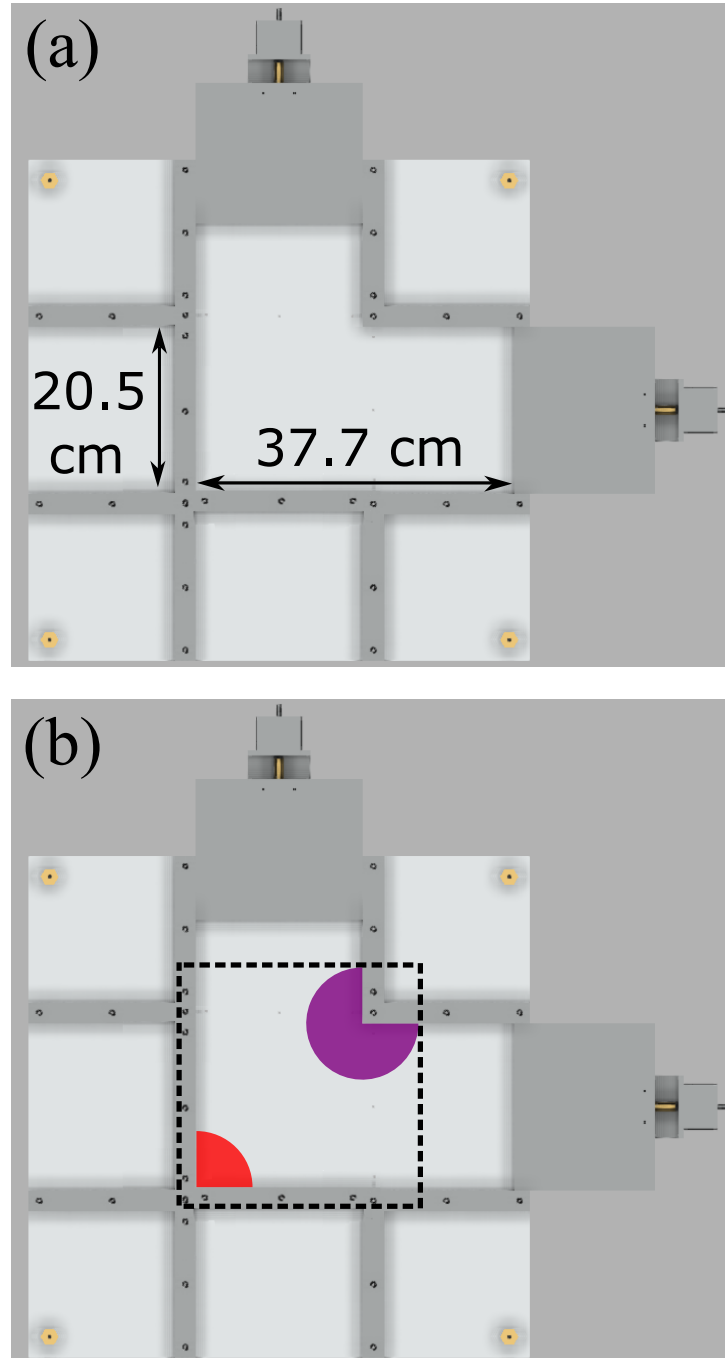


Figure 3.2: Top down schematic of the experimental device, set up in the "L" configuration. Plungers have been placed at each end of the flow geometry, this allows us to push the particles back and forth. The plungers both move at a set speed $v_p = 0.22\text{cm/s}$ and maximal extension of 10.7 cm. In Fig. (a) we show the dimensions of our system. Fig. (b) shows as red quarter circle, what we call the closed corner, or the bottom right corner. The purple 3/4 circle represents the "upper right corner" or "open corner". Finally the dashed square shows an approximate area of what we will refer later on as the "central" area, region or zone. The dashed square and circular circle are illustrative representations meant to give an approximate location of the these canal features.

3.2.1 Experimental procedure

To set up the experiment, the particles from a chosen size distribution are randomly placed in the surface of the configuration, which we then cover with the previously mentioned acrylic sheet. The particles are then pushed through the experimental device in a cyclical manner; a diagram explaining the experimental process is shown in Fig. 3.3. First one of the plungers will push the particles through the canal, the plunger at the other end is fully retracted, leaving enough space for the particles to move into. Once the first plunger has pushed to its maximum extension, it will retract fully back to its initial position, leaving space for the particles in the next cycle. After the first plunger has fully retracted, the plunger on the other end becomes active, repeating this procedure.

The above described procedure repeated is 10 times per experiment. During the first two cycles, we observe that the area fraction rises nontrivially due to particle rearrangements. Accordingly, we only analyze the final eight cycles for which the area fraction has reached a steady state. Once a run is completed, we remove the top cover, randomize the position of the particles using a random number generator for the positions, and carry out the next run of the experiment using the same procedure. For each size distribution, we carry out five runs, each with randomized initial positions.

3.2.2 Particle size distributions

At this point it is important to describe the features of the particle size distributions chosen for this project. As mentioned above, our aim is to study the effect of particle size diversity on the flow of our particles. The quantity which characterizes the size variety in a particle size distribution($P(R)$) is the polydispersity (δ):

$$\delta = \sqrt{\langle \Delta R^2 \rangle} / \langle R \rangle \quad (3.1)$$

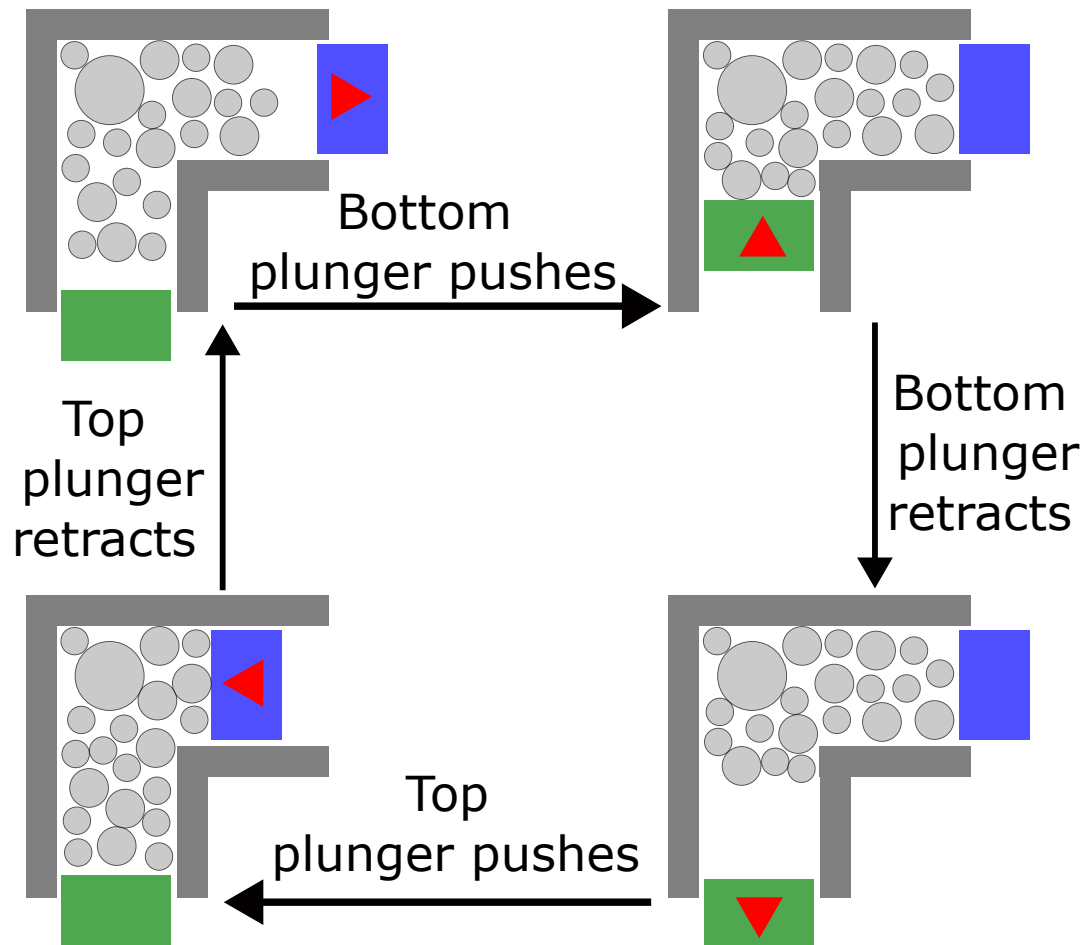


Figure 3.3: A top down sketch of the experimental device, setup in the “L” configuration. Plungers have been placed in such a manner as to block the outlets and study the sloshing back and forth of a given particle configuration.

Where R is a the radius of a given particle, $\Delta R = R - \langle R \rangle$, and the moments of R (and ΔR) are given by $\langle R^n \rangle = \int R^n P(R) dR$ (and $\langle \Delta R^n \rangle = \int \Delta R^n P(R) dR$).

Size Distribution	Size Ratio	Number Ratio	δ
Bidisperse	3:2	1:1	0.20
T1	4:3:2	1:8:8	0.23
T2a	6:3:2	1:24:24	0.27
T2b	6:3:2	1:18:18	0.29
T2c	6:3:2	1:11:11	0.32
T2d	6:3:2	1:9:9	0.35
T3	8:3:2	1:26:26	0.35
T4	10:3:2	1:28:28	0.42
C1	6 to 2	1 to 25	0.31
C2	8 to 2	1 to 50	0.40
C3	10 to 2	1 to 55	0.48

Table 3.1: Table with all the disks size distributions used in this Chapter. The first column shows the name of each distribution, in the second and third column we show the size and number ratio for all particles, respectively. The last column shows polydispersity of each distribution. For the C1 size ratio is; 2 : 3 : 4 : 5 : 6, for C2; 2 : 3 : 4 : 5 : 6 : 7 : 8, and for C3; 2 : 3 : 4 : 5 : 6 : 7 : 8 : 9 : 10. For more information about the number ratio of C1,C2 and C3, Fig. 3.4 shows a histogram with the amount of particles of each size in these distributions.

Specifically, there are a total of nine different radii that we use. In terms of $a = 0.3175$ cm (an eighth of an inch), the smallest particles have a radius $R_0 = 2a = 0.635$ cm, and the other radii are defined by $R_n = (n+2)a$, up to $R_8 = 3.175$ cm. More precisely these radii are [0.64, 0.95, 1.27, 1.59, 1.91, 2.22, 2.54, 2.86, 3.18] cm, labeled R_0 to R_8 respectively. Table 3.1 contains information about the size ratio, number ratio and polydispersity of each size distributions. The bidisperse distribution has equal numbers of R_0 and R_1 sized particles, and as mentioned before is the distribution with lowest polydispersity which does not crystallize. The tridisperse distributions, labeled T1 through T4, are built using R_0 and R_1 particles with added particles of greater size. These larger particles are R_2 for T1, R_4 for the T2 sets, R_6 for T3, and finally R_8 for the T4 distribution. Note that the T2 sets are composed of 4 subsets, each containing different amount of R_4 particles, and thus different polydispersity,

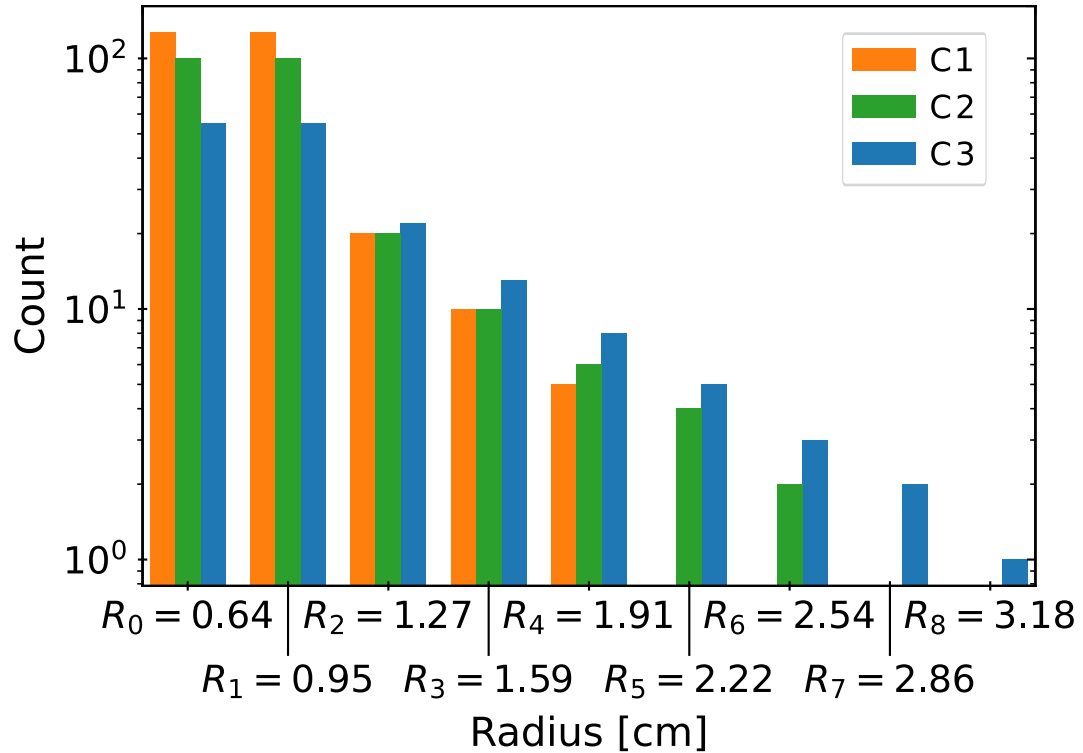


Figure 3.4: Histogram for the three continuous distribution of particles, C1, C2 and C3. These distributions are built using particles sizes “continuously”, starting from R_0 and R_1 , to a larger particle size, including all radii in between.

but same size ratio between particles. Fig. 3.4 shows a histogram of the particle counts for the continuous distribution, labeled C1, C2 and C3. These distributions are built with equal numbers of R_0 and R_1 particles, and lowering number of larger particles, continuously including all sizes in between R_0 and the largest particle of that distribution (R_4 for C1, R_6 for C2, and R_8 for C3).

3.2.3 Image analysis

The first step in our image analysis is to split each frame of a recording into its corresponding RGB values. We then subtract the green channel from the red channel, which results in the red rectangle of each particle to be strongly highlighted against a mostly dark background. Once all the frames in the recording have been processed we proceed to identify the particle in each frame, by identifying group of connected pixels

above an intensity threshold. From each group we take the center of mass, total pixel count, area, and orientation, among other quantities, which we then used to filter out falsely identified particles. After we have identified the particles in each frame, we tracked their trajectory using standard software [145]. In Fig. 3.1(a) we show an example of a raw image of our disk particles, and in Fig. 3.1(b) the same frame is shown, but using our particular lighting conditions described above, and using using a variety of image adjustment methods, to further highlight the red rectangles of the disks. In Fig. 3.1(b), we also shown superimposed rings, colored in cyan, to reflect the results of our particle tracking method. Note that while we have measured the orientation of each particle, we did not see anything of strong interest, for further information please refer to App. A.

3.3 Results

3.3.1 Mean Flow

We first consider the mean flow properties of our samples. We start by calculating the displacements of the particles using a time scale $\Delta t = 5$ s which corresponds to roughly a tenth of the total duration of a cycle (the disks moving in one direction as one plunger pushes on them). During this time interval, the plunger moves $\Delta r_p = v_p \Delta t = 1.1$ cm, slightly less than the diameter of the smallest particles (1.27 cm). We then spatially bin the data with a resolution $\Delta w = 1.6$ cm, which is the mean diameter of the two particle species in the bidisperse sample. Within each bin, we find the mean displacement vector, averaging over all particles and all times. To compute this average, we also exploit the symmetry of the back-and-forth motion in the “L” (Fig. 3.3), and thus reorient the data so that the active plunger is always at the lower right corner. The result is the vector field $\Delta \vec{r}_{\text{mean}}(x, y)$ shown in Fig. 3.5. We see plug-like flow on the lower right inlet, corresponding to the active plunger, which

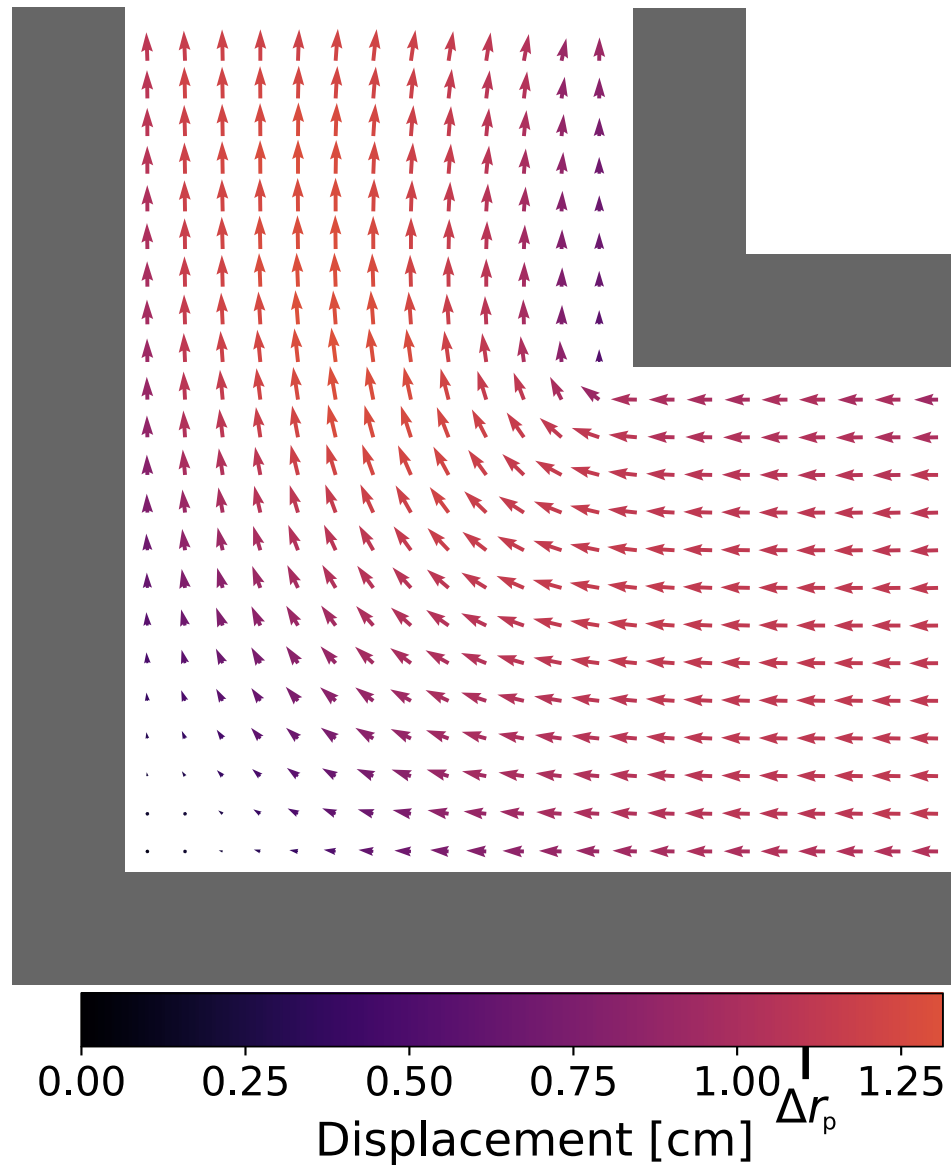


Figure 3.5: Mean displacement field $\Delta \vec{r}_{\text{mean}}(x, y)$. The displacements are calculated using $\Delta t = 5\text{s}$. The bold line on the scale bar indicates $\Delta r_p = v_p \Delta t = 1.1\text{cm}$, the displacement corresponding to the plunger motion over Δt . On the lower right inlet, we observe a plug like flow closer to the plunger, which then turns into a more shear like flow as the particles turn the corner. Closer to the lower left corner we see an area with almost no displacements, signified by the shorter arrows with the darker color.

enforces that all particles contacting it move with the plunger velocity V_p . In the corner region of the “L” particles change the direction of their motion. The particles in the lower left corner barely move on average, whereas the particles in the middle of the corner region move significantly, resulting in a velocity gradient. In the upper outlet region, the motion of the particles is slightly slower near the sidewalls. To conserve particle flux, this means that particles near the center of the outlet region are moving slightly faster than the plunger speed.

Note that Fig. 3.5 is averaged over all particle size distributions. We separately compute the mean flow field for each particle size distribution and find that the different flow fields are nearly the same within the noise, with no systematic variation. Accordingly, to reduce the noise, we consider $\Delta\vec{r}_{\text{mean}}(x, y)$ as a useful reference mean flow for all experiments.

3.3.2 Non affine displacement and local particle rearrangement

Of course, the flow field shown in Fig. 3.5 is averaged over all particles and all times; at any specific moment, individual particles are often found moving in different directions, and it is only their average which is a smooth function of space. As an example, we can look at Figs. 3.6(a,b) which show the displacement of particles for two different distributions, bidisperse and T4, for a single frame. The T4 distribution is constructed by adding five large particles to the bidisperse distribution, where the large particles are five times larger than the smallest particles. In Figs. 3.6(a,b), the length of the arrow and also the color of the particle signify the magnitude of the displacement, with darker colors for larger displacements.

Starting with the displacement of bidisperse case shown in Fig. 3.6(a), we observe many of the characteristics highlighted in Fig. 3.5. These characteristics include plug-like flow near the plunger inlet and shear-like flow on the outlet side. Of course,

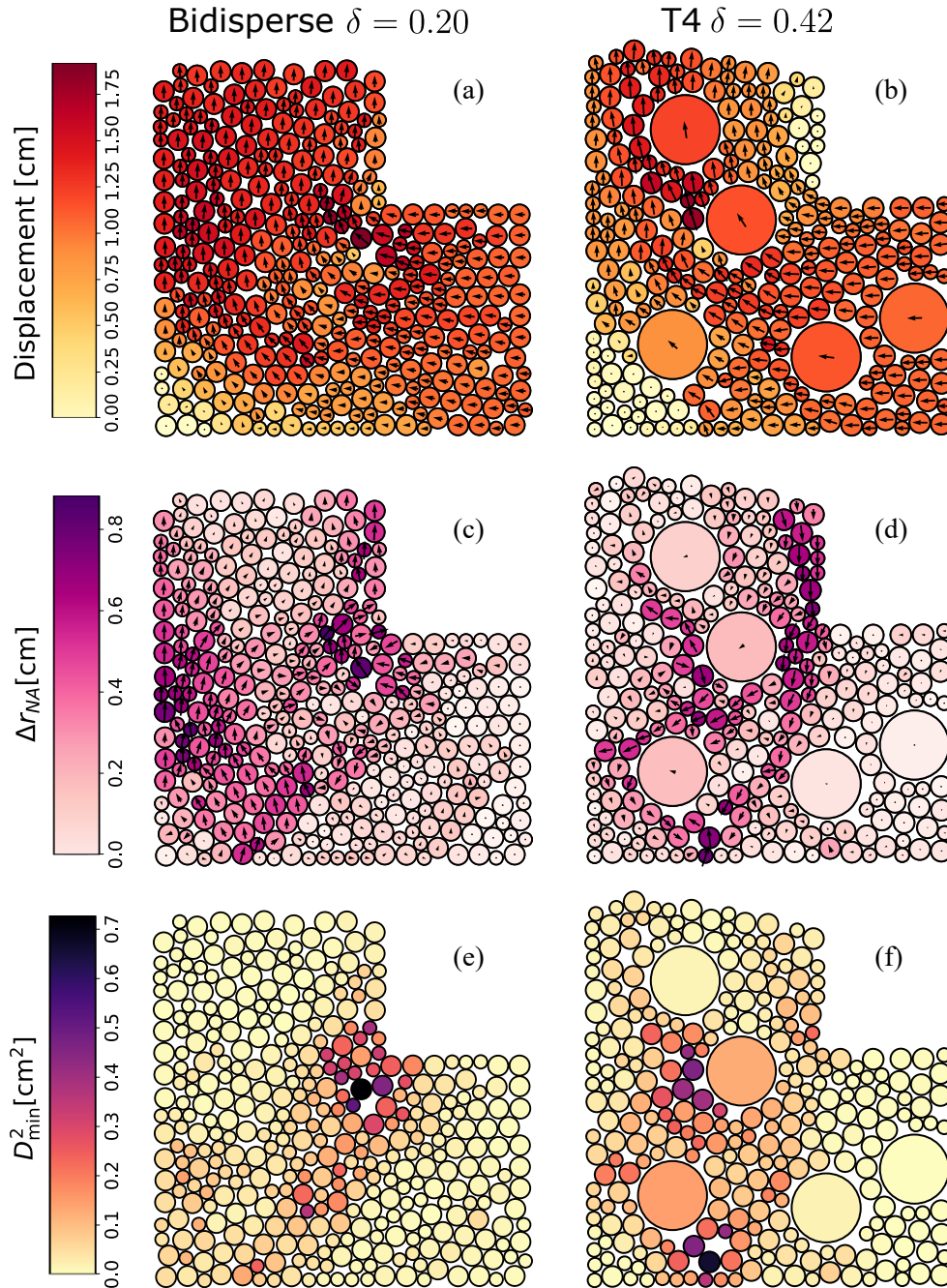


Figure 3.6: Snapshots showing the different quantities measured in the flow for the bidisperse size distribution (left column panels) and the T4 size distribution (right panels). From top to bottom, (a,b) display the displacement of each particle, (c,d) show the nonaffine displacement, and (e,f) show D_{\min}^2 for each disk. The plunger at lower right enforces that contacting particles move with velocity v_p , and thus have displacements $\Delta r_p = 1.1$ cm. For the bidisperse distribution, regions of higher nonaffine motion (Δr_{NA} or D_{\min}^2) are typically associated with locations of higher strain. For the tridisperse distribution, the largest particles generally have less nonaffine motion, but nearby smaller particles often have more nonaffine motion. For both distributions, the flow near the moving plunger (lower right) is plug flow: thus no shearing and no nonaffine motion.

Fig. 3.5 shows the mean displacement field $\Delta r_{\text{mean}}(x, y)$ which is an average over data such as Fig. 3.6(a). At the specific time shown in the latter, the lower left corner has very small displacements, with some particles at the corner being completely still. There are also a few particles with displacements larger than that of the plunger, $\Delta r_p = 1.1$ cm. Another interesting feature is the difference in displacements between neighboring particles: in contrast to Fig. 3.5 where the colors change smoothly as a function of space, for the discrete particles there are instances in Fig. 3.6(a,b) where a region has a mixture of colors.

To quantify these behaviors of individual particles at individual moments in time, we consider nonaffine displacements of the particles, $\vec{\Delta}r_{\text{NA}}$. An affine or linear displacement is defined by a linear mapping that preserves points, straight lines, and planes. For the motion of particles an affine displacement is generally described by:

$$\begin{bmatrix} \Delta x \\ \Delta y \end{bmatrix} = \mathbf{A} \begin{bmatrix} x \\ y \end{bmatrix} + \mathbf{b}. \quad (3.2)$$

Where \mathbf{A} is a constant matrix and \mathbf{b} is a constant vector. The displacements described by Eq. 3.2 include describes many kinds of transformations such as translations and rotations, but can also describe dilatation and shearing[146]. Non-affine displacements are then transformations which are not lineal, are often associated with plastic deformations in a material, and are often used to characterize plastic deformations in materials and granular flows[28, 32, 144].

As stated before, to analyze the motion of our particles, we will study the non-affine component of motion, by subtracting off the mean displacement(affine) over a Δt . We will refer to this quantity as Δr_{NA} , the non-affine displacement, and for the mean displacement , we will use the previously calculated mean displacement field. More specifically, we use the following formula to calculate the non-affine displacement of a single particle i at a time t :

$$\Delta\vec{r}_{i\text{NA}}(t) = \Delta\vec{r}_i(t) - \Delta\vec{r}_{\text{mean}}(x, y), \quad (3.3)$$

where $\Delta\vec{r}_i(t)$ is the displacement for the particle i at time t and $\Delta\vec{r}_{\text{mean}}(x, y)$ is the mean displacement at the corresponding to particle's i initial position (x, y) , as shown in Fig. 3.5. The non-affine displacement, Δr_{NA} helps us better understand the effect on the flow of particles caused by local rearrangements, compared to the mean background displacement, and has been used multiple time to characterize amorphous materials and systems with defects [32, 112, 144, 147–151].

Figures 3.6(c,d) show a vector map for the nonaffine displacements for the data corresponding to panels (a,b). As we did for Figs. 3.6(a,b), the arrows are the non-affine displacements, and darker particle colors indicate a larger magnitude of Δr_{NA} . We see that most particles with high nonaffine displacements occur closer to the central area and close to the walls in the upper section. In the bidisperse flow this occurs due to the rearrangement of particles as the flow changes from plug-like flow to shear-like, and the particles need to navigate the turn around the corner. For the more polydisperse sample, this behavior is still present. However, the flow is also disrupted by the larger particles. This is seen as most instances of nonaffine motion now occur around the larger particles, other than the lower right region where there is plug-like flow. Another interesting note is that while large particles cause a disruption in the surrounding flow, these large particles themselves have small Δr_{NA} values compared to their neighbors.

A simple way to explain this behavior is to picture a large particle as it moves around the corner. The mean flow is shown in Fig. 3.5, and for a sufficiently large particle near the top right corner, it would exist in regions where the mean flow changes both in magnitude and direction. Given that the large particle feels forces from a variety of adjacent smaller particles, it makes sense that the large particle will, on average, still follow the mean flow expected for the large particle's center.

However, any nearby smaller particles will try to move according to the local flow field they experience. If a smaller particle is close to the larger particle but in a normally faster section of the flow field, the smaller particle will need to move around the larger particle. In contrast, a small particle in a slower local flow will be pushed out of the way by the larger particle [32].

Of course, it is possible that large particles could locally induce a smooth flow of themselves and their neighboring particles. To look for this, we consider an alternate definition of nonaffine motion introduced by Falk and Langer in 1998 [28] and widely used since then [112, 118, 121, 152, 153].

The key idea is to examine a local group of particles and fit their displacements to a strain tensor using a least-squares fit. The least squares fit error, D_{\min}^2 , then quantifies the extent to which that local group of particles is *not* well described by a simple strain tensor, and thus serves as a measure of the nonaffine motion of that group of particles. To compute this quantity, we select a particle $n = 0$ and a set of its nearest neighbors and fit the displacements of all of these particles at a specific time t to a local strain tensor ϵ_{ij} . The fitting is least squares where we find ϵ_{ij} to minimize the quantity

$$D^2(t, \Delta t) = \sum_n \sum_i \left\{ r_n^i(t) - r_0^i(t) - \sum_j (\delta_{ij} + \epsilon_{ij}) \right. \\ \left. \times [r_n^j(t - \Delta t) - r_0^j(t - \Delta t)] \right\}^2, \quad (3.4)$$

where n indexes the neighbors of the reference particle with the index $n = 0$. The indices i, j refer to the spatial coordinate components, $\epsilon_{i,j}$ is the best least-squares fit strain matrix characterizing the region, and δ_{ij} is the Kronecker delta. The residual error after least squares fitting, D_{\min}^2 , is our measure of local nonaffine motion [28]. Here, rather than defining the affine flow through the space- and time-averaged flow, the affine flow is determined locally in space and time.

For random packing of highly polydisperse particles D_{\min}^2 is strongly dependent on the number of nearest neighbors included in the sum over n in Eq. 3.4: more neighbors allow for more deviations from the mean strain matrix, increasing D_{\min}^2 [32]. Following prior work by Jiang *et al.* [32], we use the $N_{\text{nbs}} = 15$ closest particles as the nearest neighbors, defining the distance between particles as surface-to-surface:

$$d_{0n} = |\vec{r}_n - \vec{r}_0| - R_n - R_0 \quad (3.5)$$

where, as before, \vec{r}_0 is the position of the reference particle, \vec{r}_n the position of neighbor n , and R_0 and R_n their respective radii. Using Eq. 3.5, particles in contact are at distance $d_{0n} = 0$ cm. This definition allows us to fairly compare the D_{\min}^2 of particles of different sizes and across multiple size distributions.

Using $N_{\text{nbs}} = 15$ results in 2 layers of neighbors for the smallest particles, and a single full layer for the largest particles. Other methods were used to define the local interaction range, including only the first neighbors, first and second neighbors, and first Voronoi layer particles. However for these methods N_{nbs} has a strong dependence on particle size. Alternatively, for the fixed N_{nbs} method, we tried different N_{nbs} values, such as $N_{\text{nbs}} = 11$ and $N_{\text{nbs}} = 20$, which return similar results. In Fig. 3.7 we show an example of the 15 closest neighbors for both the smallest and largest particles.

When compared to the non-affine displacement defined in Eq. 3.3, D_{\min}^2 is calculated based on the displacement of a reference particle's neighboring particles, and does not refer to the mean displacement field at all. Similarly to the non-affine displacements, D_{\min}^2 has been used several times to characterize the deformations and distortions in amorphous materials and granular flows[28, 118, 144, 152].

Figures 3.6(e,f) show the particles shaded according to their value of D_{\min}^2 , where darker colors indicate higher values. A similar behavior to Figs. 3.6(c,d) is observed

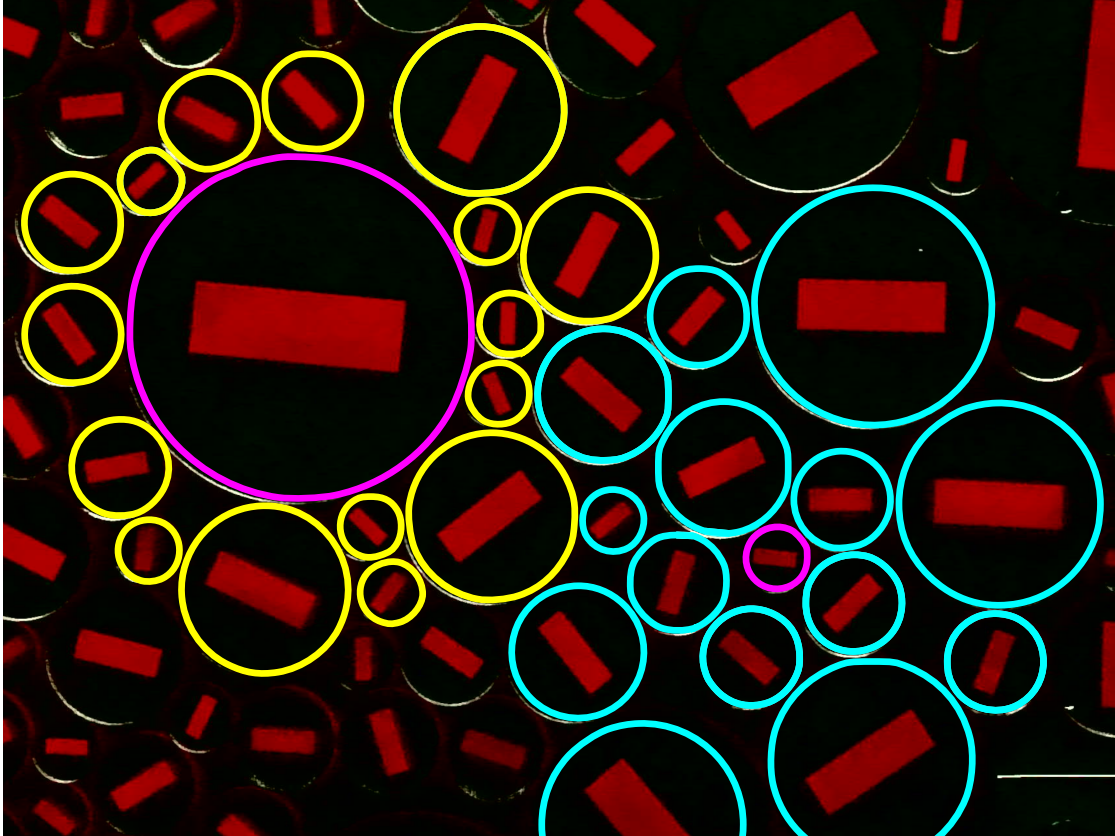


Figure 3.7: Two examples of our neighbor definition. We use the closest 15 particles as neighbors of the reference particle. Magenta indicates the reference particle. Yellow indicates the neighbors of our largest particle, R_8 , on the left. The cyan particles show the neighbors for the smallest particle, R_0 , on the right.

for D_{\min}^2 . For the bidisperse case [Fig. 3.6(e)] the highest values for D_{\min}^2 occur close to the upper right corner where particles navigate the turn. The region with the second highest levels of D_{\min}^2 is in the central zone. In Fig. 3.6(f), corresponding to the T4 case, the larger particles are again seen to have an effect on the flow. Here, the particles with the largest D_{\min}^2 are small particles that are close to large particles, showing that large particles disrupt the displacements of their neighbors. The proximity to the upper right corner appears less relevant. The large particles, while enhancing the D_{\min}^2 of their neighbors, have a lower D_{\min}^2 value themselves.

As mentioned above, a high amount of the phenomena related to particle rearrangement and non affine motion happens in the central area, therefore, we will define our central region as the area covered by a 23.7 cm square, matching the lower left corners of this square and the experimental device. An illustration of this square region is shown in Fig 3.2(b).

Our goal is to understand the role of particle size, and Figs. 3.6 (d,f) suggest that larger particles have less nonaffine motion. We know that the flow pattern is spatially heterogeneous, as will be discussed in more detail in Sec. 3.3.4. Nevertheless, we wish to find the average nonaffine motion as a function of particle size. To do this, we pick a particle radius from a given experimental condition. We calculate the values of $\Delta r_{\text{NA}}/\langle R \rangle$ and $D_{\min}^2/\langle R \rangle^2$ for all particles of that size and all times. We then find the mean values of these as a function of (x, y) , similar to how we find the flow field $\Delta \vec{r}_{\text{mean}}(x, y)$. Finally, we average the resulting fields over (x, y) . We do this for all particle radii and all particle size distributions, with the results shown in Fig. 3.8. The one exception to this procedure is for the three largest particle sizes in the C3 particle size distribution, for which their small numbers do not give us adequate statistics. Accordingly, we average the observations of these three particle sizes together to calculate the nonaffine motion as a function of (x, y) , and then plot the (x, y) averaged results at the mean radius of the three particle sizes. Figure 3.8

shows that the smaller particles have higher values of Δr_{NA} and D_{min}^2 , whereas the larger particles have smaller values. This points to the previously given explanation, where large particles move according to the average displacement field to which they are subjected but cause other particles either to have to detour around them or be bumped out of the way.

To study how large particles affect the motions of their neighbors, we measure the mean values of Δr_{NA} and D_{min}^2 conditioned on the distance a particle has from a particle of a specific size. These results are plotted as a function of the edge to edge distance d_{ij} in Fig. 3.9. Figures 3.9(a,b) show the results for the bidisperse distribution. There is a minimum at contact between the particles, followed by a peak, and then a valley at $d_{ij} = 2R_0$. These oscillations are more pronounced for the neighbors of particles with radius R_1 , the larger of the two species in the bidisperse distribution [the top red curves in panels (a,b)]. Similar trends are stronger for the tridisperse distribution T4, shown in Fig. 3.9(c,d). Here, the largest particles (size R_8) strongly increase the nonaffine motion of their neighbors [the top blue curves in panels (c,d)]. These results confirm the conceptual picture sketched above that the large particles act as obstacles moving with the “wrong” velocity for some of their neighbors, forcing those neighbors to move nonaffinely. For larger separations d_{ij} , the measures level out towards the average (albeit with noise). The “signal” of the perturbation appears to be short-ranged and is within the noise for $d_{ij} \gtrsim 3$ cm, a distance equal to $2.4R_0 = 1.6R_1$ in terms of the two smallest particle sizes. This short-ranged influence is comparable to that seen in a prior experiment which studied the oscillatory shear of emulsions [144], although simulations of a 2D emulsion model found longer range influences out to approximately 5 particle diameters [32].

The heights of the first peak in Figs. 3.9 are a good measure of the effect a particle has on the flow of its neighbors. We can then characterize this disturbance of flow caused by particles of size R by calculating the difference in value between these

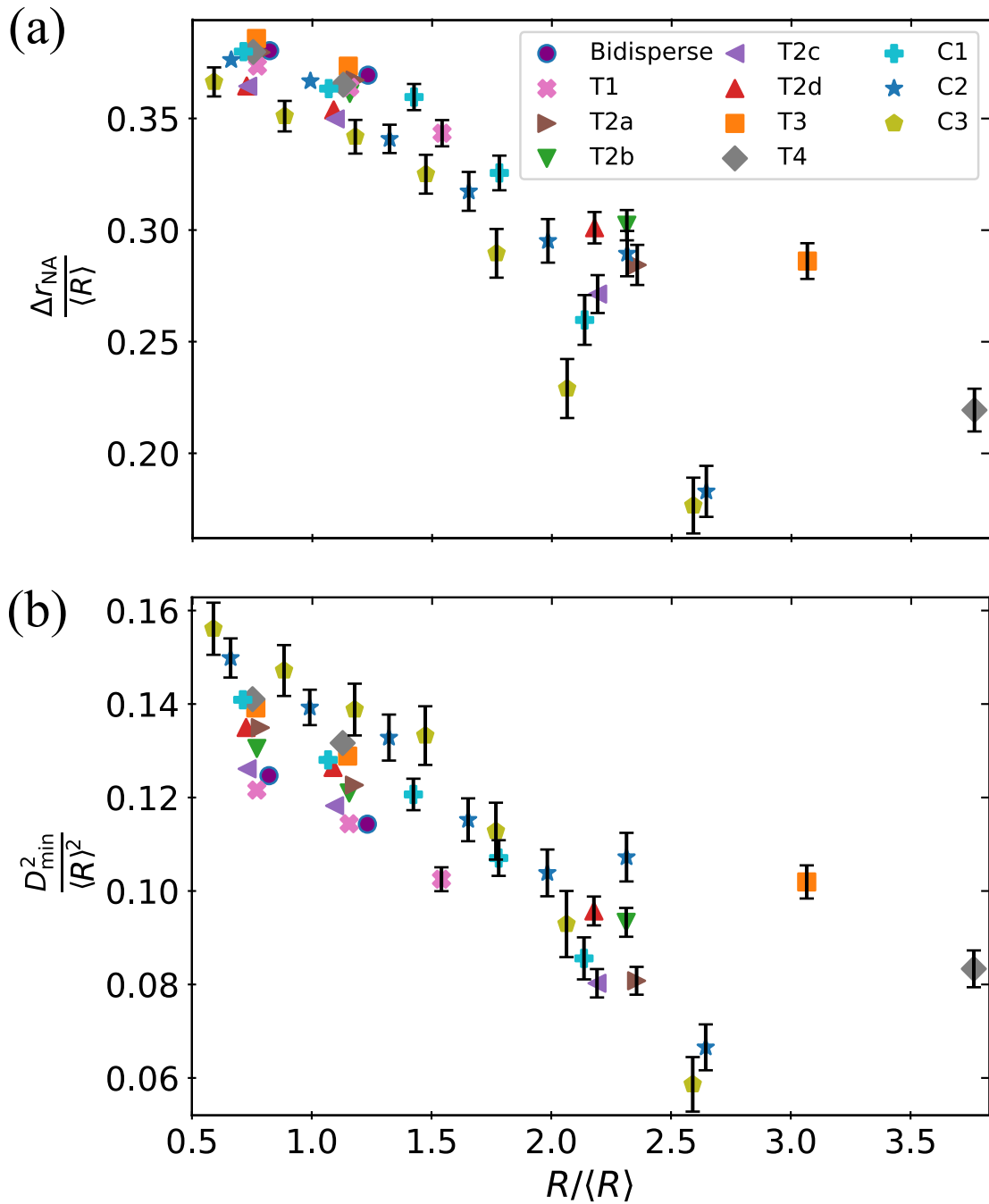


Figure 3.8: (a) The mean magnitude of the nonaffine motion $|\Delta r_{\text{NA}}|/\langle R \rangle$ and (b) $D_{\text{min}}^2/\langle R \rangle^2$, both as a function of the normalized particle size $R/\langle R \rangle$. Smaller particles have higher $|\Delta r_{\text{NA}}|$ and D_{min}^2 than larger particles. This is because larger particles are more likely to follow the mean flow, which forces smaller particles to maneuver around these large particles. To have enough data for a meaningful result, we average the observations of the three largest particles in C3 together.

peaks and the average Δr_{NA} and D_{min}^2 , for each particle size R , and for every size distribution. Here we will nondimensionalize all lengths by the mean radius $\langle R \rangle$ for the relevant particle size distribution. Figure 3.10 shows the normalized differences in peaks for (a) Δr_{NA} and (b) D_{min}^2 as a function of size R , and with the different symbols corresponding to the different size distributions studied. As hinted both by Figs. 3.6 and Figs. 3.9, the larger a particle, the larger the effect it will have on its neighbors, clearly shown in the growth of Δr_{NA} and D_{min}^2 for larger $R/\langle R \rangle$. The imperfect data collapse suggests there may be influences of the particle size distribution, although there is no clear trend.

The data shown in Figs. 3.8 and 3.10 show opposite trends as a function of R , and these opposite trends emphasize our conceptual story. Larger particles are subjected to the mean flow of all of their surrounding neighbors, resulting in less nonaffine motion, confirmed in Fig. 3.8. These larger particles thus disrupt the flow of their neighboring smaller particles, forcing these smaller particles in a competition between following the mean flow and following the motion of their larger neighbor. Thus, the larger particles cause more nonaffine motion for their neighbors, confirmed in Fig. 3.10. These results agree with prior observations of softer particles [32, 144].

This chapter focuses on the larger particles and it is plausible that the larger those particles are, the more strongly the overall particle motion is affected. We test this conjecture by calculating the mean values of the spatial averaging of Δr_{NA} and D_{min}^2 for all particles as a function of the polydispersity δ of the corresponding size distribution, plotted in Fig. 3.11. Surprisingly, $\Delta r_{\text{NA}}/\langle R \rangle$ is not affected by changes in polydispersity. The values for the distributions studied average to $\langle \Delta r_{\text{NA}}/\langle R \rangle \rangle = 0.37 \pm 0.01$. Comparing this to the data shown in Fig. 3.8, it appears that the smaller nonaffine motion for the few larger particles is balanced by the increased nonaffine motion of the more numerous smaller particles. On the other hand, Fig. 3.11(b) shows

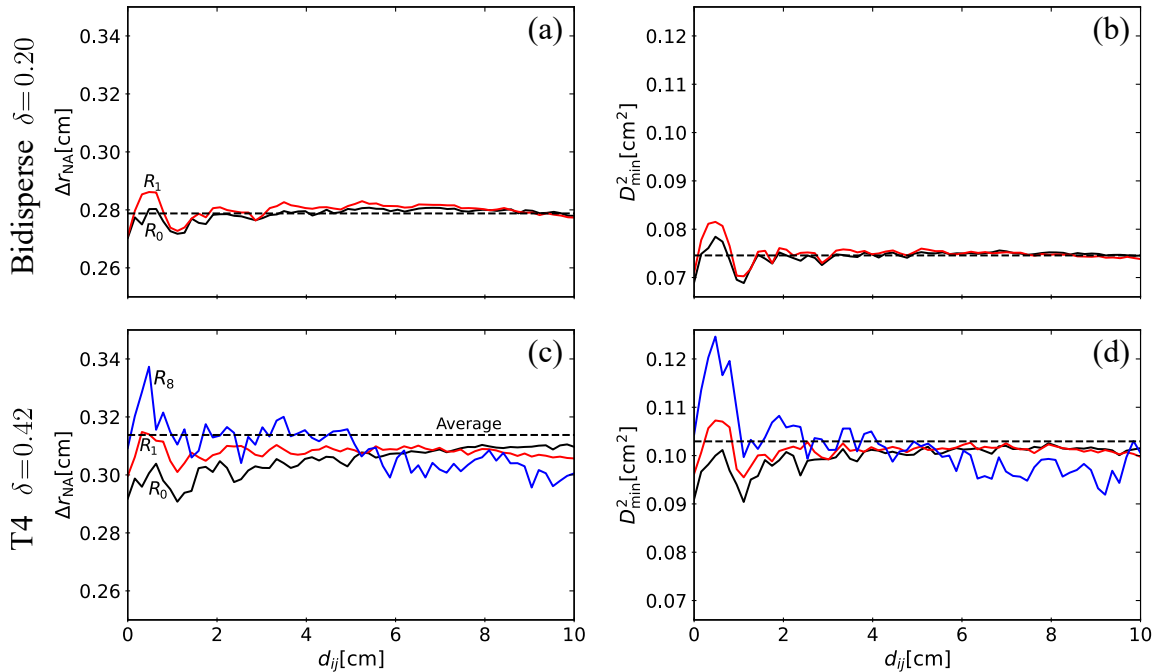


Figure 3.9: Δr_{NA} is shown in (a,c) and D_{min}^2 in (b,d), both as a function of distance (d_{0i}) from the edge of a reference particle with radius R to all other particles. The top panels (a,b) correspond to the bidisperse distribution, and the bottom panels (c,d) to the T4 distribution. At $d_{0i} = 0$, there's a valley for all cases, corresponding to particles in direct contact to the reference, resulting in low Δr_{NA} and D_{min}^2 , due to the tight packing. There's a another valley at $d_{0i} = 2R_0$, which in this case corresponds to a buffer of one R_0 between the particles, but are otherwise in close packing, causing the minimum. In between these valleys we find a peak at $d_{ij} \sim 0.75$ cm. These peaks are a good tool to measure the effect the reference particle has on its closest neighbors. This measurement is affected by particle size, an effect that can be seen for all distributions shown here, with larger particles having higher peaks. This can be seen by the differently colored curves. As shown in the legend, the blue curve correspond to the R_8 particles, while red and black to R_0 and R_1 , respectively. The dashed line shows the average value for all particles.

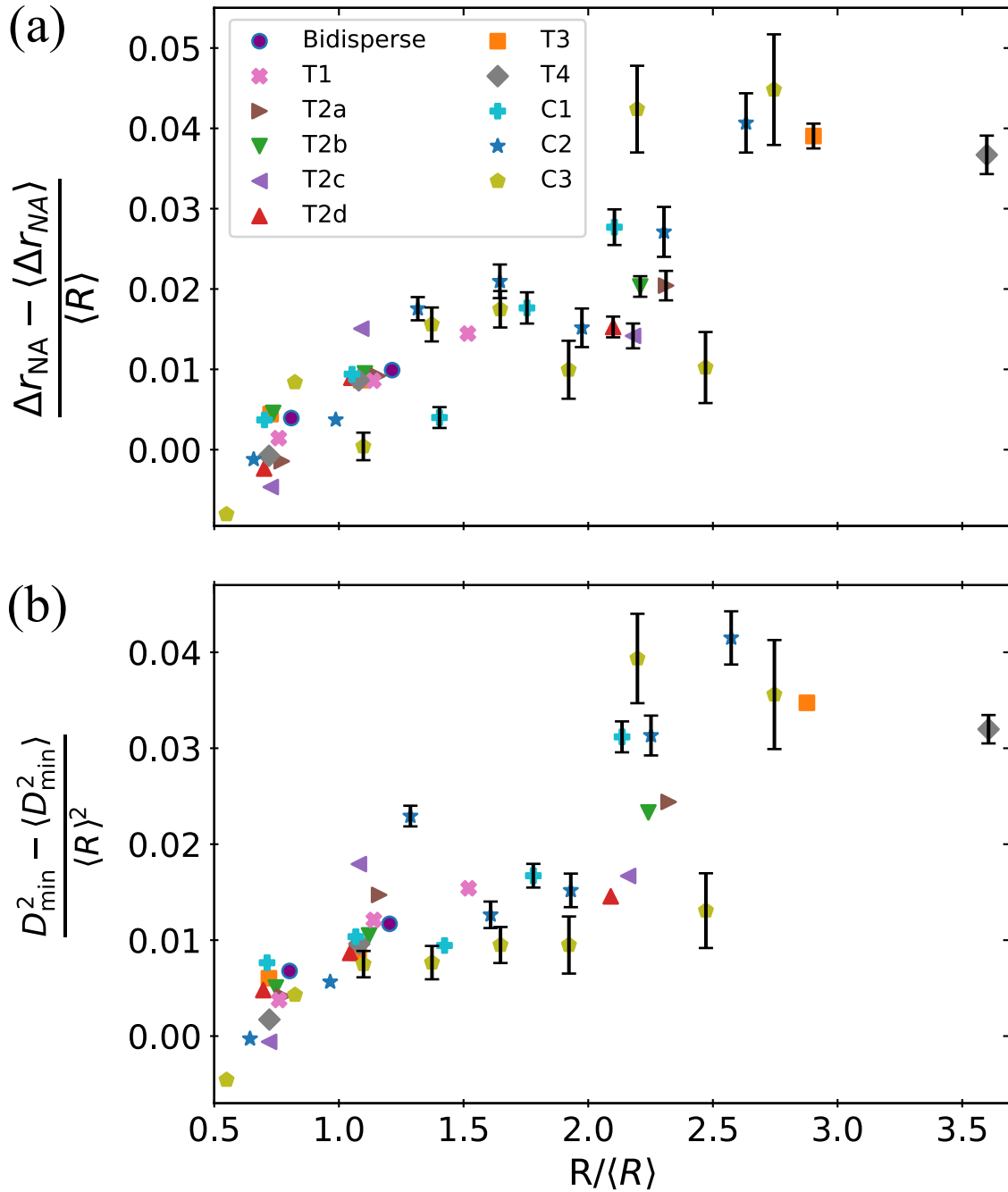


Figure 3.10: These graphs show how particles of size $R/\langle R \rangle$ influence the motion of their neighbors. (a) Peak $(\Delta r_{NA} - \langle \Delta r_{NA} \rangle)/\langle R \rangle$. (b) Peak $(D_{\min}^2 - \langle D_{\min}^2 \rangle)/\langle R \rangle^2$. The symbols correspond to distinct particle size distributions, given by the legend in (a). The peak height is measured from data similar to that shown in Fig. 3.9, where the peak is measured for $d_{0j} < 2R_0$ from the reference particle. Larger particles have stronger influences on their neighbors. Error bars are only shown when the error bar is larger than the scatter symbol.

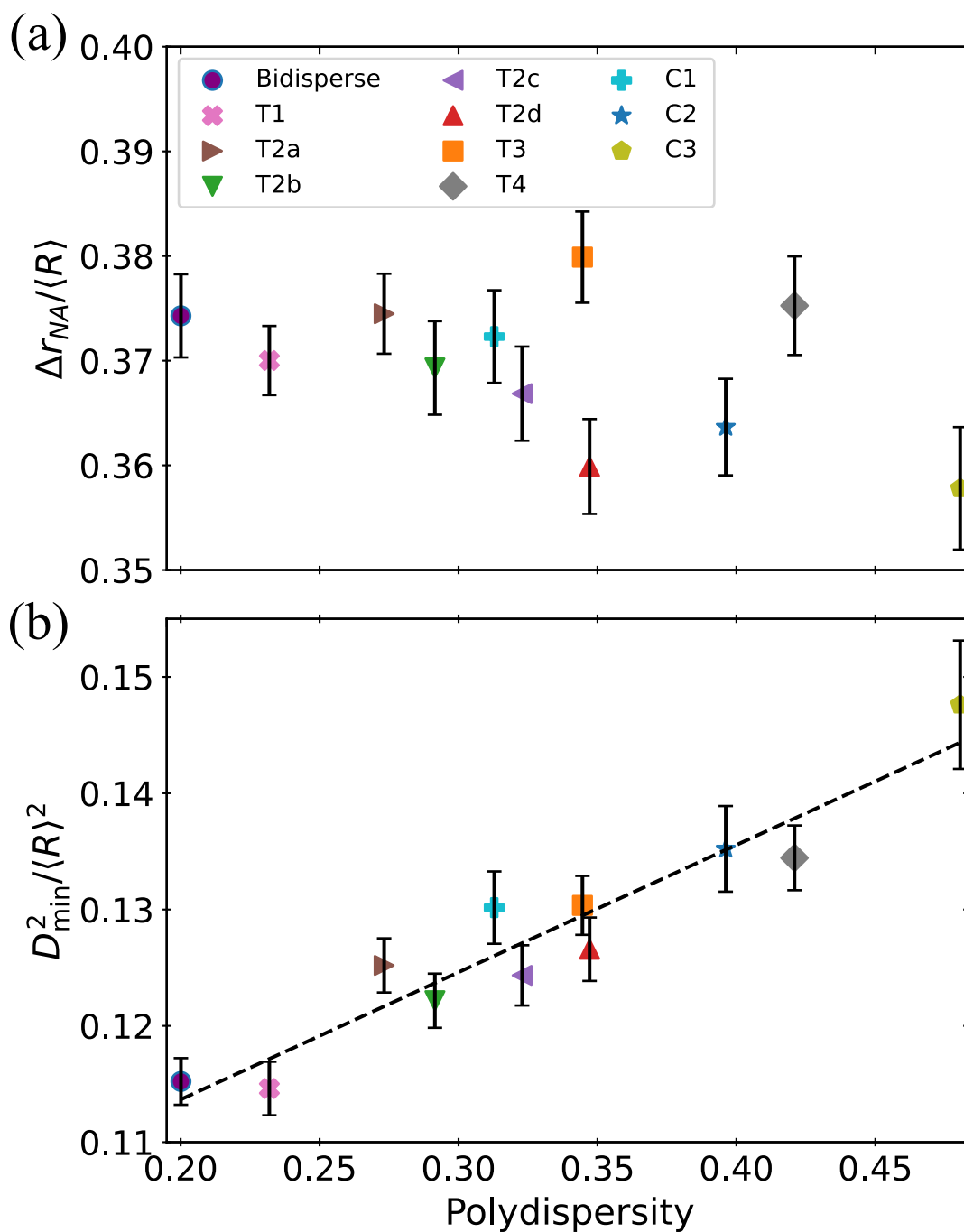


Figure 3.11: (a) $\Delta r_{\text{NA}}/\langle R \rangle$, and (b) $D_{\text{min}}^2/\langle R \rangle^2$, as a function of the polydispersity for each size distribution. For $\Delta r_{\text{NA}}/\langle R \rangle$, we see no relation to polydispersity, averaging to a value of 0.37. On the other hand $D_{\text{min}}^2/\langle R \rangle^2$ shows a positive relation with polydispersity. The dashed line is a least-squares fit to the data; see text for details.

that $D_{\min}^2/\langle R \rangle^2$ has a positive relation with polydispersity. We fit the data using

$$D_{\min}^2/\langle R \rangle^2 = m\delta + b \quad (3.6)$$

with slope $m = 0.11$ and intercept $b = 0.09$. We note that this behavior is affected primarily by the polydispersity of a size distribution and not the size ratio itself, as evidenced by T2 family of distributions. All T2 distributions have the same size ratio but their $\langle D_{\min}^2 \rangle / \langle R \rangle^2$ values correlate mainly to their polydispersity. Conversely, two distributions with similar polydispersity but different size ratios R_{\max}/R_{\min} , T3 and T2d, have similar values of $\langle D_{\min}^2 \rangle / \langle R \rangle^2$.

3.3.3 Time scale dependence

All of the results above have used a set time scale $\Delta t_0 = 5$ s for calculating displacements. To briefly investigate the influence of this choice, we study how the results of Fig. 3.11 depend on Δt . We compute the average values for $\Delta r_{\text{NA}}/\langle R \rangle$ and $D_{\min}^2/\langle R \rangle^2$ for different $\Delta t/\Delta t_0$. Here, to enhance the signal, we take the averages only over particles in the central region of the channel (the square region between the inner and outer corners of Fig. 3.5). The data are plotted in Fig. 3.12 for all time intervals. All size distributions show a similar growth in values for increasing time intervals. The data in Fig. 3.12(a) for $\Delta r_{\text{NA}}/\langle R \rangle$ nearly superimpose on each other, which is expected as seen in Fig. 3.11(a): this measure of nonaffine motion is not sensitive to polydispersity, and this fact holds true for all Δt . On the other hand, in Fig. 3.12(b) the $D_{\min}^2/\langle R \rangle^2$ are slightly separated by polydispersity, in agreement with Fig. 3.11(b). The differences with polydispersity are more apparent in Fig. 3.11(b); the logarithmic axis of Fig. 3.12(b) reduces the distance between the curves.

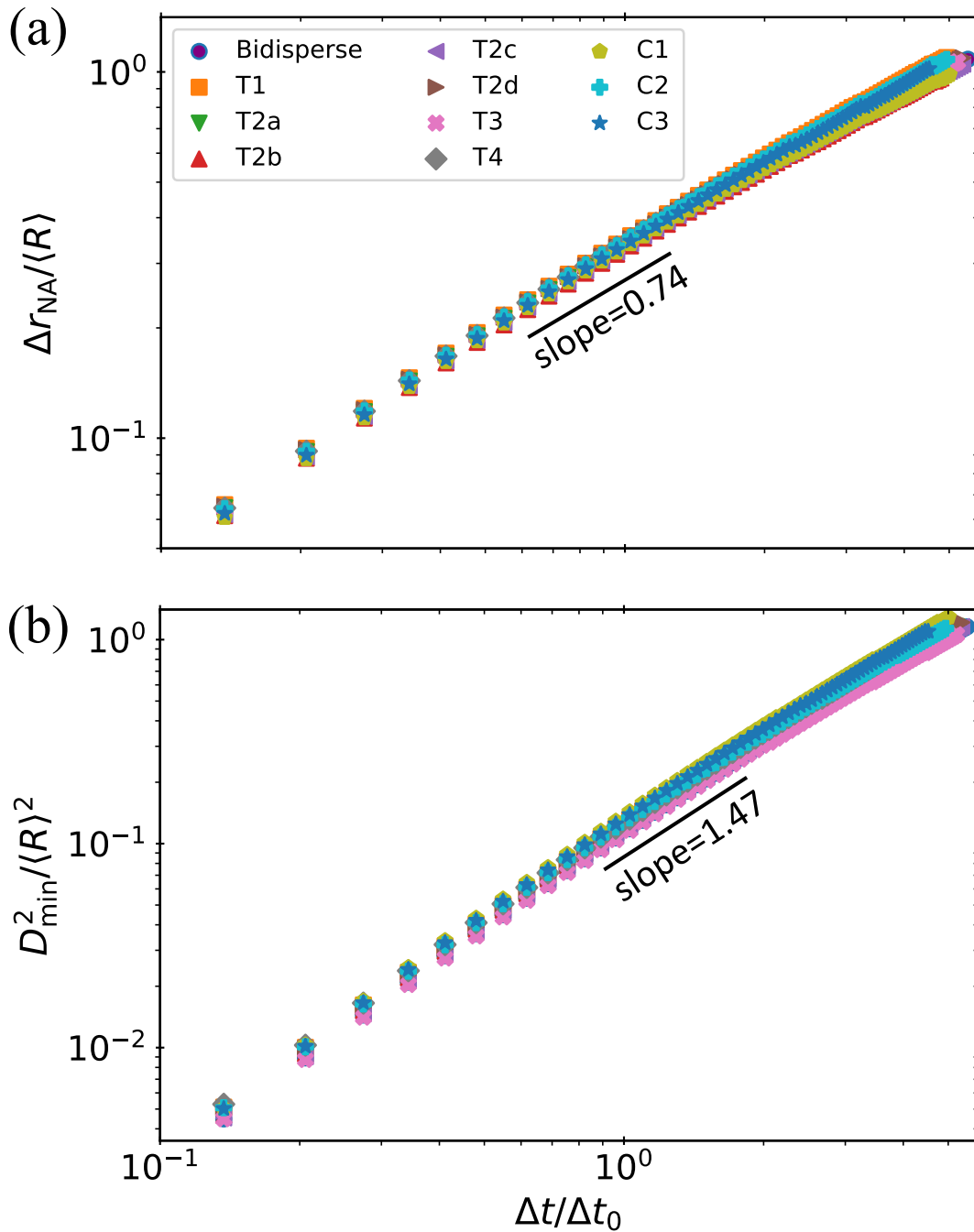


Figure 3.12: Average $\Delta r_{\text{NA}}/\langle R \rangle$, Fig.(a), and $D_{\text{min}}^2/\langle R \rangle^2$, panel Fig.(b), for the central zone for various time intervals, on log-log scale, for all size distributions. The lines indicate power-law scaling with exponents as labeled. All distributions share similar exponents and their corresponding curves do not cross each other for the observed Δt .

The time scale dependence of the nonaffine motion is well fit by power laws:

$$\Delta r_{\text{NA}}/\langle R \rangle \sim \left(\frac{\Delta t}{\Delta t_0} \right)^{\alpha_1} \quad (3.7)$$

$$D_{\text{min}}^2/\langle R \rangle^2 \sim \left(\frac{\Delta t}{\Delta t_0} \right)^{\alpha_2} \quad (3.8)$$

with $\alpha_1 = 0.74$ and $\alpha_2 = 1.47$. Given that Δr_{NA} has units of length and D_{min}^2 units of length squared, it is reasonable that $\alpha_2 \approx 2\alpha_1$. Given that these power laws well-describe the data for each individual particle size distribution, we conclude that our observations of the character of the nonaffine motion are fairly robust over time scales Δt up to the duration of our experiments.

In the following section we will study the stress field and shearing rates throughout the canal in an effort to better account for the spatial heterogeneity of the flow configuration.

3.3.4 Strain clock

For the bidisperse sample, we have noted throughout the previous subsection that there is more nonaffine motion near the top right corner, where there is more shearing. Given that the strain rate is not spatially homogeneous, one can conjecture that the data are confounded by the specific locations of the particles. To quantify this, we need to define a local strain rate. We can then compare the data which uses the fixed time interval $\Delta t_0 = 5$ s to define displacements and the data calculated using a fixed strain increment. We will first consider our fixed Δt_0 and examine the local strain rate.

The starting point is the mean displacement field $\Delta \vec{r}_{\text{mean}}(x, y, \Delta t)$ where now we explicitly include the Δt dependence. We then use the following equation to calculate the strain tensor:

$$DF_{i,j}(x, y, \Delta t) = \frac{\partial \Delta r_i(\Delta t)}{\partial r_j} \quad (3.9)$$

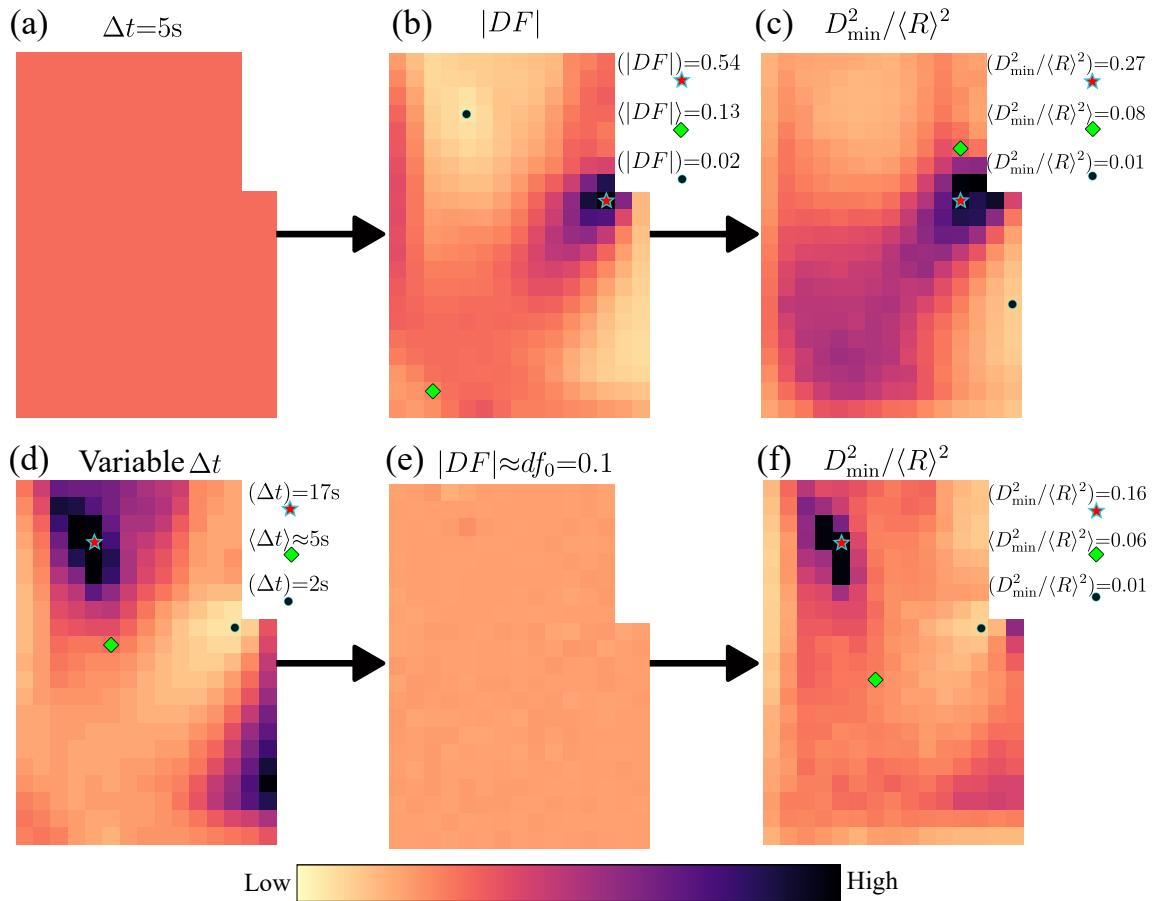


Figure 3.13: Color maps for $\Delta t = 5$ s, Fig.(a), $|DF(\Delta t = 5 \text{ cm})|$, Fig.(b) and $|D_{\min}^2(\Delta t = 5 \text{ cm})|$ on the top row. On the bottom row we show the quantities but with $\Delta t(x, y)$, Fig.(d), such that $|DF(\Delta t(x, y))| \approx df_0$, Fig (e). The final color map, Fig.(f) corresponds to $D_{\min}^2(\Delta t(x, y))$. We see at the top row that D_{\min}^2 is strongly correlated to $|DF(\Delta t = 5 \text{ s})|$, while in the case for $\Delta t(x, y)$, the time interval matrix correlates strongly to $D_{\min}^2(\Delta t(x, y))$. In this last case we manage to obtain a somewhat more spatially homogeneous matrix closer to the center areas.

where i, j are the spatial coordinate indices and $\Delta r_i(\Delta t)$ is the displacement in the i coordinate for a time step Δt . This tensor contains information on the strain of the flow of the particles and is the non-symmetric version of the Cauchy strain tensor. To measure the total strain at a given position, we calculate the Frobenius norm of the strain tensor:

$$|DF(x, y, \Delta t)| = \sqrt{\sum_{i,j} \left(\frac{\partial \Delta x_i(\Delta t)}{\partial x_j} \right)^2}. \quad (3.10)$$

This then is a scalar which quantifies the amount of strain occurring over the time scale Δt at each location (x, y) .

Figure 3.13(a-c) shows the results for fixed Δt . Panel (a) shows Δt and is uniform, reflecting that Δt is constant. Panel (b) shows that there are regions of high strain, especially near the upper right corner. The lower right inlet region is not shown, as this region is mostly plug flow and uninteresting ($|DF| \approx 0$). Panel (c) then shows that for fixed Δt , indeed much of the nonaffine motion measured by $D_{\min}^2/\langle R \rangle^2$ is located in the regions with large $|DF|$. The diagonal from lower left corner to upper right corner has more strain: as shown in Fig. 3.5, the velocity is changing direction and magnitude in this diagonal region. Naturally, particles will be required to rearrange, and Fig. 3.13(c) confirms that $D_{\min}^2/\langle R \rangle^2$ is larger here.

To consider the case of constant strain interval rather than constant time interval, we return to the $|DF(x, y, \Delta t)|$ data. We then define $\Delta t(x, y)$ through $|DF(x, y, \Delta t)| = df_0 = 0.1$, where df_0 is a small strain. The choice of df_0 is somewhat arbitrary, but is chosen so that a good portion of $\Delta t(x, y)$ is a comparable order of magnitude to $\Delta t_0 = 5$ s. $\Delta t(x, y)$ is quantized by our imaging rate (6 images per second), so in practice we find the $\Delta t(x, y)$ that minimizes the difference between $|DF(x, y, \Delta t)|$ and df_0 . $\Delta t(x, y)$ is shown in Fig. 3.13(d), where a strong dependence on position is apparent. Near the bottom right where there is plug flow, and near the top left where there is also a small region of plug-like flow, Δt must be large to achieve any

significant local strain. By allowing Δt to depend on the position, we achieve our goal $|DF| \approx df_0$, as shown in panel (e), with residual noise due to the quantization of Δt .

Next, we calculate $\Delta \vec{r}_{NA}/\langle R \rangle$ and $D_{\min}^2/\langle R \rangle^2$ for all particles and use the entire range of time scales Δt . Finally, we examine $D_{\min}^2(x, y)/\langle R \rangle^2$ where at each (x, y) we use the data calculated with $\Delta t = \Delta t(x, y)$ to ensure the strain increment is df_0 . The results for $D_{\min}^2(x, y)/\langle R \rangle^2$ are shown in Fig. 3.13(f). The resulting D_{\min}^2 is a smoother function of (x, y) .

For much of the channel, this confirms that $D_{\min}^2/\langle R \rangle^2$ is to an extent determined by the amount of strain that occurs at a given position. The exception is the top left region, which has a patch where little strain occurs: the particles in this location tend to move in a group at constant velocity. This causes D_{\min}^2 to be larger nearby and within this group. To exclude this region from the subsequent analysis, we will restrict our attention to locations with $\Delta t \leq 17$ s. This excludes the plug-flow region at the bottom right inlet location, as well as the center of the dark patch in Fig. 3.13(d).

As just discussed, having $\Delta t(x, y)$ we can calculate $\Delta \vec{r}_{NA}/\langle R \rangle$ and $D_{\min}^2/\langle R \rangle^2$ for all particles based on a fixed strain increment df_0 . We then average over all particles within a given sample and plot these averages as a function of the polydispersity of the corresponding size distribution in Fig. 3.14. Similar to Fig. 3.11(a), $\Delta r_{NA}/\langle R \rangle$ is not dependent on polydispersity. Similar to Fig. 3.11(b), $D_{\min}^2/\langle R \rangle^2$ shows a positive relation with polydispersity. In this case we find $D_{\min}^2/\langle R \rangle^2 = m\delta + b$ with $m = 0.09$. The different value from the Fig. 3.11(b) result are because the magnitude of D_{\min}^2 depends strongly on the choice of Δt (or df_0), as shown in Fig. 3.12(b), so we do not expect a strict equivalence here. The point, instead, is that analyzing the data using a fixed strain increment leads to a similar result as the analysis with a fixed time increment and shows that the spatial heterogeneity of our flow is not a critical confounding factor.

For much of the channel, this confirms that $D_{\min}^2/\langle R \rangle^2$ is to an extent determined by the amount of strain that occurs at a given position. The exception is the top left region, which has a patch where little strain occurs: the particles in this location tend to move in a group at constant velocity. This causes D_{\min}^2 to be larger nearby and within this group. To exclude this region from the subsequent analysis, we will restrict our attention to locations with $\Delta t \leq 17$ s. This excludes the plug-flow region at the bottom right inlet location, as well as the center of the dark patch in Fig. 3.13(d).

As just discussed, having $\Delta t(x, y)$ we can calculate $\Delta \vec{r}_{NA}/\langle R \rangle$ and $D_{\min}^2/\langle R \rangle^2$ for all particles based on a fixed strain increment df_0 . We then average over all particles within a given sample and plot these averages as a function of the polydispersity of the corresponding size distribution in Fig. 3.14. Similar to Fig. 3.11(a), $\Delta r_{NA}/\langle R \rangle$ is not dependent on polydispersity. Similar to Fig. 3.11(b), $D_{\min}^2/\langle R \rangle^2$ shows a positive relation with polydispersity. In this case we find $D_{\min}^2/\langle R \rangle^2 = m\delta + b$ with $m = 0.09$. The different value from the Fig. 3.11(b) result are because the magnitude of D_{\min}^2 depends strongly on the choice of Δt (or df_0), as shown in Fig. 3.12(b), so we do not expect a strict equivalence here. The point, instead, is that analyzing the data using a fixed strain increment leads to a similar result as the analysis with a fixed time increment and shows that the spatial heterogeneity of our flow is not a critical confounding factor.

3.4 Conclusions

In this chapter we have explored how polydispersity affects nonaffine displacement and particle rearrangement in granular flows. Consistent with previous work that studied similar systems [32, 144], we find that large particles tend to move similarly to mean flow, as they average over the forces from the many discrete particles they are contacting. This then disrupts the flow of smaller neighboring particles, which

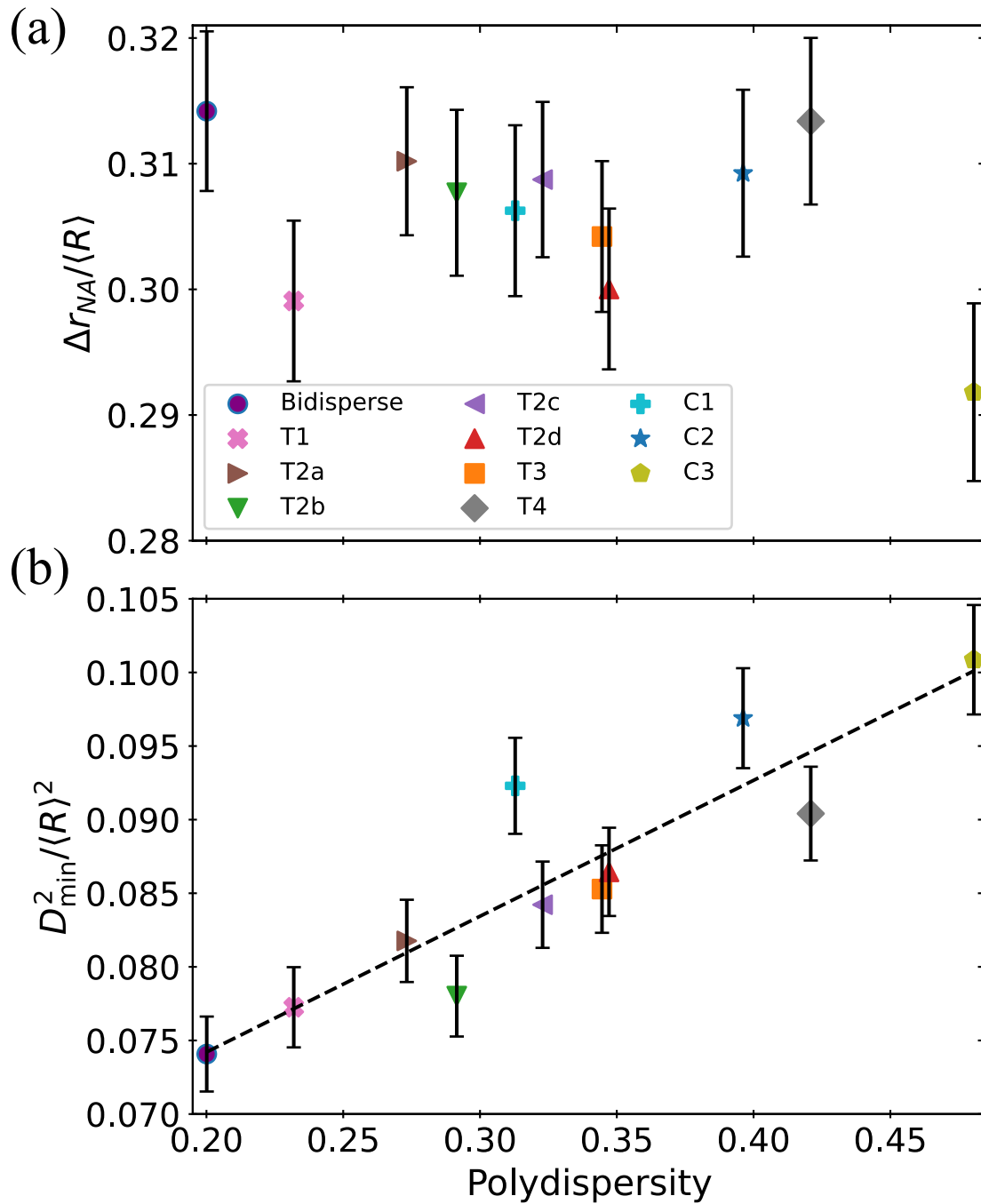


Figure 3.14: (a) $\Delta r_{NA}/\langle R \rangle$ and (b) $D_{\min}^2/\langle R \rangle^2$ as a function of polydispersity for all size distributions. In this figure $\Delta r_{NA}/\langle R \rangle$ and $D_{\min}^2/\langle R \rangle^2$ are calculated for each particle using $\Delta t(x, y)$. In contrast, Fig. 3.11 shows similar results using a fixed $\Delta t = 5$ s. The dashed line in (b) is a least-squares fit to the data; see text for details.

need to navigate around the larger particles, thus causing the smaller particles to move nonaffinely.

These observations are true even for the bidisperse case, highlighting that even when the two particle sizes are quite similar (size ratio 1 : 1.5 in our case), there is nonetheless a measurable difference in their nonaffine motion. Increasing the polydispersity of the particle size distribution quantitatively increases the observable effects. As polydispersity changes from 0.20 to 0.48, $D_{min}^2/\langle R \rangle^2$ increases by nearly 30% [Fig. 3.14(b)]. For broad size distributions with particle sizes varying by a factor of 5, Fig. 3.8 shows the largest particles have on average a magnitude of nonaffine motion $|\Delta\vec{r}_{NA}|$ that is 16% smaller than that of the smallest particles; and likewise while the data are noisier, D_{min}^2 is smaller for the larger particles. Finally, Fig. 3.10 shows that the smallest particles barely perturb the motion of their neighbors, whereas the largest particles significantly enhance the nonaffine motion in their immediate vicinity. The range of this enhancement is fairly short, about 2-3 small particle diameters.

Our analysis shows some differences between globally nonaffine motion ($\Delta\vec{r}_{NA}$) and locally nonaffine motion (D_{min}^2). The former compares particle motion to the spatially smooth mean flow, whereas the latter compares particle motion to a flow defined locally in space and time. The globally nonaffine motion is not significantly influenced by the particle polydispersity, suggesting that enhanced nonaffine motion for smaller particles is balanced by a decreased nonaffine motion for the larger particles. The locally nonaffine motion has the dependence on sample polydispersity. Both types of nonaffine motion are strongly enhanced in the presence of large particles. As noted in prior work, this implies that mixing can be enhanced in these mixtures of particle sizes [32].

We also see that while large and small particles play different roles, it appears that polydispersity is the most significant factor determining the results; the size ratio R_{max}/R_{min} between the largest and the smallest particles matters less. This is

seen in the comparison of tridisperse distributions with fixed particle sizes but differing polydispersity, where polydispersity changes the results in a predictable way. In contrast, data from size distributions with different R_{\max}/R_{\min} but matched polydispersity have essentially equivalent results.

In summary, we find that the flow of highly polydisperse materials is dramatically more complex than the flow of less polydisperse materials. This suggests that models of localized rearrangements in the flow of amorphous materials may need to be adjusted to account for the roles of particle size and overall polydispersity [28, 154]. Not all particles are equivalent; not all particle size distributions are equivalent.

Chapter 4

Clogging of cohesive particles in a two-dimensional hopper

We investigate the clogging of frictionless cohesive particles in a two-dimensional hopper using simulations and experimental data. The magnitude of the effective gravitational force, the cohesive strength between droplets, and the size of the hopper opening are varied. We find that stronger cohesion leads to enhanced clogging. These results are confirmed both in simulations and experiments. We also investigate the number of particles that can flow before a clog occurs and find that increasing cohesive strength decreases the number of particles which escape the hopper. By balancing the effective gravitational force with the cohesive strength we obtain a cohesive length scale which we find can effectively collapse our data onto a single curve. These results indicate that, for cohesive granular materials, particle size alone is insufficient to describe clogging and a cohesive length scale must be taken into account.

4.1 Introduction

Hoppers and silos have widespread usage in a variety of industries[55, 155, 156], which makes the flow of granular materials through constricted outlets a widely re-

searched subject, with a focus in the clogging of these systems and the clogging frequency [45, 47, 48, 157–161]. Often times the ratio of the hopper opening to the particles’ diameter, w/d is used as a parameter to characterize clogging [48, 161]. However, there remain a wide variety of parameters known to affect the flow and clogging in a hopper besides particle size and exit width, such as friction [162–164], particle softness [52, 101, 165–168], particle shape [51, 169–171], effective gravity [8, 172, 173] and hopper angle [174–176].

Inter-particle cohesive interaction is an often observed phenomena in granular materials. There can be multiple causes for this behaviour, for example in small powders, electrostatic and Van der Waals forces will create an attractive force between the particles [53]; in larger particles, cohesion can arise due to liquid capillary bridges [54]. These cohesive forces can significantly impact flow properties [55, 56, 177]. While cohesion is an important parameter, it is typically difficult to control. Recently, Gans *et al.* have developed a ‘cohesion controlled granular material’ and have used this experimental model system to study the impact of cohesion on properties of granular materials including the flow rate of materials through a silo [178, 179]. These results indicate that, for systems with a cohesive component, the use of cohesion length scale was needed to describe the characteristics of the flow [179]. Additionally, Zhang *et al.* investigated the clogging of wet granular materials and found that liquid cohesion increasing clogging probability, which could be predicted using an effective aggregate size instead of the particle size [180].

In this chapter, we study the flow of cohesive particles through a quasi 2-D hopper. We will use simulations as well as experiments done by our collaborators, to study the flow dependence on various conditions including hopper width opening, effective buoyancy, the inter-particle cohesion, and the size distribution of the particles in the hopper.

The following chapter will be split in 2 sections. Section 4.2 will detail the methods

used in the experiments, as well as the numerical methods utilized in the simulations. In Section 4.3 we will analyze the out-flowing particle mass, as well as the clogging probability for different depletion strengths and effective gravity.

4.2 Methods

4.2.1 Computational methods

As in Chapter 2, for the simulations of the hopper we use a quasi 2D “Durian bubble model” [87], as modified in Refs. [21, 52], where we have added gravity to the forces being simulated. This model considers soft particles with large viscous forces acting on them, such that all other forces balance the viscous drag force. Thus at each time step the equations of motion are solved for the velocity rather than the acceleration. For each particle i the equation to solve is:

$$\sum_j \left[\vec{F}_{ij}^{\text{contact}} + \vec{F}_{ij}^{\text{visc}} \right] + \vec{F}_i^{\text{wall}} + \vec{F}_i^{\text{grav}} + \vec{F}_i^{\text{drag}} = 0, \quad (4.1)$$

where $\vec{F}_{ij}^{\text{contact}}$ is the contact force between droplets i and j , as seen in Eq. 2.1:

$$\vec{F}_{ij}^{\text{contact}} = f_0 \left[\frac{1}{|\vec{r}_i - \vec{r}_j|} - \frac{1}{|R_i + R_j|} \right] \vec{r}_{ij}. \quad (4.2)$$

Here \vec{r}_i is the position of the i droplet, with radius R_i , and f_0 is the spring constant of a droplet. $\vec{F}_{ij}^{\text{visc}}$ is the viscous interaction between two contacting droplets, referring back to Eq. 2.2:

$$\vec{F}_{ij}^{\text{viscous}} = b(\vec{v}_i - \vec{v}_j), \quad (4.3)$$

with b being the viscous coefficient, and \vec{v}_i the velocity of a given particle. This force acts on each droplet in a direction that tries to bring their velocities into agreement: for example, if droplet i is motionless then the viscous force from droplet j acting on

i is in the direction of v_j . We also define the viscous drag on a the bubble i as:

$$\vec{F}_i^{\text{drag}} = -bv\vec{v}_i \quad (4.4)$$

where b is the same constant used for $\vec{F}_{ij}^{\text{visc}}$. As with the forces previously mentioned in this chapter, the adhesive depletion force is calculated in the same way as in chapter 2, Eq. 2.5, based on the Asakura-Oosawa model [99]:

$$\vec{F}_{ij}^{\text{dep}} = \frac{\phi_c}{8a_s^3} \frac{\partial V_{\text{overlap}}(r_{ij}, R'_i, R'_j)}{\partial r_{ij}} \hat{r}_{ij}, \quad (4.5)$$

where ϕ_c is the constant related to the depletion strength, and is analogous with the micelle concentration C_m in the experiments. R'_i is defined as $R'_i \equiv R_i + a_s$, where $a_s = 1/20$ is the depletant radius. Finally $\partial V_{\text{overlap}}/\partial r_{ij}$ is the overlap between two particles. \vec{F}_i^{wall} acts on droplets which overlap the wall and includes a repulsive force, an attractive depletion force, and a viscous force. The forces previously mentioned were discussed in further detail in chapter 2.

In addition we also must include the gravitational pull on a droplet:

$$\vec{F}_i^{\text{grav}} = -\rho g R_i^3 \hat{y}, \quad (4.6)$$

where we set $\rho = 1$ as the droplet's density, and g is the gravitational constant which drives the particles through the hopper exit. Additionally we must also calculate the depletion forces at the hopper exit, which is non trivial due to asymmetric geometry. The calculations are based on the overlapping volume of a sphere with radius $R' = R + a_s$ and a triangular prism, which results in a repulsive force away from the point at the hopper exit.

The time step is defined by $t_0 = b\langle R \rangle / 2f_0$, which is the timescale for two droplets to push apart, limited by inter-droplet viscous interactions. To best match our experimental counterpart, we generate 190 particles with a hopper wedge at an angle

of 45° , and a droplet polydispersity set at 0.01. The width of the hopper openings ranges from $w = 4R$ in the lowest depletion case to $w = 15R$ for the highest depletion case. A simulation is initialized by generating the particles at random positions above the hopper exit, which are then allowed to free fall towards the exit and settle. Once the particles are static, the hopper exit is opened. Eq. 4.1 can be rewritten as a first order differential equation for the velocity, which is solved using a fourth-order Runge-Kutta algorithm and a time step of $t_0 = 0.05$, as previously stated. Simulations end when all droplets have exited the hopper, or when the maximum speed of all particles in the hopper is below 10^{-12} ; the latter case defines a clog. For these simulations the choice of parameters for depletion strength and gravity were made based both on previous simulations involving cohesive forces in Chapter 2[21], and hopper simulations[52], with the overall goal of maintaining a range of parameters in line with the experiments. One set of simulations keeps $g = 0.01$ constant and varying the width of the opening w and depletion strength ϕ_c , from $\phi_c = 0$ to $\phi_c = 3 \times 10^{-4}$. A second set of simulations keeps $w/\langle R \rangle = 3$ constant and varies g and ϕ_c . In Fig. 4.1(a) we show a representative image of the hopper simulations where the flow has stopped due to a clog.

4.2.2 Experimental methods

Experimentally, the role of the inter-particle interactions is investigated using monodisperse cohesive oil droplets as a model system. Our collaborators, Johnathan Hoggarth and Kari Dalnoki-Veress at McMaster University, vary the size of the droplets, the size of the hopper opening, the cohesion between the droplets, and the effective buoyancy.

In previous studies, Ono-dit-Biot *et al.* developed a model system using oil droplets in a surfactant solution to control inter-particle cohesion of a frictionless system [18, 20], which chapter 2 replicated and expands upon. The surfactant has

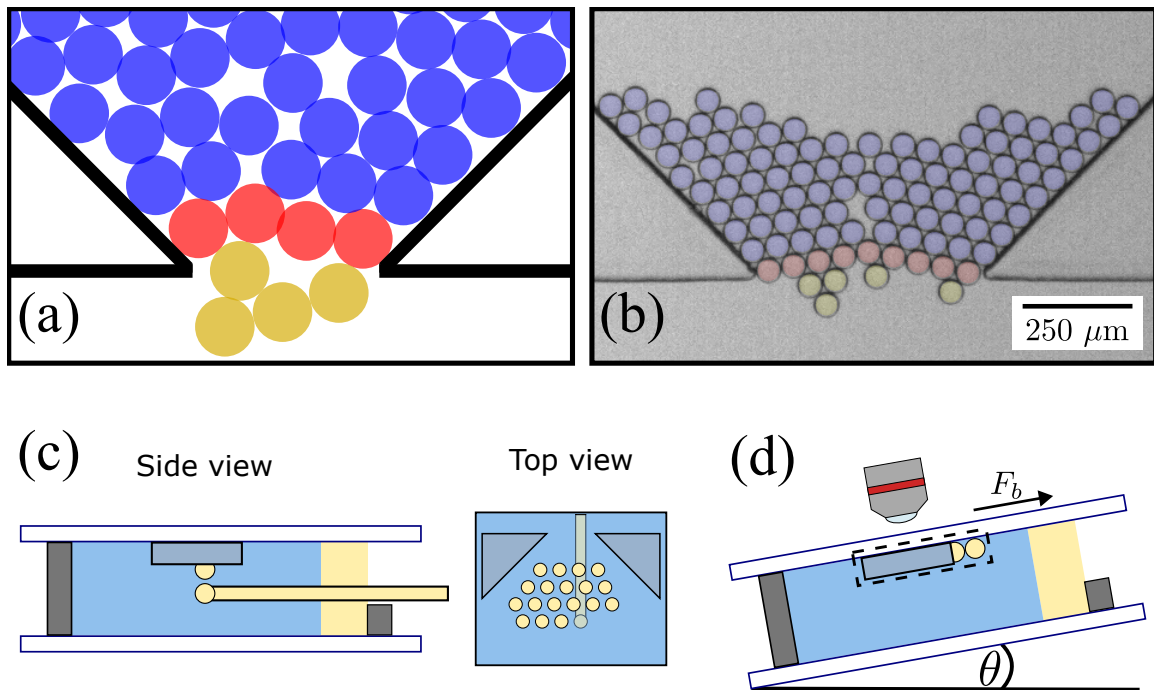


Figure 4.1: (d) Representative image showing a clog in simulations, with a colour overlay: Red droplets indicate the clogging arch, blue droplets represent remaining droplets, yellow droplets remain attached to the aggregate due to cohesion. In this particular simulation $w/d = 3.25$, and $w/\delta = 5.00$. (b) Representative experimental image showing a clog, with $w/d = 8.8$ while $w/\delta = 2.86 \pm 0.07$. (c) Side and top view schematic diagram of the experimental chamber. Droplets are deposited and float to the bottom of the top slide while the chamber is held horizontal. (d) During the experiment, the chamber is rotated to a desired tilt angle which drives the droplets due to the buoyant force.

two roles in the system. First of all, the surfactant stabilizes the droplets against coalescence. Second, when added in excess, the surfactant forms micelles which act as a depletant causing an attractive interaction [18, 181, 182]. Critically, the concentration of surfactant allows for precise control of the cohesive force by tuning the concentration of micelles within the solution without the need to change any other system properties.

Experimentally, a quasi-2D hopper is made by coating a glass slide with a ~ 100 μm layer of SU-8 photoresist and photolithography is used to pattern a hopper with walls at 45° angles. For the experiments, the hopper opening width spanned from 100 μm to 500 μm , with most experiments performed at 150 μm or 200 μm . Experimental chambers are made by sandwiching a 3D printed spacer between the slide with the 2D hopper and a glass microscope slide. A schematic diagram of the experimental chamber is shown in Fig. 4.1 (c) and (d). The chamber is placed on a rotation stage such that hopper can be rotated to a specific tilt angle. Additionally, a camera is placed on the same rotation stage such that the hopper remains in focus regardless of the angle.

Chambers are filled with an aqueous solution of the surfactant, sodium dodecyl sulfate (SDS), and sodium chloride (NaCl) to screen ionic interactions. The concentration of SDS varied from 7 mM to 265 mM while the concentration of NaCl was held constant at 1.5% (w/w). SDS micelles act as a depletant which causes an attractive interaction between oil droplets that increases linearly with the concentration of micelles, C_m [18, 181, 182]. The droplets rise in the chamber due to buoyancy and fill the hopper. The chamber is initially held horizontally and droplets are deposited in a loosely packed pattern. After 190 ± 5 droplets have been deposited, the pipette is removed away from the hopper and the chamber is rotated to a desired tilt angle, θ , which initiates the flow of droplets through the hopper. Droplets are monitored over time for the presence of clogs. A representative image of an experiment where a clog

occurred is shown in Fig. 4.1 (b). Once all the the droplets flow through the hopper, or if a clog is detected, the experiment is considered completed and the chamber is rotated past 90° , which clears the chamber of the droplets. Once the hopper is emptied, the chamber is rotated back to horizontal and the process of filling the hopper with droplets is repeated. The process of filling the hopper with droplet, tilting to run an experiment, and emptying once complete, was fully automated and repeated 20 times for a specific set of parameters.

4.3 Results

We first investigate the combined impact of the effective gravitational forces and cohesion by observing clogging probability using different g and ϕ_c parameters, while keeping the width to droplet diameter constant at $w/d=3$. In Fig. 4.2 (a) we show P_{clog} as a function of g , for a variety of different depletion strengths. We see that for a constant cohesion strength (corresponding to a single curve), an increase in the gravitational forces corresponds to a decrease in the clogging probability. We can additionally compare the same g value for different values of ϕ_c , and find that increasing cohesion increases the clogging probability. These results are physically intuitive: increasing the gravitational force destabilizes a potential arch, thus decreasing the potential to clog. Furthermore, increasing the cohesive strength stabilizes arches and increases the likelihood of a clog. We can compare these results to those obtained by our collaborators through experiments, Fig. 4.2(b). To vary the effective gravitational forces, our collaborators tilt their hopper at different angles θ , resulting in an effective buoyancy of

$$F_g = \frac{4\pi}{3} R^3 \Delta\rho g^{\text{exp}} \sin \theta, \quad (4.7)$$

where $g^{\text{exp}} = 9.8\text{m/s}^2$ is the gravitational acceleration, $\Delta\rho$ is the different in densities of the oil droplets and water, and R is the droplets radii. Cohesive strength

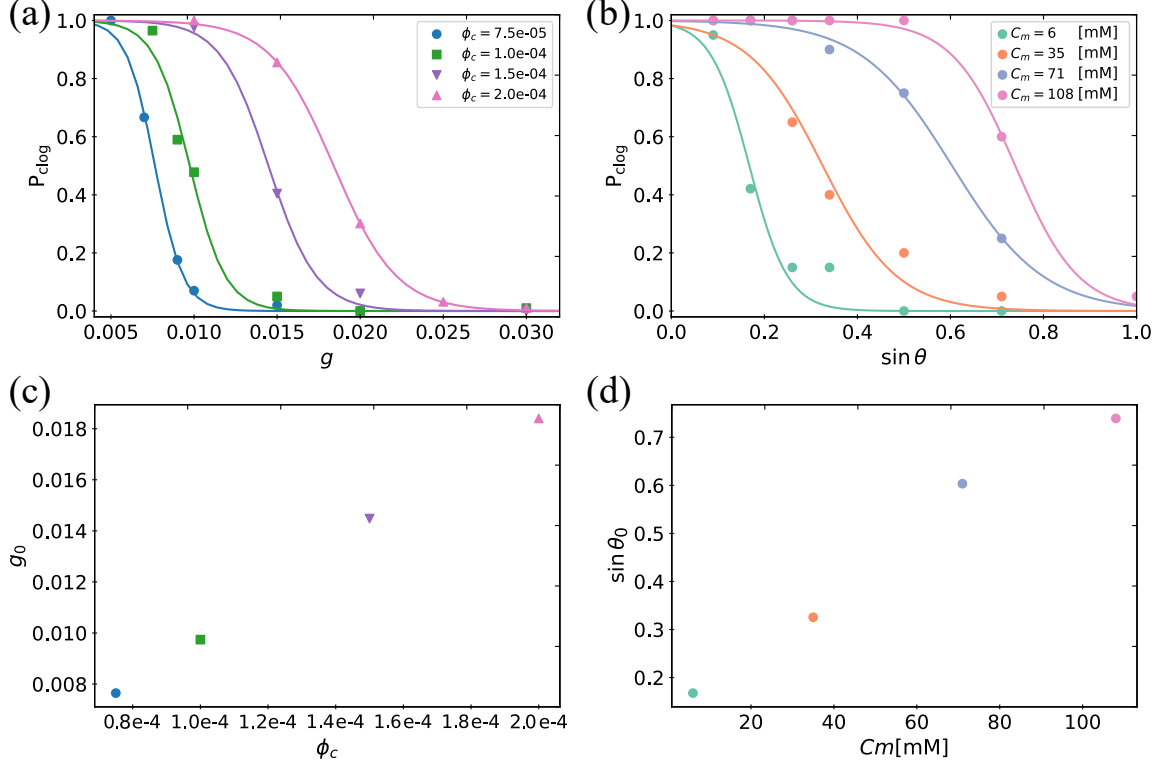


Figure 4.2: Clogging probability of (a) simulations and (b) experiments with $w/d = 3.0$ for a range of cohesive strengths as a function of strength of the effective gravitational forces g , and effective buoyant forces $\sin \theta$. Solid lines represent fits of Eq. 4.8 to the data. The value of the driving force where the probability of clogging is $P_{\text{clog}} = 1/2$ as a function the cohesive strength is shown for c) simulation and d) experiment.

is varied through the micelle concentration C_m . As in Fig. 4.2(a) for a constant cohesion strength, an increase in effective buoyancy results in a decrease clogging probability.

We use a sigmoidal function to fit both the simulation and experimental data:

$$P_{\text{clog}} = [1 + e^{(g-g_0)/\alpha}]^{-1}, \quad (4.8)$$

where g_0 represents the value at which the gravitational force results in $P_{\text{clog}} = 0.5$ and α is a measure of the width of the transition. For the experiments $\sin \theta$ and C_m are varied, which are analogous to the simulation parameters through $g \leftrightarrow \sin \theta$ and $\phi_c \leftrightarrow C_m$. In Eq. 4.8 the argument in the exponential, $(g - g_0)$ becomes $(\sin \theta - \sin \theta_0)$

for the experiments. We then plot the points corresponding to $P_{\text{clog}} = 0.5$, g_0 and $\sin \theta_0$ as a function of ϕ_c and C_m , in Fig. 4.2 (c) and (d), respectively. The trend for both simulation and experiment is monotonically increasing, which is expected: for the probability of clogging to remain constant ($P_{\text{clog}} = 0.5$), the force driving the droplets through the hopper must increase with increasing cohesion, which reinforces clogging mechanisms.

To capture the interplay between the driving gravitational forces and the cohesive forces in our systems we will use the ‘granular capillary length’, δ . This cohesive length scale was proposed by Ono-dit-Biot and co-workers [18], and sets a balance between inter-particle cohesion and the effect of gravity. The cohesive granular length is analogous to the capillary length associated with liquids and is defined by:

$$\delta = \sqrt{\frac{\mathcal{A}}{\rho g}}, \quad (4.9)$$

where ρ is the effective density ($\rho = 1$ for our simulations, and $\rho = \Delta\rho$ for the experiments). For the experiments g in Eq. 4.9 is $g = g^{\text{exp}} \sin \theta$, while in our simulations, our g in Eq. 4.6 is the same g in Eq. 4.9. \mathcal{A} is the cohesive force per unit length, analogous to the surface tension in a continuous liquid, and is defined by:

$$\mathcal{A} = \frac{F_c}{R\pi}. \quad (4.10)$$

Where R is the droplet radius, and F_c is the force needed to pull apart two bubbles. For our simulations we calculate F_c using Eq. 2.12, the equilibrium separation d_{eq} , for two droplets at given ϕ_c , and inserting it into Eq. 2.5. Our collaborators obtain \mathcal{A} by directly measuring F_c . Previously, the granular capillary length has been used to describe the spreading of oil droplets in both two- and three-dimensions [18, 183].

We note that for the simulations, when the force needed to separate two droplets, F_c , is equal to a single droplets weight, is when the depletion forces are strong enough

to hold one droplet. Using Eqs. 4.6, 4.9 and 4.10, we can obtain the value of δ for which $F_c = F_g$, which results in $\delta = (\sqrt{\pi})^{-1} \approx 0.6$.

We next vary the opening width for a variety of depletion strengths, while keeping g constant. In this manner we probe the direct effect that varying depletion strength has on the clogging probability. For this data set we will again use a sigmoid formula, similar to Eq. 4.8, but with a w/d dependence:

$$P_{\text{clog}} = [1 + \exp((w/d - w^*/d)\alpha^{-1})]^{-1}, \quad (4.11)$$

where w^* is the opening width for which $P_{\text{clog}} = 0.5$, and as before α is the approximate width of the transition. In Fig. 4.3 we show P_{clog} as a function of w/d for different ϕ_c values, where we have used Eq. 4.11 to fit the data for each ϕ_c value. Similar to what we observed for Figs. 4.2, as the depletion strength increases, the hopper must have a wider exit. These results are physically intuitive: increasing the cohesive strength stabilizes any potential arches, thus increasing the potential to clog. Furthermore, widening the hopper exit makes the formation of any arches less likely and decreasing the probability of a clog.

Having obtained the w^* from the data set shown in Fig. 4.3, using Eq. 4.11, we plot these points as a function of δ , as shown in Fig. 4.4. As hinted by Fig. 4.3, w_0 grows with δ , albeit very slowly for $\delta < \delta(\phi_c = 7.5 \cdot 10^{-5})$, showing that depletion has minimal effect on clogging. On the other hand for $\delta > \delta(\phi_c = 7.5 \cdot 10^{-5})$, we see a rapid increase in clogging probability as δ increases. These two behaviours are indicators of different physics affecting the clogging probability. As we mentioned previously, $\delta_{\text{crit}} \sim 1$ is when the depletion and gravitational forces are at equilibrium for a pair of droplets. Therefore, it is intuitive that we see a change in behaviour around this value of δ , and this is seen in Fig. 4.4, for $\delta(\phi_c = 7.5 \cdot 10^{-5}) = 0.90$. We then fit each of these data points separately. For the high depletion rate the clogging

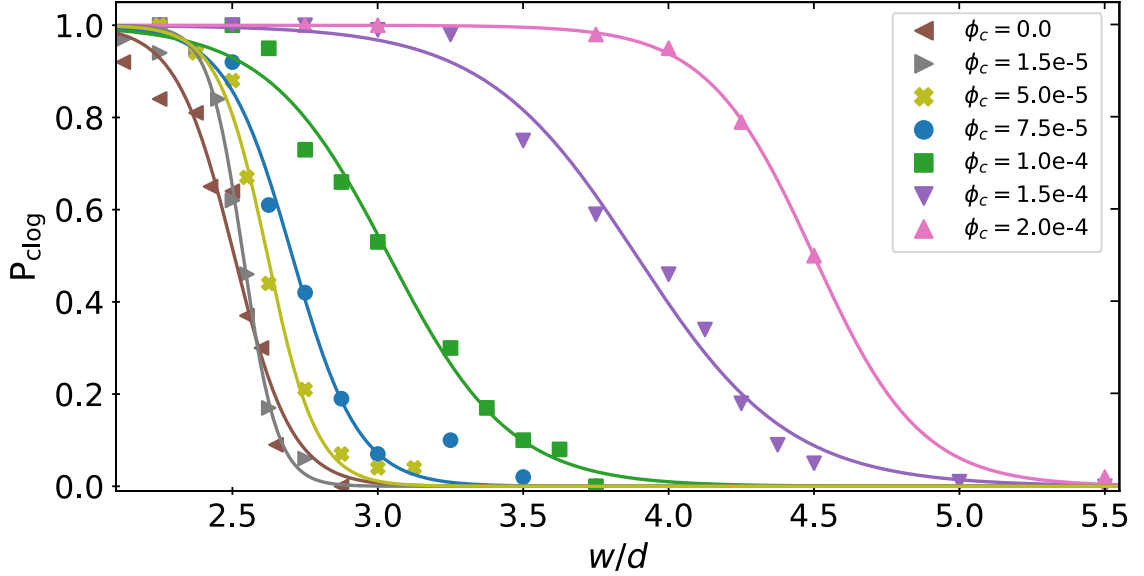


Figure 4.3: Clogging probability for a range of cohesive strengths as a function of the hopper opening width over the droplets diameter(w/d), for constant g . Solid lines represent fits of Eq. 4.11 to the data. For increasing ϕ_c wider hopper exits are needed in order to avoid clogging, meaning that the particles clog easier if they are more cohesive.

probability is mostly dominated by the cohesive forces and we have fit the opening width linearly, with $w_{\text{high}}^* = m_{\text{high}}\delta$, with $m_h = 5.92$. On the other hand for the low depletion regime, we use the mean value of the opening widths such that, $w_{\text{low}}^* = 5.19$. This is due depletion effects being negligible in this range. For convenience we will redefine δ^* as a split function for high and low cohesion cases as follows:

$$\delta^* = \begin{cases} C_{\text{low}} & \text{for } \delta < \delta_{\text{crit}} \\ \delta & \text{for } \delta > \delta_{\text{crit}}. \end{cases} \quad (4.12)$$

where $C_{\text{low}} = 5.19/m_{\text{high}} \approx 0.87598213 \sim R$, and we define δ_{crit} to be at the intersection of our two fits:

$$\delta_{\text{crit}} = C_{\text{low}} = 0.876. \quad (4.13)$$

Our collaborators experiments are all in the high depletion regime, where $\delta > \delta_{\text{crit}}$. Having a better understanding of the effect of cohesive and driving forces on the

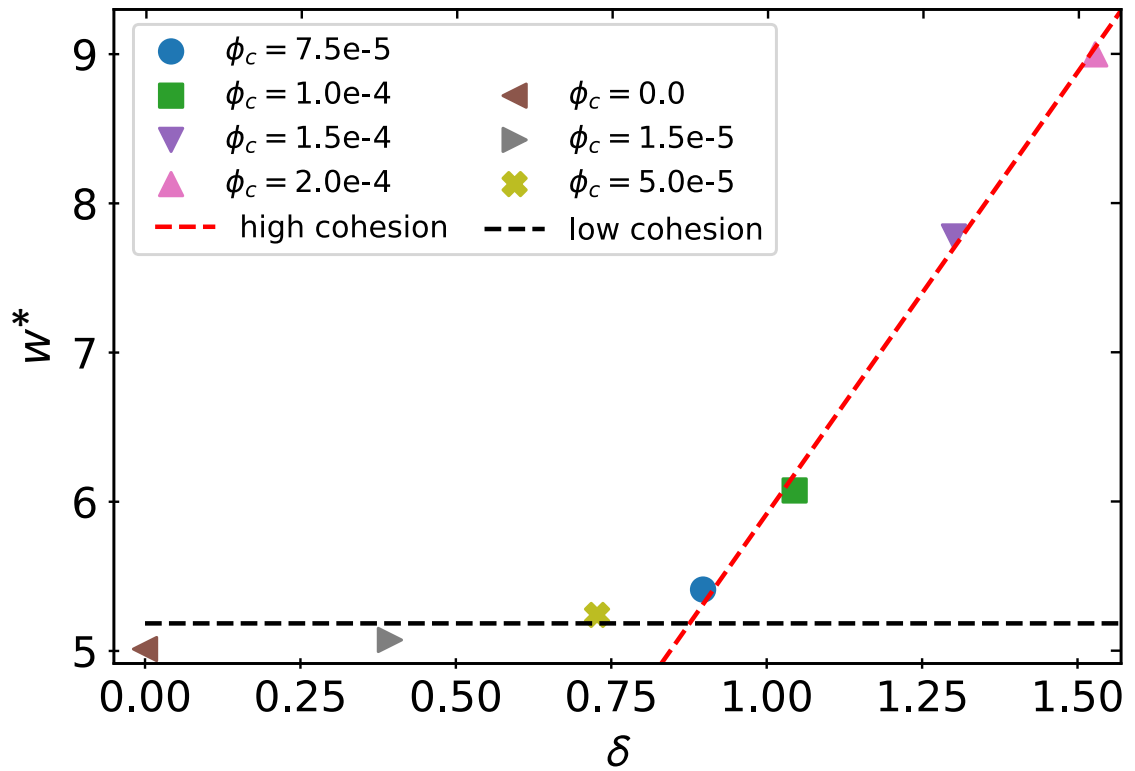


Figure 4.4: w^*/d as a function of δ . Close to $\delta \approx 1$ there's a change in the behaviour for w^*/d , as we expected. We have therefore chosen to fit these behaviours differently. The black dashed line represents the linear fit for low cohesion, while the red dashed line is the linear fit for high cohesion.

clogging probability, we now turn to the impact on the amount of particles that exit the hopper before a clog occurs. Experiments and simulations were performed with various values of the driving force and cohesive strengths while changing w/d . We characterize the flow of the droplets by finding the number of particles which flow through a hopper prior to a clog, or the mean avalanche size, $\langle s \rangle$. Typically, $\langle s \rangle$ is plotted as a function of w/d in cases where cohesion is negligible [161]. However, for our system with strong inter-particle cohesion, we propose that the critical length-scale that determines clogging is not the droplet diameter d , but rather the cohesive length scale δ^* , which will collapse our data for the clogging probability. We note that this assumption is consistent with observations made by Gans *et al.* when investigating the flow of cohesive particles through a silo [179] and other works [18, 20, 21, 183]. We further justify the use of this length scale because as the cohesion is increased the relevant parameter is not the droplet size, but rather the size of cohesively stabilized aggregates which depends on buoyancy and cohesion – one can think of a small stable aggregate as re-normalizing w/d to w/δ^* since d is no longer the relevant parameter. For our simulations the droplet diameter is $d = 2R = 2$, and our values for δ range from 0 to 1.9. Additionally, we have performed simulations at $\phi_c = 10^{-4}$ and $g = 0.01$, with $N = 95$ and $N = 285$. To be able to compare avalanche sizes for different droplet numbers, the avalanche size has been normalized and then multiplied $N = 190$, since most simulations use this number of droplets. In our collaborator’s experiments the droplet diameters range from $52 \mu\text{m}$ to $67 \mu\text{m}$, and the values of δ range from $30.5 \pm 0.3 \mu\text{m}$ to $260 \pm 10 \mu\text{m}$ [18].

A plot of $\langle s \rangle$ as a function of w/δ is shown in Fig. 4.5 (a) and (b) for simulations and experiments, respectively. For both data sets, the number of particles present within the hopper is a limiting factor and therefore our plot in Figs. 4.5 show a plateau at an avalanche size of 190 droplets. The plateau does not imply that we have reached a critical value for which clogging never occurs, but instead have reached a region

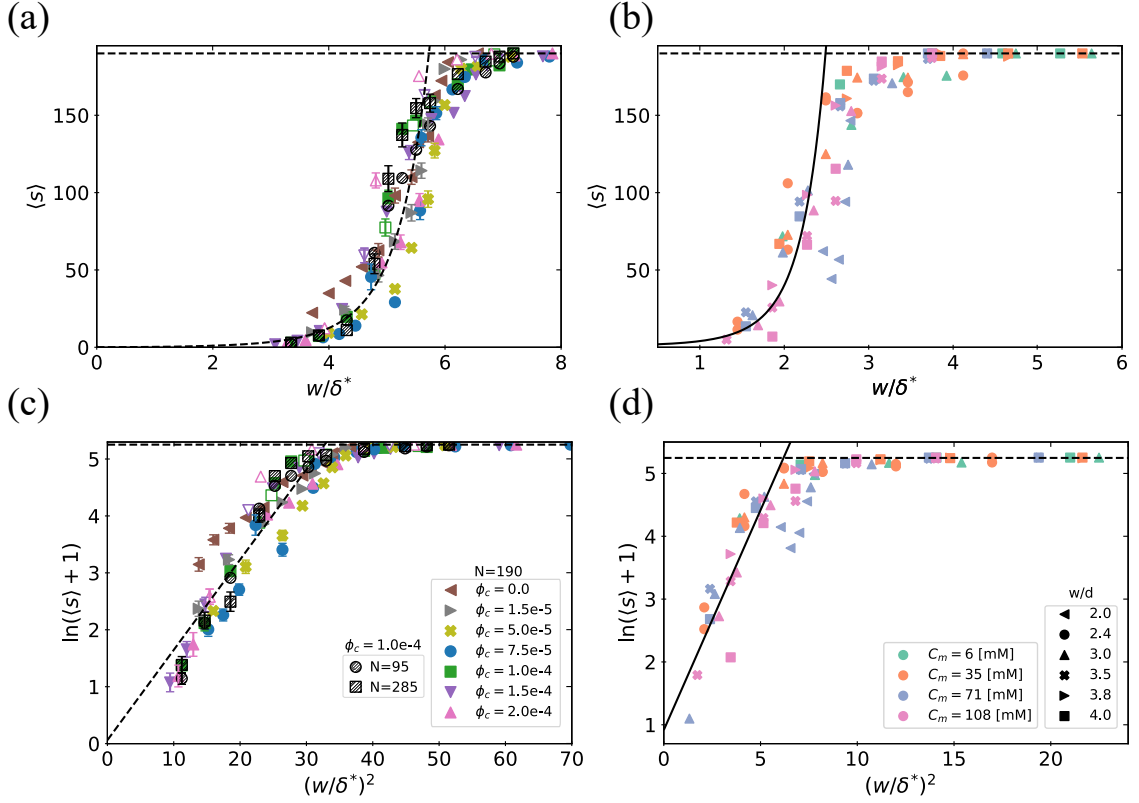


Figure 4.5: Figs. (a) and (b) show the mean avalanche size before a clog occurs plotted against the dimensionless ratio w/δ^* , for simulations and experiments, respectively. The solid line is a fit to Eq. 4.17. Figs. (c) and (d) shows $\ln(\langle s \rangle + 1)$ as a function of w/δ^* , for simulations and experiments respectively. Using Eq. 4.18 we were able to fit the data, dashed lines in Figs.(c) and (d), and obtain the parameter to plot Eq. 4.17 in Figs.(a) and (b). Dashed lines show a plateau at 190 droplets. For the simulations the empty symbols are data point with variable g , whereas the stripped data points are simulations with $N = 95$ for the circles, and $N = 285$ for the squares.

where the probability of clogging for our small number of particles vanishes.

In previous studies of 2D hopper flow of cohesionless particles, Janda *et al.* proposed a model to describe the average avalanche size as a function of the dimensionless ratio of hopper opening to particle size, w/d [47]. They proposed that the probability that an avalanche will contain s particles is

$$n_{w/d}(s) = p^s(1 - p) \quad (4.14)$$

where p is the probability of a single particle passing through the hopper opening. It is assumed that each particle acts independently of each other. The average avalanche size can be written as

$$\langle s \rangle = \frac{1-p}{p}. \quad (4.15)$$

The clogging probability is dependent on a particle being able to form a stable arch, which in turn is dependent on the size of the particle and hopper opening. Using the results from two different simulation techniques [184, 185] leads to an equation for the probability of a particle to clog:

$$1-p = A \exp(-Bx^2), \quad (4.16)$$

where A and B are fitting parameters and $x = w/d$ is the dimensionless ratio of the hopper opening compared to droplet size. The average avalanche size can then be obtained from Eqs. 4.14 through 4.16 as:

$$\langle s \rangle = A^{-1} \exp(Bx^2) - 1, \quad (4.17)$$

In the work by Janda *et al.* using non-cohesive particles, $x = w/d$, which is modified to $x = w/\delta^*$ for the cohesive particles of this chapter, shown in Figs. 4.5 (a) and (b). Eq. 4.17 can also be rewritten as a linear equation which expresses the mean avalanche size as:

$$\ln(\langle s \rangle + 1) = \ln A^{-1} + Bx^2. \quad (4.18)$$

We plot $\ln(\langle s \rangle + 1)$ as a function of $(w/\delta^*)^2$ in Fig 4.5 (c) and (d) and use Eq. 4.18 to obtain fit parameters $A = 0.12 \pm 0.03$ and $B = 0.029 \pm 0.001$ for simulation data and $A = 0.4 \pm 0.1$ and $B = 0.70 \pm 0.09$ for experimental data. When fitting our data we use values for which $\langle s \rangle$ is less than 75% of the total particles in the hopper as this lets us focus on the region where the plateau has less influence on our data. The

ability of our data to collapse onto a master curve as well as the goodness of fit to Eq. 4.17 and 4.18, when using the ratio of the width to the cohesive length, w/δ^* , justifies the assumption that this non-dimensional length scale describes the clogging process of cohesive particles.

To further investigate the importance of w/δ^* to our system, the probability of clogging as a function of w/δ^* is plotted in Fig. 4.6. Similar to the treatment of $\langle s \rangle$, using w/δ^* collapses our data onto a single master curve. Taking further influence from Janda *et al.*[47], the probability of clogging for a hopper containing N particles is:

$$P_{\text{clog}} = 1 - \exp(-N/\langle s \rangle). \quad (4.19)$$

By substituting $\langle s \rangle$ with Eq. 4.17 and using $x = w/\delta^*$ in Eq. 4.19 the probability of clogging can be written as:

$$P_{\text{clog}} = [1 - \exp(-NA \exp(-B(w/\delta^*)^2))] . \quad (4.20)$$

Where $N = 190$ is the number of particles in the hopper, and A and B are the same fit parameters found in Eqs. 4.17 and 4.18. We find that Eq. 4.20 is a satisfactory description of the data. The agreement between the theory, the simulation and experimental data further confirms that the critical parameter describing clogging is given by w/δ , for high cohesion systems.

4.4 Conclusions

In conclusion, we have observed the clogging of frictionless cohesive particles in a 2D hopper and outlined the impact of the cohesive strength and effective buoyancy on the ability for the particles to flow. We find a clear positive correlation between the cohesive strength and the probability of clogging. Furthermore, we have demonstrated

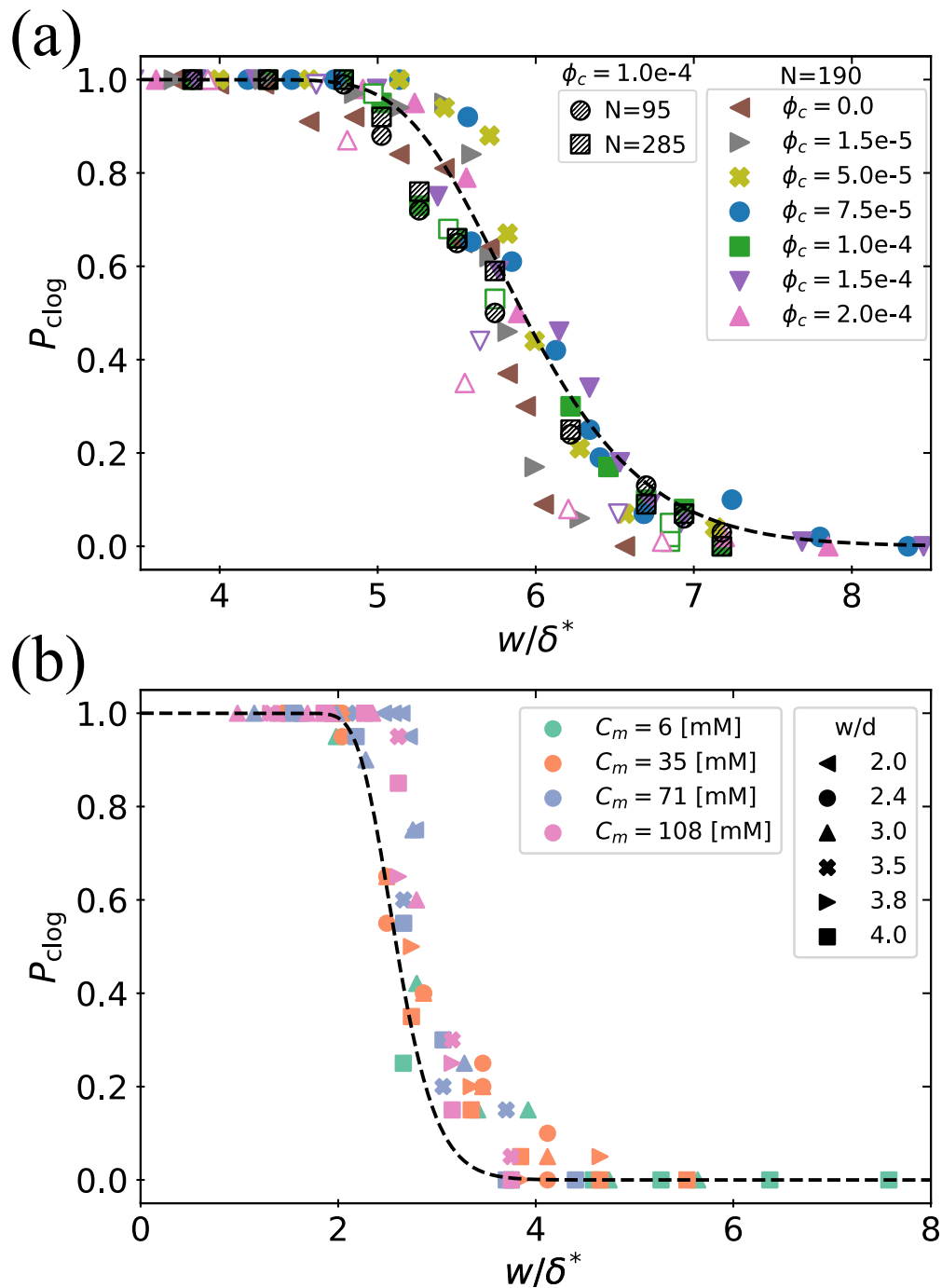


Figure 4.6: Probability of clogging as a function of w/δ^* . The data for both simulations and experiments collapses onto one master curve. The dashed line represents a fit to Eq. 4.20 using $A = 0.12 \pm 0.03$ and $B = 0.029 \pm 0.001$, for the simulations, and $A = 0.4 \pm 0.1$ and $B = 0.70 \pm 0.09$ for the experiments. For the simulations the empty symbols are data point with variable g , whereas the striped data points are simulations with $N = 95$ for the circles, and $N = 285$ for the squares.

that a fundamental cohesive length scale which can be obtained by balancing the cohesive strength with the effective buoyant force is critical to describing clogging. The transitions between the low and high depletion clogging regimes occurs at $\delta_{\text{crit}} = 0.89$, which is close to the δ for which a droplet can hold the weight of another droplet through depletion. When plotting both the mean avalanche size and the clogging probability as a function of a dimensionless ratio w/δ^* , our data collapsed on a master curve underscoring the importance of cohesion in hopper flow. Additionally, previously derived equations by Janda *et al.*, which used the hopper width to droplet diameter ratio w/d , can be used to describe our data accurately by using w/δ^* in place of w/d . Critically, when examining flow through large hopper opening sizes, such as in the simulations shown in Fig. 4.1(a), although the hopper opening is $w/d = 3.25$ and significant clogging would not be expected for cohesionless systems, the cohesion in our system leads to a value of $w/\delta^* = 2.50$, and we observe clogging occurring readily. Of note is that the simulation and experimental data do not collapse into each other despite δ^* successfully collapsing each data set separately. This is most due to the systems having different particle characteristics which are known to affect clogging, mainly the softness of the particles[52, 101]. Finally we assert that when cohesion is strong between particles, the relevant length scale to predict clogging can no longer be obtained through the particle diameter, but instead a cohesive length scale needs to be taken into account.

Chapter 5

Conclusions

The study of the plastic deformation of materials under stress has been a subject of extensive research for centuries. Due to their large presence in the industrial and natural world better understanding how these materials react is incredibly important. For example, natural disasters like avalanches and mudslides are amorphous systems in which a material is plastically deformed under stress, and then continue to flow as granular material. Understanding the mechanism in which these events are triggered and being able to predict when they could happen is invaluable. On the other hand, in an industrial setting, understanding when a brittle material will fail under load is of extreme importance, and so is understanding the flow of granular particles. As an example, understanding the flow of particles through a bottle neck can potentially save resources and avoid industrial accidents, but can also be used to improve evacuation times in largely crowded venues. My goal is to better understand these materials at the particle length scale, that is to say, what are the properties of individual particles, and how these properties affect the behaviour of the system as a whole. However the field studying this subject is enormous. If each Chapter in this dissertation were to be a single pebble, then the whole field would be a mosaic. With each added piece helping create a better, more brilliant picture.

In my first project, Chapter 2, we investigated the response of a simulated brittle quasi 2D material under compression, and how changes in the size, aspect ratio of these materials, and the polydispersity its constituent particles, affect the response the system has to external compressive stress. As a reminder, we simulated a 2D array of droplets with attractive interactions as they are compressed between two walls. Using this method we show that elastic properties of the droplet arrays are related to the intrinsic spring constant acting between a pair of contacting droplets. The attractive interactions between the droplets increase the overall stiffness of the array. We also confirm that the force requires to initiate a fracture event, a plastic deformation, scales with the aggregate size. Thirdly we found that increasing the polydispersity in the system dramatically increases the number of fracture events, while decreasing the force needed to initiate those fractures. We found that adding in any density of defects in an otherwise monodisperse hexagonally packed crystal, dramatically increases the ease of breaking the crystal. The results of these work are consistent with previous experimental work[19, 20], and help better understand the properties of various crystal and glassy materials, and how the presence of defects can affect their response to external stress. I believe this simulation method to be robust enough to be easily expanded to 3D arrays, which can be achieved by adding the same equations of motion already used in a third direction, and appropriately expanding the arrays containing the particles positions and velocities. Additionally this code can also be used to study a materials response to extensional and torsional stress, which can be done by simply reversing the direction of the walls, for extensional stresses, or once the 3D code has been implemented, by twisting the particles adjacent to the wall about a center point in the wall. Doing so would allow us to probe the response of materials such as bulk metals, crystals and glasses. Modifying the simulation to achieve this goals is not a particularly complex task, and improving the computational speeds, coupled with improved hardware would permit the simulation of even larger

arrays. On the other hand larger forces which could deform particles would not be well suited for this code, and even with more efficient code and improved hardware, arrays more than an order of magnitude higher could prove to be extremely slow to simulate. In summary we have provided a simulation framework in which various crystal and glassy structures can be probed under a variety of stresses. Additionally we have shown the relation between the particles' properties and particle distribution properties, and various properties relating to fracture events in the crystal and glassy arrays.

My second project focused on the 2D flow of acrylic disks, and how polydispersity affected the properties of the flow. Consistent with previous work that studied similar systems [32], we found that large particles tend to move more with the overall flow of their vicinity, due to being subjected to the average motion of all their neighbors, but simultaneously disrupt the flow of smaller neighboring particles. These smaller particles need to navigate around their larger particles' neighbors. We verify this by measuring the non-affine displacements and D_{\min}^2 in the immediate vicinity of all particles, and separately based on a particle's size. We found this effect to be visible for the studied particle size distributions. Furthermore, we found that local non-affine behaviour (D_{\min}^2) is strongly affected by the polydispersity of its constituent particles' size distribution, with the size ratio between particles playing a minor role in comparison. On the other hand the global non-affine motion ($\Delta \vec{r}_{\text{NA}}$) is not significantly influenced by the particle polydispersity, suggesting that enhanced nonaffine motion for smaller particles is balanced by a decreased nonaffine motion for the larger particles. Both types of nonaffine motion are strongly enhanced in the presence of large particles. As noted in prior work, this implies that mixing can be enhanced in these mixtures of particle sizes [32]. The research presented in Chapter 3, helps better understand how granular flows are affected by the polydispersity of their constituent particles.

We believe that the experimental procedure developed here can be of further use in the future. One option is to fabricate a few more particles and build particle distributions with larger size ratios and higher polydispersity. Additionally, using the currently available particles, it is possible to study the flow of disks through more flow configurations, such as the “X” and “T” configurations, with a variety of ways in which the plungers can be placed. Additionally the flow of non circular shapes, like ellipses, rods, or concave shapes, can be easily done with the resources available, and are of great interest to the field of granular flow[137, 186–190]. If resources are available adding force sensors to the plunger would add another dimension of available information. In a similar manner using photoelastic disks would enable us to probe to complex contact network during the flow, and how non-conventional flow geometries apply stress into the system, the mechanism and force chains by which these stress is spread through out the system and how polydispersity can affect further affect these force chains. Fabricating photoelastic disks can be done either by cutting out the shapes out of a sheet of photoelastic material, or casting the particles out of urethane [191], using either of this methods it is possible to select samples appropriate for the load the particles will have to bear. Current limitations for this method are the need to achieve a mirrored surface below the particles such that the light is cross polarized and the diffraction patterns can be recorded and measures. Additionally, post-processing of these images needs very high resolution and additional numerical calculations if a better analysis of the pressure and internal forces and stress fields in the particles is desired. However, a simpler image intensity analysis can be done to get information about the distribution of the average stress and force chains in the samples. If possible, using force sensors and the above described photoelastic materials method would be a good next step, as probing further the forces and stresses in the system can further help understand the non-affine behavior of the particle flow.

The last project in this dissertation, Chapter 4, focuses on gravity driven granular

flow through a bottleneck for cohesive particles. We were able to verify that stronger cohesive strengths lead to higher clogging probabilities, while higher gravitational forces facilitate the flow of particles and decreases clogs. Furthermore we were able to use the cohesive length scale, analogous to the capillary length of surface tension forces, to accurately predict the behaviour of the hopper, and managed to successfully collapse the clogging probability using this cohesive length scale. We were able to identify two regimes of low and high cohesion. The former is characterized by weakly reinforcing the clogging mechanisms, with the frequency of clogs still being determined mainly by the particle to hopper opening size ratio. For high cohesion the clogging and amount of particles remaining in a clog, are dependent primarily on the cohesion length scale. We then assert that when cohesion is strong between particles, the relevant length scale to predict clogging can no longer be obtained through the particle diameter, but instead a cohesive length scale needs to be taken into account.

Further simulations can probe the effect the hopper exit angle has on the flow, since depletion interactions in the proximity to the exit are non trivial. On the other hand exploring the effect that polydispersity has on these systems is also of great interest, due to the effect differently sized particles have on the formation of structures. Finally, the software used for these hopper simulations is robust and versatile enough to be used to explore many hopper systems, and the version used in this dissertation is based on previous versions used to probe the effect of particle softness[52, 101]. As such expanding the software to be used probing cohesion forces others than depletion, or using droplets that have different properties.

To summarize my dissertation and its impact, we have shown the effect polydispersity has on plastic deformations of glassy materials and granular systems. In both cases higher polydispersity lead to changes in the properties of the materials; for compressed arrays the material becomes easier to deform, while for granular flows, local non-affine rearrangement and particle motion are affected by polydispersity. Both

these projects can help predict the behavior of samples under similar conditions. On the other hand we studied the effect of attractive forces on both crystals and granular hopper flow, and have characterized both systems based on the strength of cohesive forces in the systems. In both cases, cohesive forces are shown to be important parameters that govern the behavior of the systems, and can be used to predict the force needed to deform the system, for crystalline arrays, and predict the clogging probability and avalanche size of cohesive hoppers. Identifying these key parameters, such as polydispersity and cohesiveness, has been shown to be important in predicting the behavior of granular materials and systems.

Appendix A

Effect of polydispersity on the rotation of hard disks

As mentioned in Chapter 3, in this appendix we analyze the change in orientation of the acrylic disks as these are pushed through the canal. We use the same methods described in Chapter 3, where we measure the orientation angle of the disk $\theta(t)$ at a given time, and compare it to the angle of the same disk a Δt later, $\theta(t + \Delta t)$. We then take the absolute value of this difference:

$$|\Delta\theta| = |\theta(t + \Delta t) - \theta(t)|.$$

For this Appendix we have chosen to keep using $\Delta t = 5\text{s}$ as in Ch. 3 Sec. 3.3.2, and similarly have parsed our data in bins using the same widths as before, and following the same methodology.

First we analyze the change in angle for bidisperse and T4 distributions. In Fig. A.1(a,b), we have plotted the $|\Delta\theta|$ against displacement, which shows no clear relation between $|\Delta\theta|$ and the displacement of the particles, for particles in the center zone (the central square as indicated by Fig. 3.2) and for particles outside this region.

On the other hand, we can see for Figs. A.1(c-f), there is a positive relation

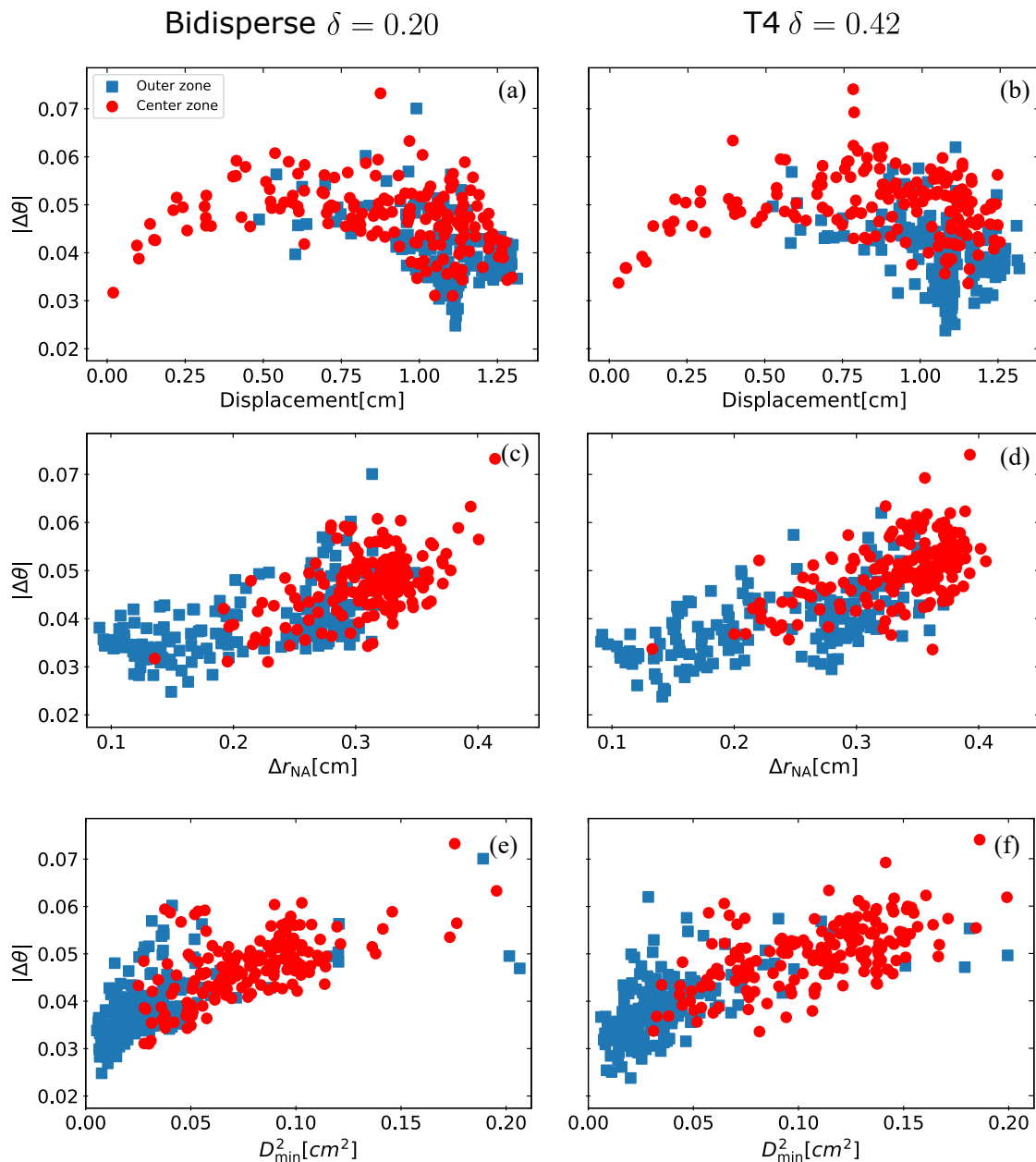


Figure A.1: Figures showing the correlation between averaged $|\Delta\theta|$ against different quantities measured in the flow for the bidisperse size distribution (left column panels) and the T4 size distribution (right panels). From top to bottom, (a,b) display the correlation between $|\Delta\theta|$ and the displacement of the particles, (c,d) show $|\Delta\theta|$ vs nonaffine displacement, and (e,f) show $|\Delta\theta|$ vs D_{\min}^2 . The red data points correspond to the bins in the central zone as outlined by Fig. 3.2, while the blue data points correspond to all bins outside this area. Regarding the displacements (a,b), there does not seem to be a strong correlation between change in orientation of the particles and the magnitude of the displacement. However for both Δr_{NA} and D_{\min}^2 there seems to be a degree of positive correlation with $|\Delta\theta|$.

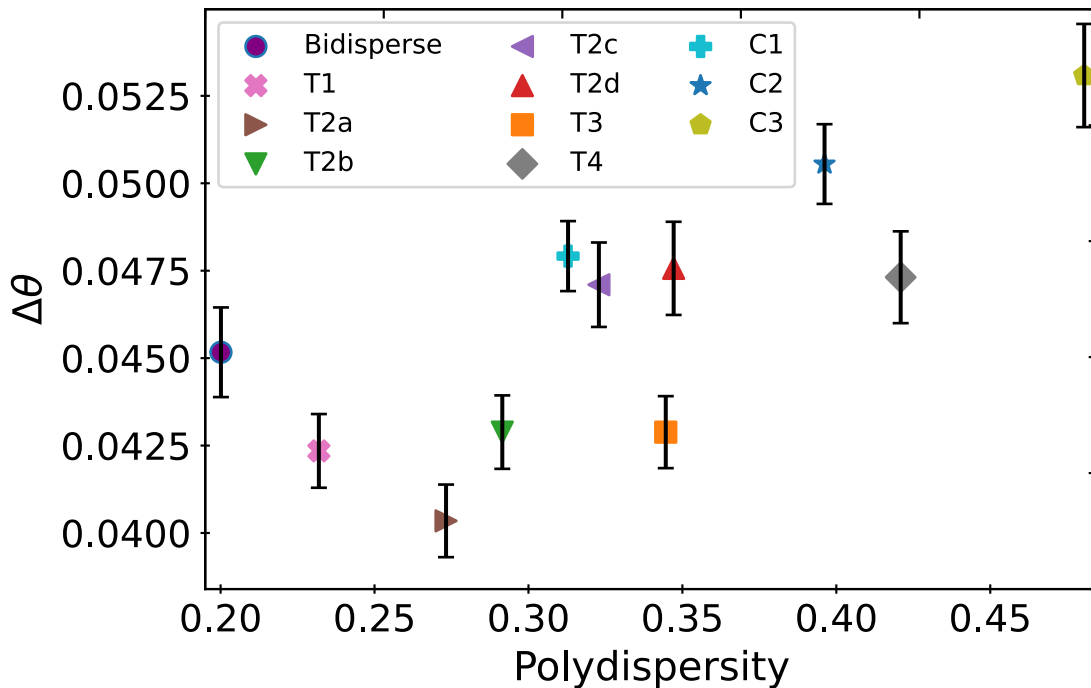


Figure A.2: $|\Delta\theta|$, as a function of the polydispersity for each size distribution. We can see that there is no clear relation between $|\Delta\theta|$ and polydispersity, averaging to a value of 0.046.

between $|\Delta\theta|$ and both Δr_{NA} and D_{min}^2 , with particles in the central region having on average larger $|\Delta\theta|$ values. Similar behavior was observed for the other distributions not shown here.

Next, we study the relation between polydispersity and $|\Delta\theta|$, and as done in Chapter 3, we averaged $|\Delta\theta|$ in the center zone and plotted it against each distributions' polydispersity, as seen in Fig. A.2. Similarly to what was observed for Δr_{NA} , there does not seem to be clear a relation between $|\Delta\theta|$ and polydispersity.

Bibliography

- [1] Richard A. L. Jones. Soft Condensed Matter. *European Journal of Physics*, 23 (6):652, November 2002. ISSN 0143-0807. doi: 10.1088/0143-0807/23/6/703. URL <https://dx.doi.org/10.1088/0143-0807/23/6/703>.
- [2] Eric Weeks. Soft jammed materials. pages 2–1. January 2007.
- [3] Kurt Binder and Walter Kob. *Glassy Materials and Disordered Solids*. WORLD SCIENTIFIC, revised edition, 2011. doi: 10.1142/7300. URL <https://www.worldscientific.com/doi/abs/10.1142/7300>. eprint: <https://www.worldscientific.com/doi/pdf/10.1142/7300>.
- [4] A. K. Guber, W. J. Rawls, E. V. Shein, and Y. A. Pachepsky. Effect of soil aggregate size distribution on water retention. *Soil Sci.*, 168(4):223–233, April 2003. ISSN 0038-075X, 1538-9243. doi: 10.1097/01.ss.0000064887.94869.d3. URL https://journals.lww.com/soilsci/abstract/2003/04000/effect_of_soil_aggregate_size_distribution_on.1.aspx.
- [5] Justin C. Burton, Jason M. Amundson, Ryan Cassotto, Chin-Chang Kuo, and Michael Dennin. Quantifying flow and stress in ice mélange, the world’s largest granular material. *Proceedings of the National Academy of Sciences*, 115(20): 5105–5110, May 2018. doi: 10.1073/pnas.1715136115. URL <https://www.pnas.org/doi/10.1073/pnas.1715136115>.

- [6] Gladstone, Phillips, and Sparks. Experiments on bidisperse, constant-volume gravity currents: propagation and sediment deposition. *Sedimentology*, 45(5):833–843, 1998. ISSN 1365-3091. doi: 10.1046/j.1365-3091.1998.00189.x. URL <https://onlinelibrary.wiley.com/doi/abs/10.1046/j.1365-3091.1998.00189.x>.
- [7] F Rosquoët, A Alexis, A Khelidj, and A Phelipot. Experimental study of cement grout: Rheological behavior and sedimentation. *Cement and Concrete Research*, 33(5):713–722, May 2003. ISSN 0008-8846. doi: 10.1016/S0008-8846(02)01036-0. URL <https://www.sciencedirect.com/science/article/pii/S0008884602010360>.
- [8] Roberto Arévalo and Iker Zuriguel. Clogging of granular materials in silos: effect of gravity and outlet size. *Soft Matter*, 12(1):123–130, 2016. doi: 10.1039/C5SM01599E. URL <https://pubs.rsc.org/en/content/articlelanding/2016/sm/c5sm01599e>. Publisher: Royal Society of Chemistry.
- [9] R. L. Brown and J. C. Richards. Two- and Three-Dimensional Flow of Grains through Apertures. *Nature*, 182(4635):600–601, August 1958. ISSN 1476-4687. doi: 10.1038/182600c0. URL <https://www.nature.com/articles/182600c0>. Publisher: Nature Publishing Group.
- [10] F. Scheffold and R. Cerbino. New trends in light scattering. *Current Opinion in Colloid & Interface Science*, 12(1):50–57, February 2007. ISSN 1359-0294. doi: 10.1016/j.cocis.2007.03.005. URL <https://www.sciencedirect.com/science/article/pii/S1359029407000209>.
- [11] Gary L. Hunter and Eric R. Weeks. The physics of the colloidal glass transition. *Rep. Prog. Phys.*, 75(6):066501, May 2012. ISSN 0034-4885. doi: 10.1088/0034-4885/75/6/066501.

- [12] P. N. Pusey and W. van Megen. Phase behaviour of concentrated suspensions of nearly hard colloidal spheres. *Nature*, 320(6060):340–342, March 1986. ISSN 1476-4687. doi: 10.1038/320340a0.
- [13] P. N. Pusey and W. van Megen. Observation of a glass transition in suspensions of spherical colloidal particles. *Phys. Rev. Lett.*, 59(18):2083–2086, November 1987. doi: 10.1103/PhysRevLett.59.2083.
- [14] Dirk G. A. L. Aarts, Matthias Schmidt, and Henk N. W. Lekkerkerker. Direct Visual Observation of Thermal Capillary Waves. *Science*, 304(5672):847–850, May 2004. doi: 10.1126/science.1097116. URL <https://www.science.org/doi/10.1126/science.1097116>. Publisher: American Association for the Advancement of Science.
- [15] Ernst-Joachim Donth. *The Glass Transition: Relaxation Dynamics in Liquids and Disordered Materials*. Springer Berlin, Heidelberg, 2001. ISBN 978-3-540-41801-6.
- [16] Eric R. Weeks. Introduction to the colloidal glass transition. *ACS Macro Lett.*, 6(1):27–34, January 2017. doi: 10.1021/acsmacrolett.6b00826.
- [17] Solomon Barkley, Eric R. Weeks, and Kari Dalnoki-Veress. Snap-off production of monodisperse droplets. *Eur. Phys. J. E*, 38(12):138, December 2015. ISSN 1292-8941, 1292-895X. doi: 10.1140/epje/i2015-15138-8. URL <http://link.springer.com/10.1140/epje/i2015-15138-8>.
- [18] Jean-Christophe Ono-dit Biot, Tanel Lorand, and Kari Dalnoki-Veress. Continuum Model Applied to Granular Analogs of Droplets and Puddles. *Phys. Rev. Lett.*, 125(22):228001, November 2020. ISSN 0031-9007. doi: 10.1103/PhysRevLett.125.228001. URL <https://www.webofscience.com/wos/alldb/summary/a23222f4-37a9-49ff-98cb-c764a24b479c-6bf6fb52/>

date-descending/1(overlay:export/ris). Place: College Pk Publisher: Amer Physical Soc WOS:000591812900020.

- [19] Jean-Christophe Ono-dit-Biot, Pierre Soulard, Solomon Barkley, Eric R. Weeks, Thomas Salez, Elie Raphaël, and Kari Dalnoki-Veress. Mechanical properties of 2D aggregates of oil droplets as model mono-crystals. *Soft Matter*, 17(5): 1194–1201, February 2021. ISSN 1744-6848. doi: 10.1039/D0SM01165G.
- [20] Jean-Christophe Ono-dit-Biot, Pierre Soulard, Solomon Barkley, Eric R. Weeks, Thomas Salez, Elie Raphaël, and Kari Dalnoki-Veress. Rearrangement of two dimensional aggregates of droplets under compression: signatures of the energy landscape from crystal to glass. *Phys. Rev. Research*, 2(2):023070, April 2020. doi: 10.1103/PhysRevResearch.2.023070.
- [21] Pablo Eduardo Illing, Jean-Christophe Ono-dit Biot, Kari Dalnoki-Veress, and Eric R. Weeks. Compression and fracture of ordered and disordered droplet rafts. *Phys. Rev. E*, 109(1):014610, January 2024. doi: 10.1103/PhysRevE.109.014610. URL <https://link.aps.org/doi/10.1103/PhysRevE.109.014610>.
- [22] Vincent Mansard, Annie Colin, Pinaki Chaudhuri, and Lydéric Bocquet. A molecular dynamics study of non-local effects in the flow of soft jammed particles. *Soft Matter*, 9(31):7489–7500, July 2013. ISSN 1744-6848. doi: 10.1039/C3SM50847A. URL <https://pubs.rsc.org/en/content/articlelanding/2013/sm/c3sm50847a>. Publisher: The Royal Society of Chemistry.
- [23] Axelle Amon, Van Bau Nguyen, Ary Bruand, Jérôme Crassous, and Eric Clément. Hot Spots in an Athermal System. *Physical Review Letters*, 108(13):135502, March 2012. doi: 10.1103/PhysRevLett.108.135502. URL <https://link.aps.org/doi/10.1103/PhysRevLett.108.135502>. Publisher: American Physical Society.

- [24] Lydéric Bocquet, Annie Colin, and Armand Ajdari. Kinetic Theory of Plastic Flow in Soft Glassy Materials. *Physical Review Letters*, 103(3):036001, July 2009. doi: 10.1103/PhysRevLett.103.036001. URL <https://link.aps.org/doi/10.1103/PhysRevLett.103.036001>. Publisher: American Physical Society.
- [25] Ken Kamrin and Georg Koval. Nonlocal Constitutive Relation for Steady Granular Flow. *Physical Review Letters*, 108(17):178301, April 2012. doi: 10.1103/PhysRevLett.108.178301. URL <https://link.aps.org/doi/10.1103/PhysRevLett.108.178301>. Publisher: American Physical Society.
- [26] J. Goyon, A. Colin, G. Ovarlez, A. Ajdari, and L. Bocquet. Spatial cooperativity in soft glassy flows. *Nature*, 454(7200):84–87, July 2008. ISSN 1476-4687. doi: 10.1038/nature07026. URL <https://www.nature.com/articles/nature07026>. Publisher: Nature Publishing Group.
- [27] A. Tanguy, F. Leonforte, and J. L. Barrat. Plastic response of a 2d lennard-jones amorphous solid: Detailed analysis of the local rearrangements at very slow strain rate. *The European Physical Journal E*, 20(3):355–364, 2006. ISSN 1292-895X. doi: 10.1140/epje/i2006-10024-2. URL <https://doi.org/10.1140/epje/i2006-10024-2>.
- [28] M. L. Falk and J. S. Langer. Dynamics of viscoplastic deformation in amorphous solids. *Phys. Rev. E*, 57(6):7192–7205, June 1998. doi: 10.1103/PhysRevE.57.7192. URL <https://link.aps.org/doi/10.1103/PhysRevE.57.7192>. Publisher: American Physical Society.
- [29] Craig E. Maloney and Anael Lemaitre. Amorphous systems in athermal, quasistatic shear. *PHYSICAL REVIEW E*, 74(1):016118, July 2006. ISSN 1539-3755, 1550-2376. doi: 10.1103/PhysRevE.74.016118. URL <https://doi.org/10.1103/PhysRevE.74.016118>.

[//journals.aps.org/pre/abstract/10.1103/PhysRevE.74.016118](https://journals.aps.org/pre/abstract/10.1103/PhysRevE.74.016118). Num Pages: 22 Patent Number: 2 Place: College Pk Publisher: Amer Physical Soc Web of Science ID: WOS:000239425700020.

- [30] G. Mollon and J. Zhao. The influence of particle shape on granular Hopper flow. *AIP Conference Proceedings*, 1542(1):690–693, June 2013. ISSN 0094-243X. doi: 10.1063/1.4812025. URL <https://doi.org/10.1063/1.4812025>.
- [31] M. D. Jiang, Z. X. Yang, D. Barreto, and Y. H. Xie. The influence of particle-size distribution on critical state behavior of spherical and non-spherical particle assemblies. *Granular Matter*, 20(4):80, November 2018. ISSN 1434-7636. doi: 10.1007/s10035-018-0850-x. URL <https://doi.org/10.1007/s10035-018-0850-x>.
- [32] Yonglun Jiang, Daniel M. Sussman, and Eric R. Weeks. Effects of polydispersity on the plastic behaviors of dense two-dimensional granular systems under shear. *Phys. Rev. E*, 108(5):054605, November 2023. doi: 10.1103/PhysRevE.108.054605. URL <https://link.aps.org/doi/10.1103/PhysRevE.108.054605>.
- [33] Nasre-Dine Ahfir, Ahmed Hammadi, Abdellah Alem, HuaQing Wang, Gilbert Le Bras, and Tariq Ouahbi. Porous media grain size distribution and hydrodynamic forces effects on transport and deposition of suspended particles. *Journal of Environmental Sciences*, 53:161–172, March 2017. ISSN 1001-0742. doi: 10.1016/j.jes.2016.01.032. URL <https://www.sciencedirect.com/science/article/pii/S1001074216301656>.
- [34] R. M. Dorrell, A. J. Hogg, and D. Pritchard. Polydisperse suspensions: Erosion, deposition, and flow capacity. *Journal of Geophysical Research: Earth Surface*, 118(3):1939–1955, 2013. ISSN 2169-9011. doi: 10.1002/jgrf.20129. URL <https://onlinelibrary.wiley.com/doi/abs/10.1002/jgrf.20129>.

- [35] B. T. Werner. Eolian dunes: Computer simulations and attractor interpretation. *Geology*, 23(12):1107–1110, December 1995. ISSN 0091-7613. doi: 10.1130/0091-7613(1995)023<1107:EDCSAA>2.3.CO;2. URL [https://doi.org/10.1130/0091-7613\(1995\)023<1107:EDCSAA>2.3.CO;2](https://doi.org/10.1130/0091-7613(1995)023<1107:EDCSAA>2.3.CO;2).
- [36] Heinrich M. Jaeger, Sidney R. Nagel, and Robert P. Behringer. Granular solids, liquids, and gases. *Reviews of Modern Physics*, 68(4):1259–1273, October 1996. doi: 10.1103/RevModPhys.68.1259. URL <https://link.aps.org/doi/10.1103/RevModPhys.68.1259>. Publisher: American Physical Society.
- [37] Olivier Pouliquen and Yoel Forterre. A non-local rheology for dense granular flows. *Philosophical Transactions of the Royal Society A: Mathematical, Physical and Engineering Sciences*, 367(1909):5091–5107, December 2009. doi: 10.1098/rsta.2009.0171. URL <https://royalsocietypublishing.org/doi/10.1098/rsta.2009.0171>. Publisher: Royal Society.
- [38] Yoël Forterre and Olivier Pouliquen. Flows of Dense Granular Media. *Annual Review of Fluid Mechanics*, 40(Volume 40, 2008):1–24, January 2008. ISSN 0066-4189, 1545-4479. doi: 10.1146/annurev.fluid.40.111406.102142. URL <https://www.annualreviews.org/content/journals/10.1146/annurev.fluid.40.111406.102142>. Publisher: Annual Reviews.
- [39] W. Edwards. Deming and Arnon L. Mehring. The Gravitational Flow of Fertilizers and Other Comminuted Solids. *Industrial & Engineering Chemistry*, 21(7):661–665, July 1929. ISSN 0019-7866. doi: 10.1021/ie50235a013. URL <https://doi.org/10.1021/ie50235a013>. Publisher: American Chemical Society.
- [40] F. C. Franklin and L. N. Johanson. Flow of granular material through a circular orifice. *Chemical Engineering Science*, 4(3):119–129, June 1955.

ISSN 0009-2509. doi: 10.1016/0009-2509(55)80003-6. URL <https://www.sciencedirect.com/science/article/pii/0009250955800036>.

- [41] R. T. Fowler and J. R. Glastonbury. The flow of granular solids through orifices. *Chemical Engineering Science*, 10(3):150–156, May 1959. ISSN 0009-2509. doi: 10.1016/0009-2509(59)80042-7. URL <https://www.sciencedirect.com/science/article/pii/0009250959800427>.
- [42] W. A. Beverloo, H. A. Leniger, and J. van de Velde. The flow of granular solids through orifices. *Chemical Engineering Science*, 15(3):260–269, September 1961. ISSN 0009-2509. doi: 10.1016/0009-2509(61)85030-6. URL <https://www.sciencedirect.com/science/article/pii/0009250961850306>.
- [43] A. W. Jenike. Quantitative design of mass-flow bins. *Powder Technology*, 1(4):237–244, December 1967. ISSN 0032-5910. doi: 10.1016/0032-5910(67)80042-1. URL <https://www.sciencedirect.com/science/article/pii/0032591067800421>.
- [44] R. M. Nedderman. *Statics and Kinematics of Granular Materials*. Cambridge University Press, Cambridge, 1992. ISBN 978-0-521-40435-8. doi: 10.1017/CBO9780511600043. URL <https://www.cambridge.org/core/books/statics-and-kinematics-of-granular-materials/3D238E75C21D9B8B99302744D6200F8C>.
- [45] Iker Zuriguel, Daniel Ricardo Parisi, Raúl Cruz Hidalgo, Celia Lozano, Alvaro Janda, Paula Alejandra Gago, Juan Pablo Peralta, Luis Miguel Ferrer, Luis Ariel Pugnaroni, Eric Clément, Diego Maza, Ignacio Pagonabarraga, and Angel Garcimartín. Clogging transition of many-particle systems flowing through bottlenecks. *Sci Rep*, 4(1):7324, December 2014. ISSN 2045-

2322. doi: 10.1038/srep07324. URL <https://www.nature.com/articles/srep07324>. Number: 1 Publisher: Nature Publishing Group.
- [46] Kirsten Harth, Jing Wang, Tamás Börzsönyi, and Ralf Stannarius. Intermittent flow and transient congestions of soft spheres passing narrow orifices. *Soft Matter*, 16(34):8013–8023, September 2020. ISSN 1744-6848. doi: 10.1039/D0SM00938E. URL <https://pubs.rsc.org/en/content/articlelanding/2020/sm/d0sm00938e>. Publisher: The Royal Society of Chemistry.
- [47] A. Janda, I. Zuriguel, A. Garcimartín, L. A. Pugnaloni, and D. Maza. Jamming and critical outlet size in the discharge of a two-dimensional silo. *EPL*, 84(4):44002, November 2008. ISSN 0295-5075. doi: 10.1209/0295-5075/84/44002. URL <https://dx.doi.org/10.1209/0295-5075/84/44002>.
- [48] C. C. Thomas and D. J. Durian. Fraction of Clogging Configurations Sampled by Granular Hopper Flow. *Phys. Rev. Lett.*, 114(17):178001, April 2015. doi: 10.1103/PhysRevLett.114.178001.
- [49] Ran Tao, Madelyn Wilson, and Eric R. Weeks. Soft particle clogging in two-dimensional hoppers. *Phys. Rev. E*, 104(4):044909, October 2021. doi: 10.1103/PhysRevE.104.044909.
- [50] Ahmed Ashour, Torsten Trittel, Tamás Börzsönyi, and Ralf Stannarius. Silo outflow of soft frictionless spheres. *Phys. Rev. Fluids*, 2(12):123302, December 2017. doi: 10.1103/PhysRevFluids.2.123302. URL <https://link.aps.org/doi/10.1103/PhysRevFluids.2.123302>. Publisher: American Physical Society.
- [51] A. Ashour, S. Wegner, T. Trittel, T. Börzsönyi, and R. Stannarius. Outflow and clogging of shape-anisotropic grains in hoppers with small apertures. *Soft Matter*, 13(2):402–414, January 2017. ISSN 1744-6848. doi: 10.1039/C6SM02374F.

- [52] Xia Hong, Meghan Kohne, Mia Morrell, Haoran Wang, and Eric R. Weeks. Clogging of soft particles in two-dimensional hoppers. *Phys. Rev. E*, 96(6): 062605, December 2017. doi: 10.1103/PhysRevE.96.062605.
- [53] A. Castellanos. The relationship between attractive interparticle forces and bulk behaviour in dry and uncharged fine powders. *Advances in Physics*, 54(4): 263–376, June 2005. ISSN 0001-8732. doi: 10.1080/17461390500402657. URL <https://doi.org/10.1080/17461390500402657>. Publisher: Taylor & Francis _eprint: <https://doi.org/10.1080/17461390500402657>.
- [54] S. Herminghaus *. Dynamics of wet granular matter. *Advances in Physics*, 54(3):221–261, May 2005. ISSN 0001-8732. doi: 10.1080/00018730500167855. URL <https://doi.org/10.1080/00018730500167855>. Publisher: Taylor & Francis _eprint: <https://doi.org/10.1080/00018730500167855>.
- [55] AbdulMobeen N. Faqih, Albert W. Alexander, Fernando J. Muzzio, and M. Silvina Tomassone. A method for predicting hopper flow characteristics of pharmaceutical powders. *Chemical Engineering Science*, 62(5):1536–1542, March 2007. ISSN 0009-2509. doi: 10.1016/j.ces.2006.06.027. URL <https://www.sciencedirect.com/science/article/pii/S0009250906007226>.
- [56] Ahmed Jarray, Vanessa Magnanimo, and Stefan Luding. Wet granular flow control through liquid induced cohesion. *Powder Technology*, 341:126–139, January 2019. ISSN 0032-5910. doi: 10.1016/j.powtec.2018.02.045. URL <https://research.wur.nl/en/publications/wet-granular-flow-control-through-liquid-induced-cohesion>. Publisher: Elsevier.
- [57] Corey S. O’Hern, Leonardo E. Silbert, Andrea J. Liu, and Sidney R. Nagel.

- Jamming at zero temperature and zero applied stress: the epitome of disorder. *Phys. Rev. E*, 68(1):011306, July 2003. doi: 10.1103/PhysRevE.68.011306.
- [58] William Lawrence Bragg and J. F. Nye. A dynamical model of a crystal structure. *Proc. Roy. Soc. London A*, 190(1023):474–481, September 1947. doi: 10.1098/rspa.1947.0089.
- [59] William Lawrence Bragg and W. M. Lomer. A dynamical model of a crystal structure. II. *Proc. Roy. Soc. London A*, 196(1045):171–181, March 1949. doi: 10.1098/rspa.1949.0022.
- [60] Huijun Zhang and Yilong Han. Compression-induced polycrystal-glass transition in binary crystals. *Phys. Rev. X*, 8(4):041023, November 2018. doi: 10.1103/PhysRevX.8.041023.
- [61] Peter Yunker, Zexin Zhang, and A. G. Yodh. Observation of the disorder-induced crystal-to-glass transition. *Phys. Rev. Lett.*, 104(1):015701, January 2010. doi: 10.1103/PhysRevLett.104.015701.
- [62] Carl P. Goodrich, Andrea J. Liu, and Sidney R. Nagel. Solids between the mechanical extremes of order and disorder. *Nature Phys*, 10(8):578–581, August 2014. ISSN 1745-2481. doi: 10.1038/nphys3006.
- [63] Nathan C. Keim and Paulo E. Arratia. Role of disorder in finite-amplitude shear of a 2D jammed material. *Soft Matter*, 11(8):1539–1546, February 2015. ISSN 1744-6848. doi: 10.1039/C4SM02446J.
- [64] Patrick Charbonneau, Eric I. Corwin, Lin Fu, Georgios Tsekenis, and Michael van der Naald. Glassy, Gardner-like phenomenology in minimally polydisperse crystalline systems. *Phys. Rev. E*, 99(2):020901, February 2019. doi: 10.1103/PhysRevE.99.020901.

- [65] Ludovic Berthier and Thomas A. Witten. Glass transition of dense fluids of hard and compressible spheres. *Phys. Rev. E*, 80(2):021502, August 2009. doi: 10.1103/PhysRevE.80.021502.
- [66] Bo Li, Di Zhou, and Yilong Han. Assembly and phase transitions of colloidal crystals. *Nat. Rev. Mater.*, 1(2):1–13, January 2016. ISSN 2058-8437. doi: 10.1038/natrevmats.2015.11.
- [67] Romain Mari, Florent Krzakala, and Jorge Kurchan. Jamming versus glass transitions. *Phys. Rev. Lett.*, 103(2):025701, July 2009. doi: 10.1103/PhysRevLett.103.025701.
- [68] Dapeng Bi, Jie Zhang, Bulbul Chakraborty, and R. P. Behringer. Jamming by shear. *Nature*, 480(7377):355–358, December 2011. ISSN 1476-4687. doi: 10.1038/nature10667.
- [69] Matthias Grob, Claus Heussinger, and Annette Zippelius. Jamming of frictional particles: A nonequilibrium first-order phase transition. *Phys. Rev. E*, 89(5):050201, May 2014. doi: 10.1103/PhysRevE.89.050201.
- [70] Bernd Illing, Sebastian Fritschi, Herbert Kaiser, Christian L. Klix, Georg Maret, and Peter Keim. Mermin–Wagner fluctuations in 2D amorphous solids. *Proc. Nat. Acad. Sci.*, 114(8):1856–1861, February 2017. doi: 10.1073/pnas.1612964114.
- [71] Ivane Jorjadze, Lea-Laetitia Pontani, Katherine A. Newhall, and Jasna Brujić. Attractive emulsion droplets probe the phase diagram of jammed granular matter. *Proc. Nat. Acad. Sci.*, 108(11):4286–4291, March 2011. doi: 10.1073/pnas.1017716108.
- [72] Dale W. Schaefer and Bruce J. Ackerson. Melting of colloidal crystals. *Phys.*

- Rev. Lett.*, 35(21):1448–1451, November 1975. doi: 10.1103/PhysRevLett.35.1448.
- [73] Ziren Wang, Feng Wang, Yi Peng, Zhongyu Zheng, and Yilong Han. Imaging the homogeneous nucleation during the melting of superheated colloidal crystals. *Science*, 338(6103):87–90, October 2012. ISSN 1095-9203. doi: 10.1126/science.1224763.
- [74] A. M. Alsayed, M. F. Islam, J. Zhang, P. J. Collings, and A. G. Yodh. Premelting at defects within bulk colloidal crystals. *Science*, 309(5738):1207–1210, August 2005. ISSN 1095-9203. doi: 10.1126/science.1112399.
- [75] Takashi Hayashi and Richard W. Carthew. Surface mechanics mediate pattern formation in the developing retina. *Nature*, 431(7009):647–652, October 2004. ISSN 1476-4687. doi: 10.1038/nature02952.
- [76] David Gonzalez-Rodriguez, Karine Guevorkian, Stéphane Douezan, and Françoise Brochard-Wyart. Soft matter models of developing tissues and tumors. *Science*, 338(6109):910–917, November 2012. ISSN 1095-9203. doi: 10.1126/science.1226418.
- [77] Lea-Laetitia Pontani, Ivane Jorjadze, Virgile Viasnoff, and Jasna Brujic. Biomimetic emulsions reveal the effect of mechanical forces on cell–cell adhesion. *Proceedings of the National Academy of Sciences*, 109(25):9839–9844, June 2012. doi: 10.1073/pnas.1201499109.
- [78] Stéphane Douezan and Françoise Brochard-Wyart. Active diffusion-limited aggregation of cells. *Soft Matter*, 8(3):784–788, December 2011. ISSN 1744-6848. doi: 10.1039/C1SM06399E.
- [79] Ehsan Irani, Pinaki Chaudhuri, and Claus Heussinger. Impact of attractive

- interactions on the rheology of dense athermal particles. *Phys. Rev. Lett.*, 112(18):188303, May 2014. doi: 10.1103/PhysRevLett.112.188303.
- [80] Daniel Bonn, Morton M. Denn, Ludovic Berthier, Thibaut Divoux, and Sébastien Manneville. Yield stress materials in soft condensed matter. *Rev. Mod. Phys.*, 89(3):035005, August 2017. doi: 10.1103/RevModPhys.89.035005.
- [81] Iaroslava Golovkova, Lorraine Montel, Elie Wandersman, Thibault Bertrand, Alexis Michel Prevost, and Lea-Laetitia Pontani. Depletion attraction impairs the plasticity of emulsions flowing in a constriction. *Soft Matter*, 16(13):3294–3302, April 2020. ISSN 1744-6848. doi: 10.1039/C9SM02343G.
- [82] D. A Edwards and D. T Wasan. Foam dilatational rheology: I. dilatational viscosity. *Journal of Colloid and Interface Science*, 139(2):479–487, October 1990. ISSN 0021-9797. doi: 10.1016/0021-9797(90)90120-D.
- [83] T. G. Mason, J. Bibette, and D. A. Weitz. Yielding and flow of monodisperse emulsions. *J. Colloid Interface Sci.*, 179(2):439–448, May 1996. ISSN 0021-9797. doi: 10.1006/jcis.1996.0235.
- [84] T. G. Mason, J. Bibette, and D. A. Weitz. Elasticity of compressed emulsions. *Phys. Rev. Lett.*, 75(10):2051–2054, September 1995. doi: 10.1103/PhysRevLett.75.2051.
- [85] P. Coussot, J. S. Raynaud, F. Bertrand, P. Moucheront, J. P. Guilbaud, H. T. Huynh, S. Jarny, and D. Lesueur. Coexistence of liquid and solid phases in flowing soft-glassy materials. *Phys. Rev. Lett.*, 88(21):218301, May 2002. doi: 10.1103/PhysRevLett.88.218301.
- [86] Alexandre Nicolas, Ezequiel E. Ferrero, Kirsten Martens, and Jean-Louis Barrat. Deformation and flow of amorphous solids: insights from elastoplastic mod-

- els. *Rev. Mod. Phys.*, 90(4):045006, December 2018. doi: 10.1103/RevModPhys.90.045006.
- [87] D. J. Durian. Foam mechanics at the bubble scale. *Phys. Rev. Lett.*, 75(26):4780–4783, December 1995. doi: 10.1103/PhysRevLett.75.4780.
- [88] D. J. Durian, D. A. Weitz, and D. J. Pine. Scaling behavior in shaving cream. *Phys. Rev. A*, 44(12):R7902–R7905, December 1991. doi: 10.1103/PhysRevA.44.R7902.
- [89] Stig E Friberg. Foams from non-aqueous systems. *Current Opinion Colloid Interface Sci.*, 15(5):359–364, October 2010. ISSN 1359-0294. doi: 10.1016/j.cocis.2010.05.011.
- [90] Hua Tong, Peng Tan, and Ning Xu. From crystals to disordered crystals: a hidden order-disorder transition. *Sci Rep*, 5(1):15378, October 2015. ISSN 2045-2322. doi: 10.1038/srep15378.
- [91] Peter Schall, Itai Cohen, David A. Weitz, and Frans Spaepen. Visualization of dislocation dynamics in colloidal crystals. *Science*, 305(5692):1944–1948, September 2004. doi: 10.1126/science.1102186.
- [92] Daniel Vecchiolla and Sibani Lisa Biswal. Dislocation mechanisms in the plastic deformation of monodisperse wet foams within an expansion–contraction microfluidic geometry. *Soft Matter*, 15(30):6207–6223, July 2019. ISSN 1744-6848. doi: 10.1039/C9SM00477G.
- [93] Jeetu S. Babu, Chandana Mondal, Surajit Sengupta, and Smarajit Karmakar. Excess vibrational density of states and the brittle to ductile transition in crystalline and amorphous solids. *Soft Matter*, 12(4):1210–1218, January 2016. ISSN 1744-6848. doi: 10.1039/C5SM02200B.

- [94] Hideyuki Mizuno, Stefano Mossa, and Jean-Louis Barrat. Elastic heterogeneity, vibrational states, and thermal conductivity across an amorphisation transition. *Europhys. Lett.*, 104(5):56001, December 2013. ISSN 0295-5075. doi: 10.1209/0295-5075/104/56001.
- [95] Misaki Ozawa, Ludovic Berthier, Giulio Biroli, and Gilles Tarjus. Role of fluctuations in the yielding transition of two-dimensional glasses. *Phys. Rev. Research*, 2(2):023203, May 2020. doi: 10.1103/PhysRevResearch.2.023203.
- [96] M. Hanifpour, N. Francois, S. M. Vaez Allaei, T. Senden, and M. Saadatfar. Mechanical characterization of partially crystallized sphere packings. *Phys. Rev. Lett.*, 113(14):148001, October 2014. doi: 10.1103/PhysRevLett.113.148001.
- [97] Peter J. Yunker, Ke Chen, Matthew D. Gratale, Matthew A. Lohr, Tim Still, and A. G. Yodh. Physics in ordered and disordered colloidal matter composed of poly(N-isopropylacrylamide) microgel particles. *Rep. Prog. Phys.*, 77(5):056601, May 2014. ISSN 0034-4885. doi: 10.1088/0034-4885/77/5/056601.
- [98] Jean Comtet, Antoine Lainé, Antoine Niguès, Lydéric Bocquet, and Alessandro Siria. Atomic rheology of gold nanojunctions. *Nature*, 569(7756):393–397, May 2019. ISSN 1476-4687. doi: 10.1038/s41586-019-1178-3.
- [99] Sho Asakura and Fumio Oosawa. On Interaction between two Bodies immersed in a solution of macromolecules. *J. Chem. Phys.*, 22(7):1255–1256, July 1954. ISSN 0021-9606. doi: 10.1063/1.1740347.
- [100] Shubha Tewari, Dylan Schiemann, Douglas J. Durian, Charles M. Knobler, Stephen A. Langer, and Andrea J. Liu. Statistics of shear-induced rearrangements in a two-dimensional model foam. *Phys. Rev. E*, 60(4):4385–4396, October 1999. doi: 10.1103/PhysRevE.60.4385.

- [101] Ran Tao, Madelyn Wilson, and Eric R. Weeks. Soft particle clogging in two-dimensional hoppers. *Phys. Rev. E*, 104(4):044909, October 2021. doi: 10.1103/PhysRevE.104.044909.
- [102] J. C. Crocker, J. A. Matteo, A. D. Dinsmore, and A. G. Yodh. Entropic attraction and repulsion in binary colloids probed with a line optical tweezer. *Phys. Rev. Lett.*, 82(21):4352–4355, May 1999. doi: 10.1103/PhysRevLett.82.4352.
- [103] Selwyn J. Rehfeld. Adsorption of sodium dodecyl sulfate at carious hydrocarbon-water interfaces. *J. Phys. Chem.*, 71(3):738–745, February 1967. ISSN 0022-3654. doi: 10.1021/j100862a039.
- [104] Kenneth W. Desmond and Eric R. Weeks. Influence of particle size distribution on random close packing of spheres. *Phys. Rev. E*, 90(2):022204, August 2014. doi: 10.1103/PhysRevE.90.022204.
- [105] David J. Meer and Eric R. Weeks. Bounded distributions place limits on skewness and larger moments. *PLOS ONE*, 19(2):e0297862, February 2024. ISSN 1932-6203. doi: 10.1371/journal.pone.0297862. URL <https://journals.plos.org/plosone/article?id=10.1371/journal.pone.0297862>. Publisher: Public Library of Science.
- [106] Walter Kob and Hans C. Andersen. Testing mode-coupling theory for a supercooled binary Lennard-Jones mixture: The van Hove correlation function. *Phys. Rev. E*, 51(5):4626–4641, May 1995. doi: 10.1103/physreve.51.4626.
- [107] Walter Kob and Hans C. Andersen. Testing mode-coupling theory for a supercooled binary Lennard-Jones mixture. II. intermediate scattering function and dynamic susceptibility. *Phys. Rev. E*, 52(4):4134–4153, October 1995. doi: 10.1103/physreve.52.4134.

- [108] Pablo E. Illing and Eric R. Weeks. Nonaffine motion in flowing highly polydisperse granular media, 2025. URL <https://arxiv.org/abs/2502.01605>.
- [109] P. Hébraud, F. Lequeux, J. P. Munch, and D. J. Pine. Yielding and Rearrangements in Disordered Emulsions. *Phys. Rev. Lett.*, 78(24):4657–4660, June 1997. doi: 10.1103/PhysRevLett.78.4657. URL <https://link.aps.org/doi/10.1103/PhysRevLett.78.4657>.
- [110] G. Petekidis, A. Moussaïd, and P. N. Pusey. Rearrangements in hard-sphere glasses under oscillatory shear strain. *Phys. Rev. E*, 66(5):051402, November 2002. doi: 10.1103/PhysRevE.66.051402. URL <https://link.aps.org/doi/10.1103/PhysRevE.66.051402>.
- [111] Peter Schall, David A. Weitz, and Frans Spaepen. Structural Rearrangements That Govern Flow in Colloidal Glasses. *Science*, 318(5858):1895–1899, December 2007. doi: 10.1126/science.1149308. URL <https://www.science.org/doi/10.1126/science.1149308>.
- [112] Dandan Chen, Denis Semwogerere, Jun Sato, Victor Breedveld, and Eric R. Weeks. Microscopic structural relaxation in a sheared supercooled colloidal liquid. *Phys. Rev. E*, 81(1):011403, January 2010. doi: 10.1103/PhysRevE.81.011403. URL <https://link.aps.org/doi/10.1103/PhysRevE.81.011403>.
- [113] Christopher N. Schädle, Stephanie Bader-Mittermaier, and Solange Sanahuja. Characterization of Reduced-Fat Mayonnaise and Comparison of Sensory Perception, Rheological, Tribological, and Textural Analyses. *Foods*, 11(6):806, January 2022. ISSN 2304-8158. doi: 10.3390/foods11060806. URL <https://www.mdpi.com/2304-8158/11/6/806>.
- [114] Vishwas V. Vasisht, Sudeep K. Dutta, Emanuela Del Gado, and Daniel L. Blair. Rate Dependence of Elementary Rearrangements and Spatiotemporal

- Correlations in the 3D Flow of Soft Solids. *Phys. Rev. Lett.*, 120(1):018001, January 2018. doi: 10.1103/PhysRevLett.120.018001. URL <https://link.aps.org/doi/10.1103/PhysRevLett.120.018001>.
- [115] Jih-Chiang (JC) Tsai, Guan-Hao Huang, and Cheng-En Tsai. Signature of Transition between Granular Solid and Fluid: Rate-Dependent Stick Slips in Steady Shearing. *Phys. Rev. Lett.*, 126(12):128001, March 2021. doi: 10.1103/PhysRevLett.126.128001. URL <https://link.aps.org/doi/10.1103/PhysRevLett.126.128001>.
- [116] R. Yamamoto and A. Onuki. Nonlinear rheology of a highly supercooled liquid. *EPL*, 40(1):61, October 1997. ISSN 0295-5075. doi: 10.1209/epl/i1997-00419-1. URL <https://iopscience.iop.org/article/10.1209/epl/i1997-00419-1/meta>.
- [117] Peter Olsson and S. Teitel. Critical Scaling of Shear Viscosity at the Jamming Transition. *Phys. Rev. Lett.*, 99(17):178001, October 2007. doi: 10.1103/PhysRevLett.99.178001. URL <https://link.aps.org/doi/10.1103/PhysRevLett.99.178001>.
- [118] Brian Utter and R. P. Behringer. Experimental Measures of Affine and Non-affine Deformation in Granular Shear. *Phys. Rev. Lett.*, 100(20):208302, May 2008. doi: 10.1103/PhysRevLett.100.208302. URL <https://link.aps.org/doi/10.1103/PhysRevLett.100.208302>.
- [119] Anaël Lemaître and Christiane Caroli. Rate-Dependent Avalanche Size in Athermally Sheared Amorphous Solids. *Phys. Rev. Lett.*, 103(6):065501, August 2009. doi: 10.1103/PhysRevLett.103.065501. URL <https://link.aps.org/doi/10.1103/PhysRevLett.103.065501>.
- [120] M. L. Manning and A. J. Liu. Vibrational Modes Identify Soft Spots in a

- Sheared Disordered Packing. *Phys. Rev. Lett.*, 107(10):108302, August 2011. doi: 10.1103/PhysRevLett.107.108302. URL <https://link.aps.org/doi/10.1103/PhysRevLett.107.108302>.
- [121] E.D. Cubuk, S.S. Schoenholz, J.M. Rieser, B.D. Malone, J. Rottler, D.J. Durian, E. Kaxiras, and A.J. Liu. Identifying Structural Flow Defects in Disordered Solids Using Machine-Learning Methods. *Phys. Rev. Lett.*, 114(10):108001, March 2015. doi: 10.1103/PhysRevLett.114.108001. URL <https://link.aps.org/doi/10.1103/PhysRevLett.114.108001>.
- [122] W. Losert, L. Bocquet, T. C. Lubensky, and J. P. Gollub. Particle Dynamics in Sheared Granular Matter. *Phys. Rev. Lett.*, 85(7):1428–1431, August 2000. doi: 10.1103/PhysRevLett.85.1428. URL <https://link.aps.org/doi/10.1103/PhysRevLett.85.1428>.
- [123] Sylvain Patinet, Damien Vandembroucq, and Michael L. Falk. Connecting Local Yield Stresses with Plastic Activity in Amorphous Solids. *Phys. Rev. Lett.*, 117(4):045501, July 2016. doi: 10.1103/PhysRevLett.117.045501. URL <https://link.aps.org/doi/10.1103/PhysRevLett.117.045501>.
- [124] J. E. Colwell, S. Batiste, M. Horányi, S. Robertson, and S. Sture. Lunar surface: Dust dynamics and regolith mechanics. *Reviews of Geophysics*, 45(2), 2007. ISSN 1944-9208. doi: 10.1029/2005RG000184. URL <https://onlinelibrary.wiley.com/doi/abs/10.1029/2005RG000184>.
- [125] C. Caracciolo, M. Napoli, F. Porcu, F. Prodi, S. Dietrich, C. Zanchi, and S. Orlandini. Raindrop Size Distribution and Soil Erosion. *J. Irrig. Drainage Eng-ASCE*, 138(5):461–469, May 2012. ISSN 0733-9437, 1943-4774. doi: 10.1061/(ASCE)IR.1943-4774.0000412. URL <https://ascelibrary.org/doi/10.1061/%28ASCE%29IR.1943-4774.0000412>.

- [126] Wilfried Haeberli, Bernard Hallet, Lukas Arenson, Roger Elconin, Ole Humlum, Andreas Kääh, Viktor Kaufmann, Branko Ladanyi, Norikazu Matsuoka, Sarah Springman, and Daniel Vonder Mühll. Permafrost creep and rock glacier dynamics. *Permafrost and Periglacial Processes*, 17(3):189–214, 2006. ISSN 1099-1530. doi: 10.1002/ppp.561. URL <https://onlinelibrary.wiley.com/doi/abs/10.1002/ppp.561>.
- [127] Mehmet Gundogdu. Discharge Characteristics of Polydisperse Powders through Conical Hoppers. Part 1: Predictions for Fine, Granular, Free Flowing Powders. *Particulate Science and Technology - PARTICULATE SCI TECHNOLOGY*, 22:339–353, October 2004. doi: 10.1080/02726350490501565.
- [128] Nicolin Govender, Daniel N. Wilke, Patrick Pizette, and Nor-Edine Abriak. A study of shape non-uniformity and poly-dispersity in hopper discharge of spherical and polyhedral particle systems using the Blaze-DEM GPU code. *Applied Mathematics and Computation*, 319:318–336, February 2018. ISSN 0096-3003. doi: 10.1016/j.amc.2017.03.037. URL <https://www.sciencedirect.com/science/article/pii/S0096300317302217>.
- [129] Nikolaos Vlachos and Isaac T. H. Chang. Investigation of flow properties of metal powders from narrow particle size distribution to polydisperse mixtures through an improved Hall-flowmeter. *Powder Technology*, 205(1):71–80, January 2011. ISSN 0032-5910. doi: 10.1016/j.powtec.2010.08.067. URL <https://www.sciencedirect.com/science/article/pii/S0032591010004687>.
- [130] E. Bruce Pitman and Long Le. A two-fluid model for avalanche and debris flows. *Philosophical Transactions of the Royal Society A: Mathematical, Physical and Engineering Sciences*, 363(1832):1573–1601, July 2005. doi: 10.1098/rsta.2005.1596. URL <https://royalsocietypublishing.org/doi/10.1098/rsta.2005.1596>.

- [131] S. Viroulet, J. L. Baker, F. M. Rocha, C. G. Johnson, B. P. Kokeelaar, and J. M. N. T. Gray. The kinematics of bidisperse granular roll waves. *Journal of Fluid Mechanics*, 848:836–875, August 2018. ISSN 0022-1120, 1469-7645. doi: 10.1017/jfm.2018.348. URL <https://www.cambridge.org/core/journals/journal-of-fluid-mechanics/article/kinematics-of-bidisperse-granular-roll-waves/13B719112388C07C04343872F086998D>.
- [132] J. M. Amundson and J. C. Burton. Quasi-Static Granular Flow of Ice Mélange. *Journal of Geophysical Research: Earth Surface*, 123(9):2243–2257, 2018. ISSN 2169-9011. doi: 10.1029/2018JF004685. URL <https://onlinelibrary.wiley.com/doi/abs/10.1029/2018JF004685>.
- [133] J. M. Amundson, M. Fahnestock, M. Truffer, J. Brown, M. P. Lüthi, and R. J. Motyka. Ice mélange dynamics and implications for terminus stability, Jakobshavn Isbræ, Greenland. *Journal of Geophysical Research: Earth Surface*, 115(F1), 2010. ISSN 2156-2202. doi: 10.1029/2009JF001405. URL <https://onlinelibrary.wiley.com/doi/abs/10.1029/2009JF001405>.
- [134] J.e. Taylor, I. Van Damme, M.l. Johns, A.f. Routh, and D.i. Wilson. Shear Rheology of Molten Crumb Chocolate. *Journal of Food Science*, 74(2):E55–E61, 2009. ISSN 1750-3841. doi: 10.1111/j.1750-3841.2008.01041.x. URL <https://onlinelibrary.wiley.com/doi/abs/10.1111/j.1750-3841.2008.01041.x>.
- [135] Peter Sollich and Nigel B. Wilding. Crystalline Phases of Polydisperse Spheres. *Phys. Rev. Lett.*, 104(11):118302, March 2010. doi: 10.1103/PhysRevLett.104.118302. URL <https://link.aps.org/doi/10.1103/PhysRevLett.104.118302>.
- [136] Sameer Kumar, Jay Prakash Singh, Debaprasad Giri, and Shradha Mishra.

- Effect of polydispersity on the dynamics of active Brownian particles. *Phys. Rev. E*, 104(2):024601, August 2021. doi: 10.1103/PhysRevE.104.024601. URL <https://link.aps.org/doi/10.1103/PhysRevE.104.024601>.
- [137] Duc-Hanh Nguyen, Emilien Azéma, Farhang Radjai, and Philippe Sornay. Effect of size polydispersity versus particle shape in dense granular media. *Phys. Rev. E*, 90(1):012202, July 2014. doi: 10.1103/PhysRevE.90.012202. URL <https://link.aps.org/doi/10.1103/PhysRevE.90.012202>.
- [138] Duc-Hanh Nguyen, Emilien Azéma, Philippe Sornay, and Farhang Radjai. Effects of shape and size polydispersity on strength properties of granular materials. *Phys. Rev. E*, 91(3):032203, March 2015. doi: 10.1103/PhysRevE.91.032203. URL <https://link.aps.org/doi/10.1103/PhysRevE.91.032203>.
- [139] David Cantor, Emilien Azéma, Philippe Sornay, and Farhang Radjai. Rheology and structure of polydisperse three-dimensional packings of spheres. *Phys. Rev. E*, 98(5):052910, November 2018. doi: 10.1103/PhysRevE.98.052910. URL <https://link.aps.org/doi/10.1103/PhysRevE.98.052910>.
- [140] Lia Papadopoulos, Mason A Porter, Karen E Daniels, and Danielle S Bassett. Network analysis of particles and grains. *Journal of Complex Networks*, 6(4):485–565, August 2018. ISSN 2051-1329. doi: 10.1093/comnet/cny005.
- [141] Sidhant Pednekar, Jaehun Chun, and Jeffrey F. Morris. Bidisperse and polydisperse suspension rheology at large solid fraction. *Journal of Rheology*, 62(2):513–526, March 2018. ISSN 0148-6055. doi: 10.1122/1.5011353. URL <https://doi.org/10.1122/1.5011353>.
- [142] Donna N. Perera and Peter Harrowell. Relaxation dynamics and their spatial distribution in a two-dimensional glass-forming mixture. *J. Chem. Phys.*, 111(12):5441–5454, 1999. doi: 10.1063/1.479804.

- [143] Robin J. Speedy. Glass transition in hard disc mixtures. *J. Chem. Phys.*, 110(9):4559–4565, March 1999. ISSN 0021-9606. doi: 10.1063/1.478337. URL <https://doi.org/10.1063/1.478337>.
- [144] J. Clara-Rahola, T. A. Brzinski, D. Semwogerere, K. Feitosa, J. C. Crocker, J. Sato, V. Breedveld, and Eric R. Weeks. Affine and nonaffine motions in sheared polydisperse emulsions. *Phys. Rev. E*, 91(1):010301, January 2015. doi: 10.1103/PhysRevE.91.010301. URL <https://link.aps.org/doi/10.1103/PhysRevE.91.010301>.
- [145] John C. Crocker and David G. Grier. Methods of digital video microscopy for colloidal studies. *Journal of Colloid and Interface Science*, 179(1):298–310, April 1996. ISSN 0021-9797. doi: 10.1006/jcis.1996.0217.
- [146] B. Lautrup. *Physics of Continuous Matter: Exotic and Everyday Phenomena in the Macroscopic World*. CRC Press, 2011. ISBN 9781439894200. URL <https://books.google.com/books?id=ohbSBQAAQBAJ>.
- [147] F. Leonforte, R. Boissière, A. Tanguy, J. P. Wittmer, and J. L. Barrat. Continuum limit of amorphous elastic bodies. III. three-dimensional systems. *Phys. Rev. B*, 72(22):224206, December 2005. doi: 10.1103/physrevb.72.224206.
- [148] Anaël Lemaître and Christiane Caroli. Plastic response of a two-dimensional amorphous solid to quasistatic shear: Transverse particle diffusion and phenomenology of dissipative events. *Phys. Rev. E*, 76(3):036104, 2007. doi: 10.1103/PhysRevE.76.036104.
- [149] Craig E. Maloney and Mark O. Robbins. Evolution of displacements and strains in sheared amorphous solids. *J. Phys.: Condens. Matter*, 20(24):244128, 2008. doi: 10.1088/0953-8984/20/24/244128.

- [150] R. Besseling, Eric R. Weeks, A. B. Schofield, and W. C. K. Poon. Three-dimensional imaging of colloidal glasses under steady shear. *Phys. Rev. Lett.*, 99(2):028301, July 2007. doi: 10.1103/physrevlett.99.028301.
- [151] Yonglun Jiang, Eric R. Weeks, and Nicholas P. Bailey. Isomorphs in sheared binary Lennard-Jones glass: Transient response. *Phys. Rev. E*, 107(1):014610, January 2023. doi: 10.1103/PhysRevE.107.014610. URL <https://link.aps.org/doi/10.1103/PhysRevE.107.014610>. Publisher: American Physical Society.
- [152] Muhammad Hassani, Alexandra E. Lagogianni, and Fathollah Varnik. Probing the Degree of Heterogeneity within a Shear Band of a Model Glass. *Physical Review Letters*, 123(19):195502, November 2019. doi: 10.1103/PhysRevLett.123.195502. URL <https://link.aps.org/doi/10.1103/PhysRevLett.123.195502>. Publisher: American Physical Society.
- [153] Nikolai V. Priezjev. Collective nonaffine displacements in amorphous materials during large-amplitude oscillatory shear. *Phys. Rev. E*, 95(2):023002, February 2017. doi: 10.1103/physreve.95.023002.
- [154] Kenneth W. Desmond and Eric R. Weeks. Measurement of stress redistribution in flowing emulsions. *Phys. Rev. Lett.*, 115(9):098302, August 2015. doi: 10.1103/physrevlett.115.098302.
- [155] Hadi Karimi, Hossein Navid, Bahram Besharati, and Iraj Eskandari. Assessing an infrared-based seed drill monitoring system under field operating conditions. *Computers and Electronics in Agriculture*, 162:543–551, 2019. ISSN 0168-1699. doi: <https://doi.org/10.1016/j.compag.2019.04.045>. URL <https://www.sciencedirect.com/science/article/pii/S0168169919300109>.
- [156] J.J Fitzpatrick, S.A Barringer, and T Iqbal. Flow property measurement of

- food powders and sensitivity of Jenike's hopper design methodology to the measured values. *Journal of Food Engineering*, 61(3):399–405, 2004. ISSN 0260-8774. doi: [https://doi.org/10.1016/S0260-8774\(03\)00147-X](https://doi.org/10.1016/S0260-8774(03)00147-X). URL <https://www.sciencedirect.com/science/article/pii/S026087740300147X>.
- [157] Kiwing To, Pik-Yin Lai, and H. K. Pak. Jamming of Granular Flow in a Two-Dimensional Hopper. *Phys. Rev. Lett.*, 86(1):71–74, January 2001. doi: 10.1103/PhysRevLett.86.71. URL <https://link.aps.org/doi/10.1103/PhysRevLett.86.71>. Publisher: American Physical Society.
- [158] Iker Zuriguel, Luis A. Pugnaloni, Angel Garcimartín, and Diego Maza. Jamming during the discharge of grains from a silo described as a percolating transition. *Phys. Rev. E*, 68(3):030301, September 2003. doi: 10.1103/PhysRevE.68.030301. URL <https://link.aps.org/doi/10.1103/PhysRevE.68.030301>. Publisher: American Physical Society.
- [159] Kiwing To. Jamming transition in two-dimensional hoppers and silos. *Phys. Rev. E*, 71(6):060301, June 2005. doi: 10.1103/PhysRevE.71.060301. URL <https://link.aps.org/doi/10.1103/PhysRevE.71.060301>. Publisher: American Physical Society.
- [160] Iker Zuriguel, Angel Garcimartín, Diego Maza, Luis A. Pugnaloni, and J. M. Pastor. Jamming during the discharge of granular matter from a silo. *Phys. Rev. E*, 71(5):051303, May 2005. doi: 10.1103/PhysRevE.71.051303. URL <https://link.aps.org/doi/10.1103/PhysRevE.71.051303>. Publisher: American Physical Society.
- [161] I. Zuriguel and A. Garcimartín. Statistical Mechanics of Clogging. In Robert A. Meyers, editor, *Encyclopedia of Complexity and Systems Science*, pages 1–32.

- Springer, Berlin, Heidelberg, 2020. ISBN 978-3-642-27737-5. doi: 10.1007/978-3-642-27737-5_746-1.
- [162] L. Pournin, M. Ramaioli, P. Folly, and Th. M. Liebling. About the influence of friction and polydispersity on the jamming behavior of bead assemblies. *Eur. Phys. J. E*, 23(2):229–235, June 2007. ISSN 1292-895X. doi: 10.1140/epje/i2007-10176-5.
- [163] Ahmed Ashour, Torsten Trittel, Tamás Börzsönyi, and Ralf Stannarius. Silo outflow of soft frictionless spheres. *Phys. Rev. Fluids*, 2(12):123302, December 2017. doi: 10.1103/PhysRevFluids.2.123302.
- [164] Saeed Alborzi, David Abrahamyan, and Sara M. Hashmi. Mixing particle softness in a two-dimensional hopper: Particle rigidity and friction enable variable arch geometry to cause clogging. *Phys. Rev. E*, 107(2):024901, February 2023. doi: 10.1103/PhysRevE.107.024901.
- [165] Yann Bertho, Christophe Becco, and Nicolas Vandewalle. Dense bubble flow in a silo: An unusual flow of a dispersed medium. *Phys. Rev. E*, 73(5):056309, May 2006. doi: 10.1103/PhysRevE.73.056309. URL <https://link.aps.org/doi/10.1103/PhysRevE.73.056309>. Publisher: American Physical Society.
- [166] Saeed Alborzi, Benjamin G. Clark, and Sara M. Hashmi. Soft particles facilitate flow of rigid particles in a 2D hopper. *Soft Matter*, 18(21):4127–4135, June 2022. ISSN 1744-6848. doi: 10.1039/D2SM00318J. URL <https://pubs.rsc.org/en/content/articlelanding/2022/sm/d2sm00318j>. Publisher: The Royal Society of Chemistry.
- [167] Yuxuan Cheng, John D. Treado, Benjamin F. Lonial, Piotr Habdas, Eric R. Weeks, Mark D. Shattuck, and Corey S. O’Hern. Hopper flows of deformable particles. *Soft Matter*, 18(42):8071–8086, November 2022. ISSN

- 1744-6848. doi: 10.1039/D2SM01079H. URL <https://pubs.rsc.org/en/content/articlelanding/2022/sm/d2sm01079h>. Publisher: The Royal Society of Chemistry.
- [168] Saeed Alborzi, David Abrahamyan, and Sara M. Hashmi. Mixing particle softness in a two-dimensional hopper: Particle rigidity and friction enable variable arch geometry to cause clogging. *Phys. Rev. E*, 107(2):024901, February 2023. doi: 10.1103/PhysRevE.107.024901. URL <https://link.aps.org/doi/10.1103/PhysRevE.107.024901>. Publisher: American Physical Society.
- [169] Junyao Tang and R. P. Behringer. Orientation, flow, and clogging in a two-dimensional hopper: Ellipses vs. disks. *EPL*, 114(3):34002, May 2016. ISSN 0295-5075. doi: 10.1209/0295-5075/114/34002.
- [170] Ezequiel Goldberg, C. Manuel Carlevaro, and Luis A. Pugnaloni. Clogging in two-dimensions: Effect of particle shape. *J. Stat. Mech.*, 2018(11):113201, November 2018. ISSN 1742-5468. doi: 10.1088/1742-5468/aae84b.
- [171] Ahmed Hafez, Qi Liu, Thomas Finkbeiner, Raed A. Alouhali, Timothy E. Moellendick, and J. Carlos Santamarina. The effect of particle shape on discharge and clogging. *Sci Rep*, 11(1):3309, February 2021. ISSN 2045-2322. doi: 10.1038/s41598-021-82744-w.
- [172] S. Dorbolo, L. Maquet, M. Brandenbourger, F. Ludewig, G. Lumay, H. Caps, N. Vandewalle, S. Rondia, M. Mélard, J. van Loon, A. Dowson, and S. Vincent-Bonnieu. Influence of the gravity on the discharge of a silo. *Granular Matter*, 15(3):263–273, June 2013. ISSN 1434-7636. doi: 10.1007/s10035-013-0403-2.
- [173] Roberto Arévalo, Iker Zuriguel, Diego Maza, and Angel Garcimartín. Role of driving force on the clogging of inert particles in a bottleneck. *Phys. Rev. E*, 89(4):042205, April 2014. doi: 10.1103/PhysRevE.89.042205.

- [174] Diego López-Rodríguez, Diego Gella, Kiwing To, Diego Maza, Angel Garcimartín, and Iker Zuriguel. Effect of hopper angle on granular clogging. *Phys. Rev. E*, 99(3):032901, March 2019. doi: 10.1103/PhysRevE.99.032901. URL <https://link.aps.org/doi/10.1103/PhysRevE.99.032901>. Publisher: American Physical Society.
- [175] Saeed Albaraki and S. Joseph Antony. How does internal angle of hoppers affect granular flow? Experimental studies using digital particle image velocimetry. *Powder Technology*, 268:253–260, December 2014. ISSN 0032-5910. doi: 10.1016/j.powtec.2014.08.027. URL <https://www.sciencedirect.com/science/article/pii/S003259101400727X>.
- [176] Quan-Chun Yu, Ning Zheng, and Qing-Fan Shi. Clogging of granular materials in a horizontal hopper: Effect of outlet size, hopper angle, and driving velocity. *Phys. Rev. E*, 103(5):052902, May 2021. doi: 10.1103/PhysRevE.103.052902. URL <https://link.aps.org/doi/10.1103/PhysRevE.103.052902>. Publisher: American Physical Society.
- [177] Annamária Szalay, András Kelemen, and Klára Pintye-Hódi. The influence of the cohesion coefficient (C) on the flowability of different sorbitol types. *Chemical Engineering Research and Design*, 93:349–354, January 2015. ISSN 0263-8762. doi: 10.1016/j.cherd.2014.05.008. URL <https://www.sciencedirect.com/science/article/pii/S0263876214002184>.
- [178] Adrien Gans, Olivier Pouliquen, and Maxime Nicolas. Cohesion-controlled granular material. *Phys. Rev. E*, 101(3):032904, March 2020. doi: 10.1103/PhysRevE.101.032904. URL <https://link.aps.org/doi/10.1103/PhysRevE.101.032904>. Publisher: American Physical Society.
- [179] Adrien Gans, Pascale Aussillous, Blanche Dalloz, and Maxime Nico-

- las. The effect of cohesion on the discharge of a granular material through the orifice of a silo. *EPJ Web Conf.*, 249:08014, 2021. ISSN 2100-014X. doi: 10.1051/epjconf/202124908014. URL https://www.epj-conferences.org/articles/epjconf/abs/2021/03/epjconf_pg2021_08014/epjconf_pg2021_08014.html. Publisher: EDP Sciences.
- [180] Renjun Zhang, Zhibing Yang, Russell Detwiler, Dongqi Li, Gang Ma, Ran Hu, and Yi-Feng Chen. Liquid Cohesion Induced Particle Agglomeration Enhances Clogging in Rock Fractures. *Geophysical Research Letters*, 50(5):e2022GL102097, 2023. ISSN 1944-8007. doi: 10.1029/2022GL102097. URL <https://onlinelibrary.wiley.com/doi/abs/10.1029/2022GL102097>. eprint: <https://onlinelibrary.wiley.com/doi/pdf/10.1029/2022GL102097>.
- [181] A. Vrij. Polymers at Interfaces and the Interactions in Colloidal Dispersions. *Pure and Applied Chemistry*, 48(4):471–483, January 1976. ISSN 1365-3075. doi: 10.1351/pac197648040471. URL <https://www.degruyter.com/document/doi/10.1351/pac197648040471/html>. Publisher: De Gruyter.
- [182] J. Bibette, D. Roux, and B. Pouligny. Creaming of emulsions: the role of depletion forces induced by surfactant. *J. Phys. II France*, 2(3):401–424, March 1992. ISSN 1155-4312, 1286-4870. doi: 10.1051/jp2:1992141. URL <http://dx.doi.org/10.1051/jp2:1992141>. Publisher: EDP Sciences.
- [183] Johnathan Hoggarth, Jean-Christophe Ono-dit biot, and Kari Dalnoki-Veress. Two-dimensional spreading of frictionless adhesive oil droplets. *Soft Matter*, 19(20):3747–3753, May 2023. ISSN 1744-6848. doi: 10.1039/D2SM01655A. URL <https://pubs.rsc.org/en/content/articlelanding/2023/sm/d2sm01655a>. Publisher: The Royal Society of Chemistry.

- [184] Luis A. Pugnaloni and G. C. Barker. Structure and distribution of arches in shaken hard sphere deposits. *Physica A: Statistical Mechanics and its Applications*, 337(3):428–442, June 2004. ISSN 0378-4371. doi: 10.1016/j.physa.2004.02.004. URL <https://www.sciencedirect.com/science/article/pii/S0378437104001839>.
- [185] Roberto Arévalo, Diego Maza, and Luis A. Pugnaloni. Identification of arches in two-dimensional granular packings. *Physical Review E*, 74(2):021303, August 2006. doi: 10.1103/PhysRevE.74.021303. URL <https://link.aps.org/doi/10.1103/PhysRevE.74.021303>. Publisher: American Physical Society.
- [186] Farnaz Fazelpour, Zhu Tang, and Karen E. Daniels. The effect of grain shape and material on the nonlocal rheology of dense granular flows. *Soft Matter*, 18(7):1435–1442, February 2022. ISSN 1744-6848. doi: 10.1039/D1SM01237A. URL <https://pubs.rsc.org/en/content/articlelanding/2022/sm/d1sm01237a>.
- [187] Julian O. Freeman, Sean Peterson, Cong Cao, Yujie Wang, Scott V. Franklin, and Eric R. Weeks. Random packing of rods in small containers. *Granular Matter*, 21(4):84, August 2019. ISSN 1434-7636. doi: 10.1007/s10035-019-0939-x. URL <https://doi.org/10.1007/s10035-019-0939-x>.
- [188] Theodore A. Marschall, Scott V. Franklin, and S. Teitel. Compression- and shear-driven jamming of U-shaped particles in two dimensions. *Granular Matter*, 17(1):121–133, February 2015. ISSN 1434-7636. doi: 10.1007/s10035-014-0540-2. URL <https://doi.org/10.1007/s10035-014-0540-2>.
- [189] Theodore A. Marschall and S. Teitel. Athermal shearing of frictionless cross-shaped particles of varying aspect ratio. *Granular Matter*, 22(1):4, November

2019. ISSN 1434-7636. doi: 10.1007/s10035-019-0966-7. URL <https://doi.org/10.1007/s10035-019-0966-7>.

- [190] G. Lumay and N. Vandewalle. Experimental study of the compaction dynamics for two-dimensional anisotropic granular materials. *Physical Review E*, 74(2): 021301, August 2006. doi: 10.1103/PhysRevE.74.021301. URL <https://link.aps.org/doi/10.1103/PhysRevE.74.021301>. Publisher: American Physical Society.
- [191] Karen E. Daniels, Jonathan E. Kollmer, and James G. Puckett. Photoelastic force measurements in granular materials. *Rev. Sci. Instrum.*, 88(5): 051808, 2017. ISSN 0034-6748. doi: 10.1063/1.4983049. URL <https://doi.org/10.1063/1.4983049>. eprint: https://pubs.aip.org/aip/rsi/article-pdf/doi/10.1063/1.4983049/14769184/051808.1_online.pdf.